UNIVERSITÀ DEGLI STUDI DI PALERMO

ANALYSIS OF A HYBRID PROPULSION SYSTEM WITH EXHAUST GAS ENERGY RECOVERY

DOCTOR OF PHILOSOPHY

SALVATORE CALTABELLOTTA

ACADEMIC TUTOR

PROF. EMILIANO PIPITONE

ACADEMIC YEAR 2022-2023

Abstract

As widely known internal combustion engines are not able to complete the expansion process of the gas inside the cylinder, causing theoretical energy losses of the order of 20%. Several systems and methods have been proposed and implemented to recover the unexpanded gas energy, such as turbocharging, which partially exploits this energy to compress the intake fresh charge, or turbo-mechanical and turbo-electrical compounding, where the amount of unexpanded gas energy not used by the compressor is dedicated to propulsion or transformed into electric energy. In all these cases, however, maximum efficiency improvements between 4% and 9% have been achieved. In this thesis, the author deals with an innovative propulsion system composed of a spark ignition engine equipped with a turbo-generator group specifically dedicated to the unexpanded exhaust gas energy recovery and with a separated electrical-driven turbocompressor. The system has been conceived specifically for hybrid propulsion architectures, being the electric energy produced by the turbine-generator easily storable in the on-board energy storage system and reusable for vehicle traction. The turbo-generator unit should be composed of two fundamental elements: an exhaust gas turbine expressly designed and optimized for the application, and a suitable electric generator necessary to convert the recovered energy into electric energy, which could hence be stored in the on-board energy storage system of the vehicle. Being optimized for quasi-steady power production, the exhaust gas turbine here dealt with is quite different from those commonly employed for turbocharging applications; for this reason, considering the power size of the machine, such a turbine is not available on the market, nor its development has been carried out in the scientific literature. On account of

this, the author of the present thesis implemented a mean-line design algorithm to estimate the main turbine geometric dimensions. Once determined the turbine geometry, it was developed a turbine mean-line performance prediction model to evaluate the realistic performance of the electric turbo-compound system: as an overall result, it was estimated that, compared to a reference traditional turbocharged engine, the electric turbo-compound system could gain vehicle efficiency improvement between 3.1% and 17.9%, depending on the output power level, whit an average efficiency increment of 10.9% evaluated on the whole operating range.

Index

1. Introduction

The continuous growth of global population and the development of emerging economies tend to increase the human consumption of natural resources and the environmental impact of human activities. Among the negative effects of the latter, particularly relevant is the release of greenhouse gases in the atmosphere, which causes the well-known global warming and the related climate change. The European Union addresses this challenge through the European Green Deal, which is a plan to make the EU the first carbon-neutral continent by 2050, passing through the intermediate goal of 55% CO2 emissions cut by 2030 [1]. The data provided by the European Environment Agency (EEA) in 2018 showed that the transport sector is responsible for about 32% of the total CO2 emissions in the European Union [2]. As a consequence, actions are being taken to achieve the reduction of pollutant emissions from road, rail, aviation, and waterborne transport [3]. Among the most interesting and short-term solutions, hybrid electric vehicles (HEVs) certainly represent a valid alternative compared to traditional internal combustion engine vehicles (ICEVs), given the significant fuel savings achieved, especially in urban areas; although good technological levels have already been reached, their development is relatively recent, which is why there is still plenty of room for improvement. In this framework, the author performed a study aimed at investigating and designing a system that allows better exploitation of the chemical energy contained in the fuel used in internal combustion engines. In a hybrid thermal-electric architecture, a possible development area is represented undoubtedly by the internal combustion engine, which produces the energy necessary for vehicle traction and battery charging; a significant increase in the engine efficiency may produce considerable

improvements in the efficiency of the entire propulsion system. As widely known, internal combustion engines based on Otto or Diesel cycles do not complete the in-cylinder gas expansion down to the atmospheric pressure: as a result, hot and pressurized gas exits the cylinder during the exhaust process, thus reducing by about 20% the energy transfer to the piston. Several solutions have been implemented to recover the unexpanded gas energy; the Atkinson cycle, for instance, allows a theoretical efficiency increase of 20% compared to the Otto cycle with the same compression ratio (represented by the two dashed areas in **Figure 1**).

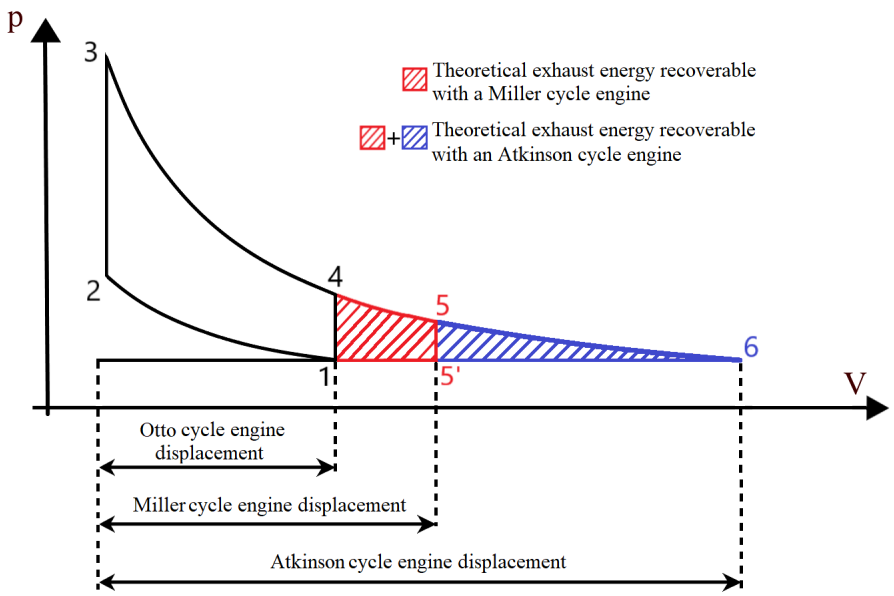

Figure 1: Comparison between Otto, Miller and Atkinson cycle

In an Atkinson cycle the expansion stroke should be extended up to atmospheric pressure [4][5][6]; this could be achieved through the use of adequate intake valve timing in a properly designed engine. As can be seen from Figure 1 (curve 1-2-3-6-1), the Atkinson cycle allows to recover both the blue and red area, allowing theoretical efficiency increase of about 20% compared to the Otto cycle. This would imply however an impracticable too large in-cylinder volume, about four times the corresponding volume

of the Otto cycle engine. This implies a strong decrease in the engine power density (in the order of -72%).

In the Miller cycle, on the other hand, the gas expands down to the pressure p_5 which is significantly higher than the atmospheric pressure [7], thus maintaining plausible in-cylinder volumes. A Miller cycle engine can be practically developed by adopting a high engine geometrical compression ratio (GCR) and early (or late) intake valve closure (IVC). In this way, the compression stroke is limited (avoiding dangerous knocking phenomena), while the expansion stroke can be better exploited [8]: adopting a geometrical compression ratio (GCR) of 14, an 8% theoretical efficiency increment can be obtained with respect to Otto cycle, to the detriment of the power density, which results reduced by about 25%. A practical application of a Miller cycle engine was made by Toyota in the Prius hybrid vehicle, in which an engine with a geometrical compression ratio of 13 was adopted: through this application it was possible to obtain a fuel economy improvement of 8.5% [9]. Although the implementation of the Miller cycle can bring good fuel consumption improvement, the resulting power density reduction still represents a crucial drawback which limits its advantage [10].

The best-known system for the exploitation of exhaust gas energy is certainly represented by the exhaust gas turbine used for turbocharging purpose. In this case, the turbine has only the function of providing the mechanical power required by the turbocompressor, thus limiting the amount of recoverable energy from exhaust gas. Several other systems for internal combustion engine exhaust energy recovery can be traced in the scientific literature [11] [12]. Many systems focus on recovering the surplus power produced by the turbine and not required by the turbocompressor,

through the use of an electric generator installed on the turbocharger shaft [13][14][15][16] (type (a) in **Figure 2**); another kind of turbo-compound systems involves the installation of a second turbine-generator downstream the first turbine in order to recover the exhaust energy not yet exploited (type (b) in Figure 2).

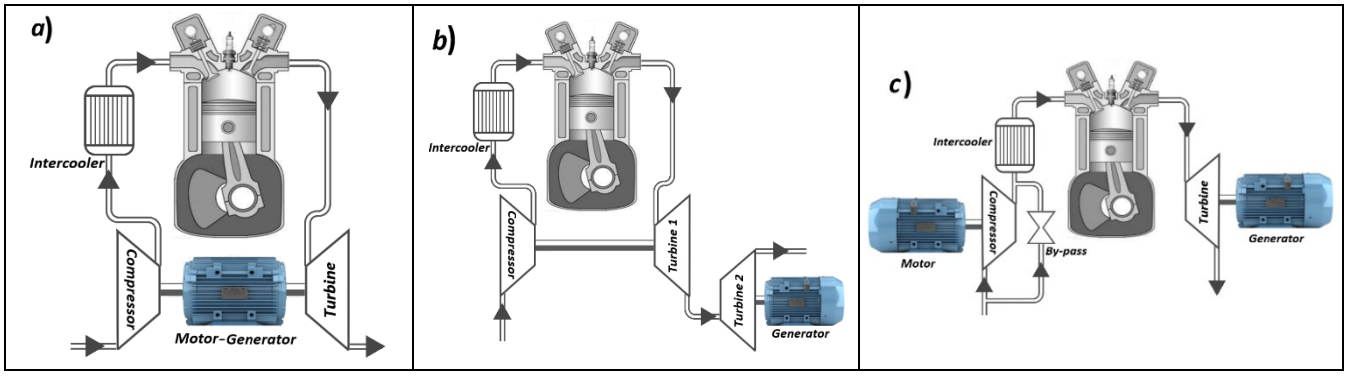

Figure 2: Electric compound systems [11]: a) High pressure electric compound; b) Low pressure electric compound; c) Separated electric compound

The first solution (type (a)), achieves maximum overall efficiency improvements of the order of 6%, while the second solution (type (b)) proved efficiency improvements within 4% [17][18]. In the naval industry the type (b) has been widely adopted, with a second turbine downstream of the first, whose output power was directly added as mechanical power to the propeller shaft. In [19] and [20], on the other hand, the use of a second turbine in parallel to the first (used for supercharging) was considered, in both cases the use of both a fixed and a variable geometry turbine was hypothesized. With this type of turbo-compound system, efficiency improvements of up to 9% have been evaluated. In this work the author analyses the energetic advantages of a compound system (type (c) in Figure 2) composed by an electric supercharged spark ignition engine endowed of a dedicated exhaust gas turbo-generator group whit the aim to recover the un-expanded exhaust gas energy. The turbo-generator group is composed of a radial inflow turbine directly linked whit a suitable electric generator,

while the compressor is driven by an electric motor. Unlike the compound systems already studied (type (a) and (b) in **Figure 2**), in this work the two thermal machines (compressor and turbine) are disconnected, thus working independently of each other. In turn, each thermal machine is connected to its own electric machine, thus ensuring a more flexible and extensive regulation of the entire system. In the system here proposed the turbine has the task of recovering as much energy as possible from the exhaust gas, which is converted into electrical energy by the connected electrical generator. The separated electric turbo-compound system is particularly suitable for hybrid propulsion vehicles [21], where the electricity produced by the turbo-generator group can be stored in the on-board storage system and then used for the vehicle traction. It is important to note that in a hybrid propulsion system, the operating conditions of the thermal engine do not vary widely and rapidly as in a traditional vehicle; for this reason the turbine of the compound-engine could work in quasi-steady conditions; for this reason the turbine considered for this application will certainly have a higher efficiency than a traditional turbocharging turbine. Quite differently, the turbines usually employed for turbocharging purpose provide only the power required by the compressor and are designed for unsteady operation on account of the strong speed and mass flow variations due to the wide and rapid speed and load variation of the thermal engine.

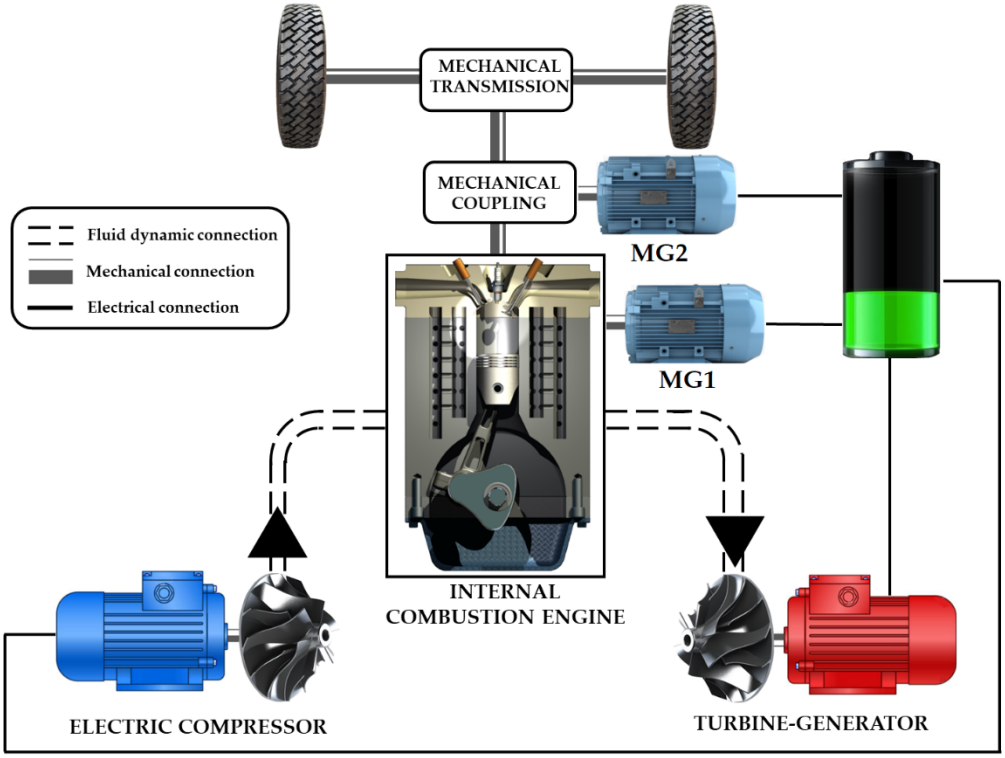

Figure 3: Separated electric compound system (MG1 and MG2=motor-generator units)

This clarifies that the turbo-generator here considered, as well as the whole hybrid propulsion system of **Figure** 3, is not commercially available at the moment. The only commercially available products are composed of a radial turbine for turbocharging application connected to an electric generator [22-24] and are designed exclusively to supply the electric accessories of traditional vehicles, thus producing maximum output power within 6 kW. **Figure** 3 shows a possible hybrid vehicle architecture equipped with the electric compound engine proposed in this thesis: as shown, the electric power produced by the turbine-generator, together with the power delivered by the motor-generator MG1, is directly stored in the vehicle's storage system, which, in turn, supplies the second electric machine MG2 and the motor-compressor employed for supercharging purpose. In this work, the steady state performances of the proposed separated electric compound engine are evaluated and compared to the

performance of a traditional reference turbocharged engine on an equal power basis, i.e. each propulsion unit was sized to deliver the same continuous maximum power of 73.5 kW (100 HP). Each power unit was also supposed to be developed starting from the same reference naturally aspirated engine, whose performance evaluation will be described further on. The whole analysis was carried out through a simple modelling approach, mainly based on mass flow and power balances equations, properly accompanied by simplifying assumptions and relations; the theoretical approach was also supported by experimental data derived from relevant scientific literature or directly measured through experimental test carried out by the same author. In the first part of this thesis, for the preliminary evaluation of the performance advantages of the separated electric compound engine, due to the lack of adequate products both in the literature and on the market, the author assumed that in the compound engine, the turbine works with an almost constant speed ratio, regardless of the power produced, and hence with an almost constant thermomechanical efficiency $\eta_{T,t,m}$. In order to investigate a wider range of possibilities, thus assessing the effect of this parameter on the overall energetic performance of the entire compound system, the author decided to consider two different efficiency levels. In detail, the two levels of efficiency considered for the compound engine turbine are $\eta_{T,t,m}$ = 0.70 and $\eta_{T,t,m}$ = 0.75. In the second part of the thesis, in order to provide a more precise and reliable estimation of the performances of the separated electric compound system by evaluating the turbine efficiency in accordance with its operating condition and thus getting rid of the simplifying assumption used in the first part of the work, the author focused on the design and analysis of the turbine.

2. Compound engine concept description

The powertrain architecture considered in this thesis is given as type (c) in **Figure 2**. Unlike other studied electric compound systems (types (b) and (c) in Figure 2), the two thermal machines (Compressor and Turbine) operate independently in the system considered here. Each one is connected to its own electric machine, and the turbo-generator group operates at high pressure directly downstream of the thermal engine. The compound system here presented is hence composed of an electrically supercharged spark ignition (SI) engine whose exhaust gas flows through a properly designed exhaust gas turbine connected to an electrical generator. The system is specifically intended for a hybrid propulsion architecture application [21], where the onboard storage system may receive and store the energy produced by the turbo-generator group. This energy can then be employed for vehicle propulsion. Moreover, in a hybrid propulsion system, the thermal engine is not involved throughout the wide and rapidly changing operating conditions of a traditional vehicle. Therefore, the exhaust gas turbine could be used under quasi-steady conditions, and hence near-maximum expansion efficiency. For this reason, the compound engine (CE) considered in this thesis is particularly suitable for applying to thermal-electric hybrid propulsion systems. **Figure** 3 shows a possible hybrid propulsion layout that includes the compound engine concept. The net power produced by the turbine-generator is summed to the power delivered by the thermal engine-generator (MG1) in the energy storage system, which in turn, supplies the second electric machine (MG2) and the electric compressor employed for supercharging purposes. It is worth mentioning that in the described system, the turbo-generator group is always active in conjunction with the thermal engine, contributing to the

energy balance of the whole vehicle. However, the electric compressor unit is powered only when supercharging is required, i.e., only when higher engine loads are required. In this work, the author aims to evaluate the efficiency improvements obtainable by the proposed separated electric compound system in comparison with a traditional turbocharged engine for hybrid vehicle applications. The aforementioned performance comparison was conducted between through a simple yet effective modeling approach. Fundamentally, the approach consists of mass flow and power balance equations, accompanied by simplifying assumptions and relations. The theoretical approach was also supported by experimental data derived from relevant scientific literature or directly measured through experiments. Focusing on the hybrid vehicle application, the comparison considered only steady-state conditions and was carried out on an equal output power basis; all the propulsive units were sized for the same maximum output power of 73.5 kW (i.e., 100 HP). The concept described here is novel, as there is no evidence of a study like the one presented here in the scientific literature. Although the separated electric compound engine has been cited in [25] among several other different systems that could be simulated, its advantages in terms of overall efficiency were not evaluated, nor were its performances compared to a traditional internal combustion engine.

3. Baseline Naturally Aspirated Engine

As a first step, the author developed the steady state performances of the baseline naturally aspirated engine. Starting from the characteristics and the specific performances of this common baseline naturally aspirated engine, the performances of both the separated electric turbo-compound unit and the reference turbocharged engine were obtained. For the development of the baseline naturally aspirated engine model, the author employed the experimental data of the gasoline VVT spark ignition engine reported in [26]. The system analyzed in the present work was conceived for a European Type C–Medium hybrid vehicle, while the gasoline spark ignition engine presented in [26] is an 8 cylinders engine with a displacement of 4244 cm^3, typical of an higher car segment. In order to adapt the engine performances reported in [26] to a mid-level passenger car engine, the author adopt a normalization process of the mean piston speed. The normalized mean piston speed S was then employed:

$$S = \frac{Sp}{Sp_{\max}} \qquad (0 \le S \le 1) \tag{1}$$

As a result, Figure 4 and Figure 5 show the resulting values of:

- Brake mean effective pressure (*BMEP*)
- Indicated mean effective pressure (*IMEP*)
- Relative air–fuel ratio (λ)
- Volumetric efficiency (λ_V)

as functions of the normalized mean piston speed S and for the full load condition (or wide-open throttle, *WOT*), while Figure 6 shows the *BMEP* as a function of the manifold absolute pressure (*MAP*) for a fixed normalized mean piston speed (S = 0.267).

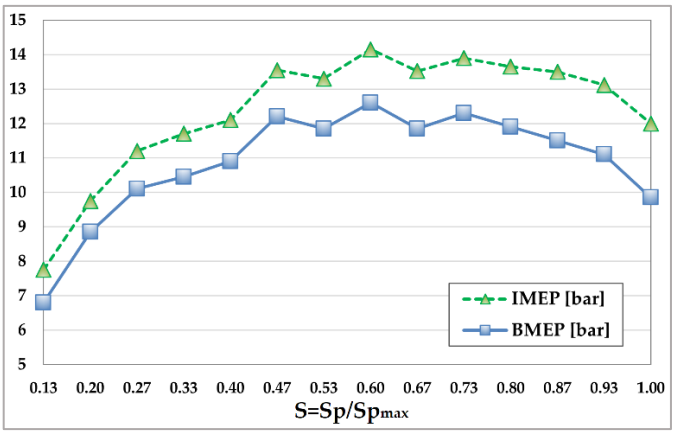

Figure 4: Brake (*BMEP*) and indicated (*IMEP*) mean effective pressure as functions of the normalized mean piston speed *S*, at full load conditions.

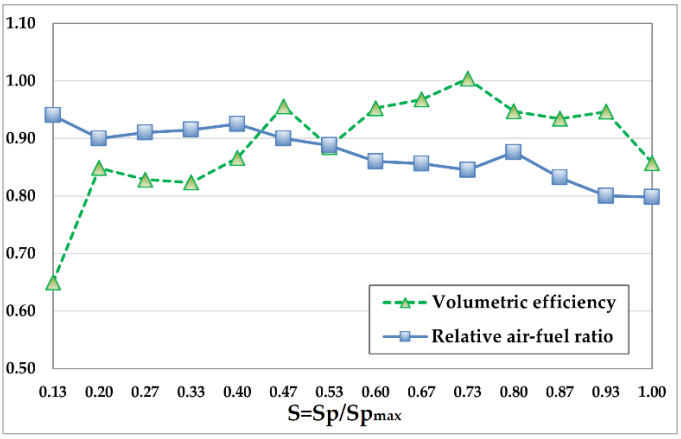

Figure 5: Volumetric efficiency and relative air-fuel ratio as function of the normalized mean piston speed, at full load condition.

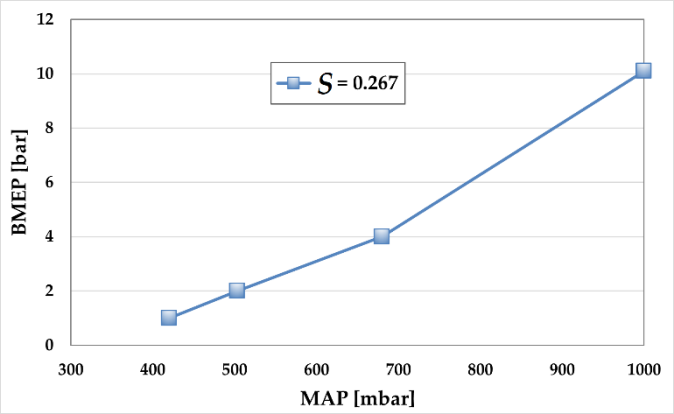

Figure 6: Brake mean effective pressure as function of manifold absolute pressure (*MAP*) at *S*=0.267

In this work, for the evaluation of the friction mean effective pressure *FMEP* the author adopts the Chen & Flynn friction model. This model is one of the most encountered in literature and employed in commercial software [27],

according to which the *FMEP* depends on in-cylinder maximum pressure and engine speed by means of the following law:

$$FMEP = A + B \cdot P_{\max} + C \cdot n + D \cdot n^2 \quad (2)$$

Eq. (2) shows that the Chen & Flynn model estimates the overall FMEP, making use of few global variable, typically one related to the engine load and the other related to the engine speed, in order to separately account both the energy dissipated by friction due to gas thrust and the energy losses influenced by the speed (e.g. those related to inertia forces). In this work, a modified version of the Chen–Flynn model [28] was adopted for the calculation of the friction mean effective pressure; in this modified version, the normalized mean piston speed *S* was adopted instead of engine speed, and the indicated mean effective pressure *IMEP* was considered as a pressure load-related variable instead of the maximum in-cylinder pressure:

$$FMEP = A + B \cdot IMEP + C \cdot S + D \cdot S^2 \quad (3)$$

Through a least squares regression process performed on the experimental *BMEP* and *IMEP* data shown in **Figure 4** and **Figure 6**, the values of the four parameters (*A*, *B*, *C* and *D*) were obtained (reported in Table 1).

Table 1. Parameters determined for the Chen & Flynn FMEP model

***A* [bar]**	0.63
***B* [-]**	0.0398
***C* [bar]**	-0.00341
***D* [bar]**	0.00366

Once the parameters of the *FMEP* model were determined, the author adopted the experimental *IMEPexp* values shown in **Figure 4** for the gasoline fuelled reference engine, while the *BMEP* values were obtained, for each speed and load, by the application of the *FMEP* model:

$$BMEP_{gasoline} = IMEP_{\exp} - FMEP \tag{4}$$

As regards the air-fuel ratio, the values shown in **Figure 5** were adopted for the full load conditions (i.e. *MAP=1 bar*), while a stoichiometric mixture (i.e. λ=1) was assumed for MAP values lower than 0.9 bar, being the stoichiometric air-fuel ratio $\alpha_{F,st}$=14.7 for gasoline. For the intermediate operating points with *MAP* between 0.9 and 1 bar, a linear variation of the air-fuel ratio was assumed. The engine indicated efficiency was evaluated starting from the relation between *IMEP* and the engine operating parameters:

$$IMEP = \frac{\delta_A \cdot \lambda_V \cdot LHV}{\lambda \cdot \alpha_{F,st} + \frac{1}{\delta'}} \cdot \eta_i \tag{5}$$

Where *LHV* is the gasoline lower heating value (assumed 43 MJ/kg), η_i the indicated engine efficiency, δ_A the air density in the manifold and δ' the relative fuel density, i.e. the ratio between fuel and air density:

$$\delta' = \delta_F / \delta_A \tag{6}$$

For a multi-point indirect gasoline injection, it is plausible to assume that 40% of the fuel evaporates before entering the cylinder, then the average fuel density δ_F is:

$$\delta_F = \delta_{F,V} \cdot 0.4 + \delta_{F,L} \cdot 0.6 \tag{7}$$

being $\delta_{F,L}$ and $\delta_{F,V}$ the fuel density of the liquid and vapour phase respectively. The vapour fuel density was evaluated assuming the perfect gas law with a gasoline molecular mass of 100 g/mol [29].

The gross indicated mean effective pressure $IMEP_{g,gasoline}$ of the gasoline fuelled engine was hence calculated on the basis of the $IMEP_{\exp}$ values:

$$IMEP_{g,gasoline} = IMEP_{\exp} + PMEP \tag{8}$$

where the pumping mean effective pressure *PMEP* was simply assumed as:

$$PMEP = MAP - p_{S0} \tag{9}$$

The term p_{S0} represents the in-cylinder pressure during the exhaust stroke of the baseline naturally aspirated engine, here considered $=1.10\ p_0$ to account for the pressure drop in the exhaust pipe. The gross indicated efficiency of the gasoline naturally aspirated engine was hence calculated from the gross indicated mean effective pressure:

$$\eta_{i,g,gasoline} = \frac{IMEP_{g,gasoline} \cdot \left(\lambda \cdot \alpha_{F,st} + \frac{1}{\delta'} \right)}{\delta_A \cdot \lambda_V \cdot LHV} \tag{10}$$

According to the simple approach followed in this analysis, the modeling of the CNG fuelled naturally aspirated engine was performed assuming the same gross indicated efficiency of the gasoline fuelled engine for the same operating points (i.e. the same MAP level and engine speed). According to this simplifying assumption, the gross indicated efficiency of the CNG fuelled engine $\eta_{ig,CNG}$ was determined starting from the gross indicated efficiency $\eta_{ig,gasoline}$ of the gasoline fuelled engine:

$$\eta_{ig,CNG}\left(MAP,S\right) = \eta_{ig,gasoline}\left(MAP,S\right) \tag{11}$$

Considering the volumetric efficiency of the engine expressed as the ratio between the mass of fuel-air mixture m_m $(=m_{air}+m_{fuel})$ actually introduced in the engine at each cycle and the theoretical mass $(V \cdot \delta_m)$:

$$\lambda_V = \frac{m_m}{V \cdot \delta_m} = \frac{m_m}{V \cdot \delta_a} \cdot \frac{\alpha_F + 1/\delta'}{\alpha_F + 1} \tag{12}$$

another plausible assumption was made on the volumetric efficiency of the CNG engine supposed equal to the gasoline fuelled engine:

$$\lambda_{V,CNG} = \lambda_{V,gasoline} \tag{13}$$

It is worth noting that the assumption made does not imply that the same amount of air enters both CNG and gasoline fuelled engine, due to the very different relative density δ' of the two fuels.

The gross indicated mean effective pressure of the CNG fuelled naturally aspirated engine was then determined as:

$$IMEP_{g,CNG} = \frac{\delta_A \cdot \lambda_v \cdot LHV_{CNG}}{\lambda \cdot \alpha_{F,st} + \frac{1}{\delta'}} \cdot \eta_{i,g,CNG} \tag{14}$$

Given the very high knock resistance of natural gas, and supposing to adopt the same volumetric compression ratio of the gasoline baseline engine, the CNG-powered engine was assumed to run always with stoichiometric air-fuel ratio (i.e. λ=1). Considering that rich mixtures cause low combustion (and hence indicated) efficiency, to account for the different mixture strengths adopted with the two fuels, the author corrected the indicated efficiency of the CNG-powered engine employing as correction factor the combustion efficiency published in [28] and reported in the diagram of Figure 7, thus obtaining the indicated gross efficiency of the CNG fuelled engine operating at the stoichiometric air-fuel ratio:

$$\eta_{i,g,CNG} = \eta_{i,g,gasoline} \frac{\eta_{comb}(\lambda = 1)}{\eta_{comb}(\lambda_{gasoline})} \tag{15}$$

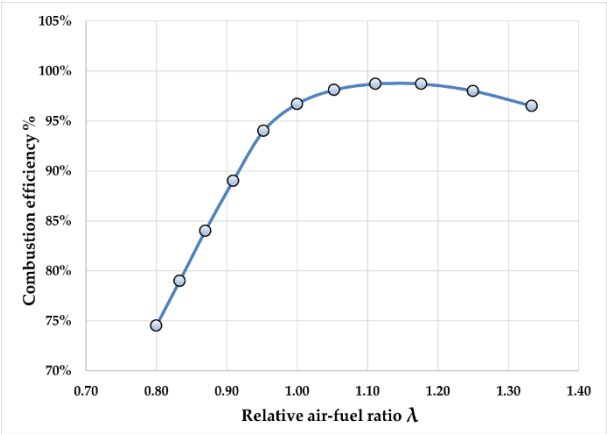

Figure 7. Spark ignition engines combustion efficiency as function of the relative air-fuel ratio λ

Where $\eta_{comb}(\lambda_{gasoline})$ is the combustion efficiency related to the gasoline relative air-fuel ratio λ.

For the determination of the chemical-physical properties of the Natural Gas, the author employed the data provided by a local natural gas supplier (see Table 2). The data shown in Table 2 allowed to calculate the CNG relative fuel density ($\delta'=0.64$), and hence the gross indicated mean effective pressure of the CNG fuelled engine, for each operating condition.

Table 2. Composition and properties of the Natural Gas considered [30]

Methane – CH_4	**[% mole of fuel]**	86.49%
Ethane – C_2H_6	**[% mole of fuel]**	8.79%
Propane – C_3H_8	**[% mole of fuel]**	1.18%
Nitrogen – N_2	**[% mole of fuel]**	1.32%
Carbon dioxide – CO_2	**[% mole of fuel]**	1.89%
Other	**[% mole of fuel]**	0.33%
Specific gas constant – R_{CNG}'	**[J·kg^{-1}·K^{-1}]**	451.42
Lower Heating Value	**[MJ kg^{-1}]**	46.93
Hydrogen/Carbon Ratio	**[-]**	3.78

The indicated mean effective pressure of the baseline CNG engine could be then evaluated through the *PMEP* of equation (9):

$$IMEP_{CNG} = IMEP_{g,CNG} + \left(MAP - p_{S0}\right) \tag{16}$$

Since it is realistic to assume that the constants *A*, *B*, *C* and *D* of the *FMEP* model remain unchanged when changing kind of fuel, the $FMEP_{CNG}$ was evaluated on the basis of the $IMEP_{CNG}$ through equation (3). The $BMEP_{CNG}$ could be hence calculated as:

$$BMEP_{CNG} = IMEP_{CNG} - FMEP_{CNG} \tag{17}$$

and the resultant brake thermal efficiency, as well as brake specific fuel consumption, could be evaluated:

$$\eta_{br,CNG} = \frac{BMEP_{CNG} \cdot \left(\lambda \cdot \alpha_{st} + 1/\delta'\right)}{\delta_A \cdot \lambda_V \cdot LHV_{CNG}} \tag{18}$$

$$BSFC_{CNG[g/kWh]} = \frac{3600}{LHV_{CNG[MJ/kg]} \cdot \eta_{br,CNG}} \tag{19}$$

With the aim to pass from the normalized mean piston speed *S* to the effective mean piston speed *Sp*, coherently with the technological level considered for the baseline naturally aspirated engine (European Type C–Medium vehicle), a maximum reference value of $Sp_{(max)}$=17 *m/s* was assumed.

As final result, Figure 8 shows the BSFC contour map obtained for the baseline CNG spark ignition engine as function of mean piston speed *S* and *BMEP*. The same figure also shows the full load *BMEP* of the CNG fuelled naturally aspirated engine. As already mentioned, each engine considered in this study was sized to provide the target maximum output power of 73.5 kW (100 HP); given the full load *BMEP* values of Figure 8, the necessary engine displacement V_A of the CNG fuelled naturally aspirated engine resulted 1610 cc.

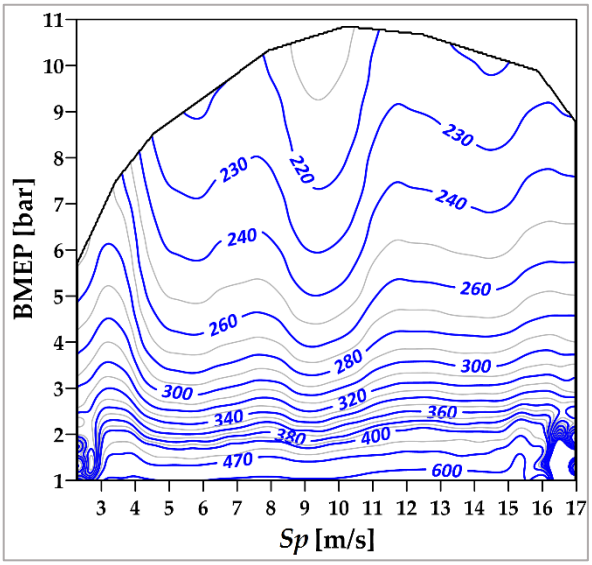

Figure 8. Brake specific fuel consumption map of the CNG fuelled naturally aspirated engine

Table 3. Main characteristics of the baseline CNG fuelled S.I. naturally aspirated engine

Engine	4-stroke, naturally aspirated, spark ignition
Displacement	1610 cc
Number of cylinders	4
Bore	77.28 mm
Stroke	85.78 mm
Max mean piston speed	17 m/s
Compression ratio	11
Injection system	CNG multi-point injection
Valvetrain	4 valves/ cylinder, VVT
Max BMEP	10.85 bar at 3567 rpm
Max Power	73.5 kW at 5549 rpm
Min BSFC	206.8 g/kWh

4. Reference Turbocharged Engine

As already mentioned, the advantages connected to the implementation of the separated electric compound SI CNG engine were compared to a reference traditional turbocharged CNG engine, whose performances are evaluated in this section.

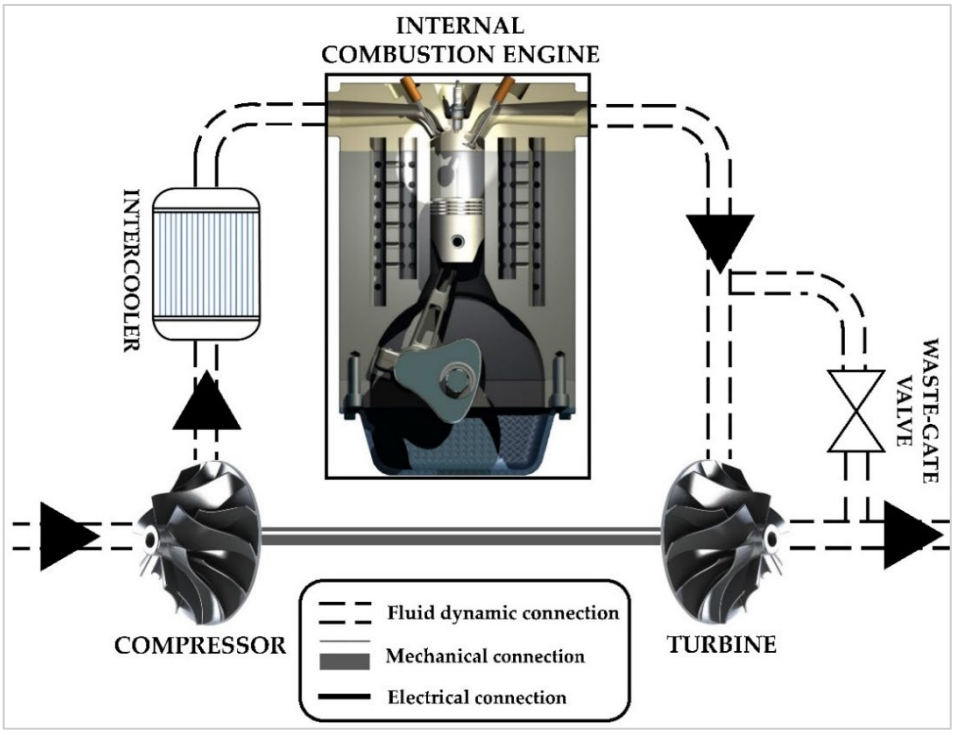

Figure 9. Reference turbocharged engine scheme

The scheme of the reference turbocharged CNG engine is represented in **Figure 9**: the turbocharger is composed by the turbine and the turbocompressor which are mechanically linked to each other, and both fluid-dynamically connected to the engine. Figure 9 also shows the presence of a waste-gate valve for the turbine by-pass, and an intercooler between engine and compressor for cooling down the air charge. Given the high knock resistance of natural gas [31–32] and the relatively low engine compression ratio adopted (i.e. 11), for the CNG fuelled turbocharged engine a maximum boost pressure of 1.85 bar was assumed. Based on the

specific parameters of the baseline CNG naturally aspirated engine, the performances of the turbocharged engine were then determined.

As first step, the author calculated the air mass flow to the engine, which, for each *MAP* and mean piston speed *Sp* is:

$$G_{TC} = \frac{V_{TC} \cdot n}{60 \cdot \varepsilon} \cdot \delta_{TC} \cdot \lambda_{V,TC} \frac{\alpha_F}{\alpha_F + 1/\delta'} \tag{20}$$

where V_{TC} is the turbocharged engine displacement, n is the speed of rotation, $\lambda_{V,TC}$ the volumetric efficiency; δ_{TC} is the air density at the engine inlet, evaluated through the ideal gas law:

$$\delta_{TC} = \frac{MAP}{R'_{air} \cdot T_{TC}} \tag{21}$$

Which in turns depends on the intercooler outlet temperature T_{TC} and on the manifold absolute pressure *MAP*. The compressor outlet temperature was estimated as:

$$T_{TC}' = T_0 \cdot \left(1 + \frac{\beta_C^{\frac{k_c - 1}{k_c}} - 1}{\eta_{TC}} \right) \tag{22}$$

Where η_{TC} is the compressor adiabatic efficiency (whose evaluation is described further on), $\beta_C = p_c / p_0$ the compression ratio, and k_C the isentropic coefficient. Assuming a plausible intercooler efficiency value R_{INT} equal to 0.7, it was possible to determine the temperature of the air inlet to the engine:

$$T_{TC} = T_{TC}' - R_{INT} \left(T_{TC}' - T_0 \right) \tag{23}$$

The volumetric efficiency of the turbocharged CNG engine $\lambda_{V,TC}$ was evaluated from the volumetric efficiency of the naturally aspirated CNG engine λ_{V0} for each mean piston speed *Sp* and corrected through two factors.

The first correction considers the variation of the pressure difference between the engine inlet and exhaust, while the second is instead linked to the increased inlet temperature to the engine (which, as known, increases the volumetric efficiency) due to the compression from the ambient to the turbocharging pressure. For the evaluation of the first correction factor, a simple approach usually adopted in academic courses was followed:

$$\frac{\lambda_V'(n)}{\lambda_V(n)} = 1 + \frac{MAP - p_S}{k \cdot MAP \cdot (\rho - 1)} \tag{24}$$

Obviously, this correction factor is unitary when no pressure difference exists between inlet and exhaust. Considering that the exhaust back pressure p_{S0} of the baseline naturally aspirated engine was assumed higher than the atmospheric pressure ($p_{S0}=1.1\ p_0$, as mentioned before), to take into account the variation of the difference among inlet and exhaust pressure due to both *MAP* and p_S variation, the author employed equation (24) as follows:

$$\frac{\lambda_V(Sp)}{\lambda_{V0}(Sp)} = \frac{1 + \dfrac{MAP - p_S}{k \cdot MAP \cdot (\rho - 1)}}{1 + \dfrac{p_0 - p_{S0}}{k \cdot p_0 \cdot (\rho - 1)}} \tag{25}$$

where, as already mentioned, the volumetric efficiency λ_{V0} of the baseline naturally aspirated engine was considered at the exhaust pressure p_{S0} and at the manifold pressure p_0. As regards the second correction factor, which accounts for the increased inlet temperature due to compression, the author adopted the classical relation:

$$\frac{\lambda_V(Sp)}{\lambda_{V0}(Sp)} = \sqrt{\frac{T_{TC}}{T_0}} \tag{26}$$

Therefore, combining equations (25) and (26), the volumetric efficiency $\lambda_{V,TC}$ of the turbocharged engine was evaluated:

$$\lambda_{V,TC}(Sp) = \lambda_{V,0}(Sp) \cdot \sqrt{\frac{T_{TC}}{T_0}} \cdot \left[\frac{1 + \frac{MAP - p_S}{k \cdot MAP \cdot (\rho' - 1)}}{1 + \frac{p_0 - p_{S0}}{k \cdot p_0 \cdot (\rho - 1)}} \right] \tag{27}$$

In a turbocharged engine, as shown in **Figure 9**, the power required by the compressor POW_{comp} to compress the air mass flow G_{TC} is supplied by the turbine, whose power output is POW_{turb}. The power balance is hence:

$$POW_{compr} = POW_{turb} \tag{28}$$

Being the power required by the turbocompressor:

$$POW_{compr} = G_{TC} \cdot cp_c \cdot \frac{T_0}{\eta_{TC}} \cdot \left(\beta_C^{\frac{k_c - 1}{k_c}} - 1 \right) \tag{29}$$

And the turbine output-power:

$$POW_{turb} = G_T \cdot cp_S \cdot \eta_{T,TC} \cdot T_S \cdot \left(1 - \beta_T^{\frac{1 - k_s}{k_s}} \right) \tag{30}$$

where T_0 and T_S are the gas temperature at compressor and turbine inlet respectively, cp_c and cp_S are the specific heat at constant pressure of fresh air and exhaust gas respectively, $\eta_{T,TC}$ is the efficiency of turbine (whose calculation procedure is described below), G_T is the turbine mass flow and β_T the turbine pressure ratio. It is worth to point out that the turbine pressure ratio β_T was defined as:

$$\beta_T = \frac{p_S - \Delta p_1}{p_0 + \Delta p_2} \tag{31}$$

Being p_s the in-cylinder gas pressure during exhaust stroke, Δp_1 the pressure drop up the turbine inlet, and Δp_2 the pressure drop between turbine outlet and ambient pressure p_0; it results hence that the overall exhaust pressure drop from cylinder to ambient is:

$$\Delta p_{TOT} = p_S - p_0 \tag{32}$$

In this thesis, for simplicity purpose, the overall exhaust pressure drop was considered unchanged with respect to the baseline engine, and composed of two equal parts, thus obtaining:

$$\Delta p_1 = \Delta p_2 = 0.5 \cdot \Delta p_{TOT} = 0.5 \cdot \left(p_{S0} - p_0 \right) \tag{33}$$

Focusing on the turbocharger, the turbine mass flow G_T and the compressor mass flow G_{TC} are connected through the relationship:

$$G_T = \Omega \cdot G_{TC} \frac{\alpha_F + 1}{\alpha_F} \tag{34}$$

Where the term $\left(\frac{\alpha_F+1}{\alpha_F}\right)$ is due to the fuel mass flow (which is added to the air mass flow downstream the compressor), while Ω represents the portion of exhaust mass flow that is not by-passed by the waste-gate valve (common values of Ω lie between 1 and 0.4). According to the power balance of equation (28), the turbocharging compression ratio can be expressed as:

$$\beta_C = \left[1 + \Omega \cdot \frac{\alpha_F + 1}{\alpha_F} \cdot \frac{cp_S}{cp_C} \cdot \frac{T_S}{T_0} \cdot \eta_T \cdot \eta_C \cdot \left(1 - \frac{1}{\beta_T^{\frac{k_S - 1}{k_S}}} \right) \right]^{\frac{k_c}{k_c - 1}} \tag{35}$$

In the calculations performed, the parameter Ω related to the waste-gate opening was adaptively reduced to prohibit exceeding the maximum allowed value of compression ratio β_C (i.e. 1.85). For the evaluation of the exhaust gas temperature at the pressure p_s another simple equation usually adopted in academic courses was adopted:

$$T_S = T_{IVC} \cdot \frac{p_S}{MAP} \cdot \frac{\left(k_S - 1\right)}{k_S} + \frac{T_{EVO}}{T_{IVC}} \cdot \frac{1}{k_S} \tag{36}$$

Where T_{IVC} represents the inlet temperature at intake valve closure (IVC) of the turbocharged engine, whose value has been assumed, equal to the gas

temperature at the intercooler outlet T_{TC}, while T_{EVO} is the in-cylinder gas temperature at the exhaust valve opening (EVO) and k_S the isentropic coefficient of the exhaust gas. Experimental data and scientific literature report, for a spark ignition engine, values of the ratio T_{EVO}/T_{IVC} ranging from 3.5 to 4.5, depending on the particular engine and on the operating condition. In this work the temperature ratio T_{EVO}/T_{IVC} was assumed to remain constant, apart from engine load and speed. However, with the aim of investigating the effects of its variation on the performance of the whole system, three different values were selected, i.e. T_{EVO}/T_{IVC} =3.5, 4.0 and 4.5, and the entire calculation procedure was repeated for each of the three values.

The isentropic coefficient k_S was evaluated according to perfect gas hypothesis:

$$k_S = \frac{c_{p,S}(T_S)}{c_{v,S}(T_S)} \tag{37}$$

$$c_{v,S}(T_S) = c_{p,S}(T_S) - R_S' \tag{38}$$

Being R_S' the burned gas constant, $c_{v,S}$ the constant volume specific heat (evaluated at the exhaust gas temperature T_S). Obviously, the thermochemical properties of the burned gas were calculated as weighted average on the basis of the chemical composition, i.e:

$$c_{p,s} = c_{p,CO_2}(T_s)\cdot x_{CO_2} + c_{p,H_2O}(T_s)\cdot x_{H_2O} + c_{p,N_2}(T_s)\cdot x_{N_2} \tag{39}$$

$$R'_s = R'_{CO_2}\cdot x_{CO_2} + R'_{H_2O}\cdot x_{H_2O} + R'_{N_2}\cdot x_{N_2} \tag{40}$$

being x the mass fraction of each chemical species in the burned gas: to this purpose, the combustion of a hydrocarbon with H/C=3.78 was considered for the calculation of each mass concentration (see

Table 2). It is worth noting that in both equations (39) and (40) no carbon monoxide is considered, due to the assumption that the CNG-powered engine was never fuelled with rich air-fuel mixtures. The constant pressure specific heat of each chemical species in the burned gas was evaluated as a function of the exhaust gas temperature T_S through the Shomate equations and the coefficients available on the NIST Chemistry WebBook [33].

The calculation of the power produced by the turbine requires the turbine characteristic curves correlating the pressure ratio to the gas mass flow for each speed of rotation. According to the simple approach followed in this model, a single fitting curve was adopted to describe the turbine mass flow parameter MFP as a function of the pressure ratio β_T, whose mathematical expression is:

$$MFP = \frac{a \cdot b + c \cdot \beta_T^d}{b + \beta_T^d} \tag{41}$$

The values of the function parameters a, b, c and d were obtained by means of a least square regression procedure performed on the performance data of a market available product (IHI RHF3). The turbine mass flow G_T could be then obtained from the MFP:

$$G_T = MFP \frac{p_S}{\sqrt{T_S}} \tag{42}$$

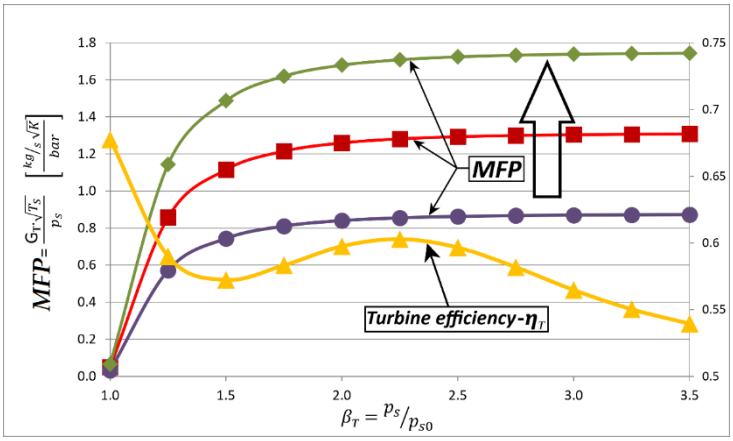

Figure 10:Performance of the exhaust gas turbine (Mass flow parameter and efficiency as function of pressure ratio)

Since in the calculations performed the engine size was iteratively determined on the basis of the specific performance obtained, the MFP curve of equation (41) was amplified or reduced in order to adapt the turbine size and swallowing capacity to the displacement and performance of the engine under analysis: as example, **Figure 10** shows the MFP curves related to three different turbine sizes. The data available on the mentioned commercial product also allowed to express the turbine efficiency as a function of the pressure ratio β_T by means of the polynomial function:

$$\eta_T = -\frac{292.1}{10^4}\beta_T^5 + \frac{3933}{10^4}\beta_T^4 - 2.049\beta_T^3 + 5.113\beta_T^2 - 6.072\beta_T + 3.321 \qquad (43)$$

The resulting efficiency curve η_T is also reported in **Figure 10**.

The performance map of the IHI RHF3 series turbocharger was also used for the evaluation of the compressor efficiency η_c. As done for the turbine, an iterative resizing procedure was carried out to best adapt also the compressor size to the engine. For this aim, the turbocharger map was recursively adapted by modifying the minimum and maximum values on both axis (β_C, G_{TC}) thus maintaining the compressor operating points within the scaled map, as shown in **Figure 11**.

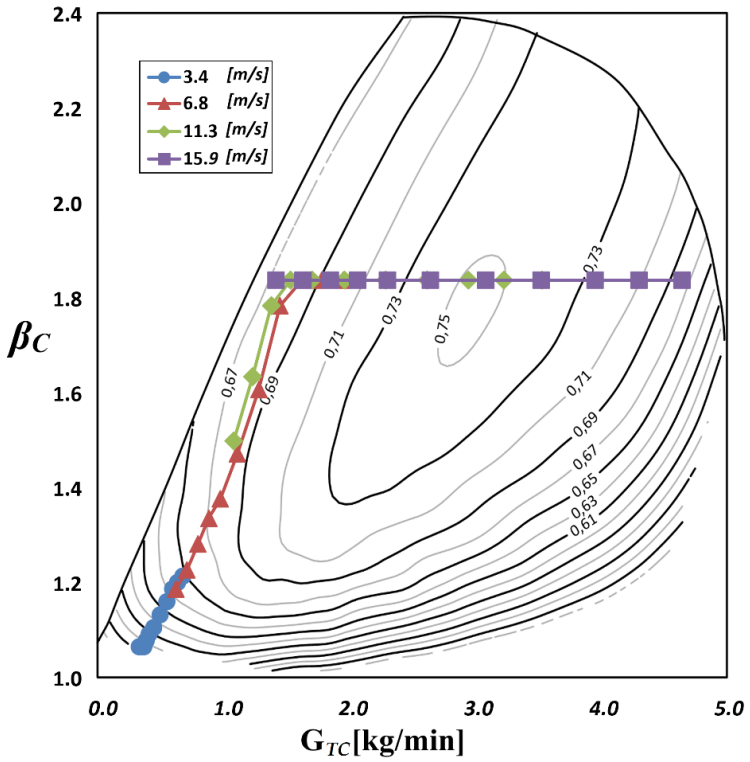

Figure 11: Turbocharger performance map with reported the operating points obtained for every engine load and four mean piston speeds

The calculation of the operating parameters of the turbocharger requires hence, for each mean piston speed *Sp* (from 2.3 to 17.0 m/s) and *MAP* (from 0.78 bar up to 1.85 bar), the recursive solution of the equations from (24) to (43). Once the system of equations is solved, the condition of the gas at engine inlet and outlet are known, then the performance of the turbocharged engine may be evaluated. The described iterative adaptation of the turbocharger size represents somehow the procedure usually employed when selecting and matching a turbocharger to a specific engine.

As a starting hypothesis for the mathematical modeling of the turbocharged engine, the author assumed that the same gross indicated efficiency is obtained at the same normalized MAP and mean piston speed, even if with different absolute manifold pressures. This is obvious a simplifying assumption, which underestimates the efficiency of the turbocharged

engine, which should be instead slightly higher with respect to the naturally aspirated version.

Defining the normalized MAP as:

$$\phi = \frac{MAP}{MAP_{\max}} \tag{44}$$

according to the hypothesis made, the gross indicated efficiency of the turbocharged engine $\eta_{ig,TC}$ was determined starting from the gross indicated efficiency of the naturally aspirated engine $\eta_{ig,CNG}$:

$$\eta_{ig,TC}\left(\phi, Sp\right) = \eta_{ig,CNG}\left(\phi, Sp\right) \tag{45}$$

Once established the gross indicated efficiency for each operating point, it was possible to obtain the gross indicated mean effective pressure $IMEP_{g,TC}$ of the turbocharged engine as:

$$IMEP_{g,TC} = \frac{\delta_{TC} \cdot \lambda_{V,TC} \cdot LHV}{\alpha_F + 1/\delta'} \cdot \eta_{ig,TC} \tag{46}$$

And, in turn, the net indicated mean effective pressure $IMEP_{TC}$:

$$IMEP_{TC} = IMEP_{g,TC} + PMEP_{TC} \tag{47}$$

where the pumping mean effective pressure $PMEP_{TC}$ was simply evaluated as:

$$PMEP_{TC} = MAP - p_S \tag{48}$$

Being the friction mean effective pressure still represented by the same equation (3) adopted for the naturally aspirated engine, the author determined the brake mean effective pressure $BMEP_{TC}$ of the turbocharged engine:

$$BMEP_{TC} = IMEP_{TC} + FMEP_{TC} \tag{49}$$

and the corresponding brake specific fuel consumption $BSFC_{TC}$:

$$BSFC_{TC} = \frac{\delta_{TC} \cdot \lambda_{V,TC}}{BMEP_{TC} \cdot \left(\alpha_F + 1/\delta'\right)} \tag{50}$$

As done in the case of the naturally aspirated engine, the full load $BMEP_{TC}$ values were used to size the displacement V_{TC} of the turbocharged engine necessary to develop the maximum target output power of 73.5 kW. As already pointed out, the entire calculation procedure described in this paragraph was repeated for each assumed value of the temperature ratio T_{EVO}/T_{IVC} (i.e. 3.5, 4.0 and 4.5). **Table 4** resumes the main characteristics and performances determined for the turbocharged CNG fuelled according to the three temperature ratios T_{EVO}/T_{IVC}.

Table 4. Main characteristics of the reference turbocharged engine evaluated for each of the three temperature ratios T_{EVO}/T_{IVC}

Engine	4-stroke, spark ignition		
Injection system	CNG- multi-point injection		
Compression ratio	11		
Valvetrain	4 valves/cylinder, VVT		
Max mean piston speed	17 m/s		
T_{EVO}/T_{IVC}	3.5	4.0	4.5
Number of cylinders	3	3	3
Displacement [cc]	890 cc	826 cc	781 cc
Bore	69.8 mm	68.1 mm	66.8 mm
Stroke	77.5 mm	75.6 mm	74.2 mm
Max BMEP	19.5 bar at 3950 rpm	19.9 bar at 4050 rpm	20.1 bar at 4120 rpm
Max Power	73.5 kW at 6140 rpm	73.5 kW at 6300 rpm	73.5 kW at 6420 rpm
Min BSFC	201.2 g/kWh	199.3 g/kWh	197.9 g/kWh

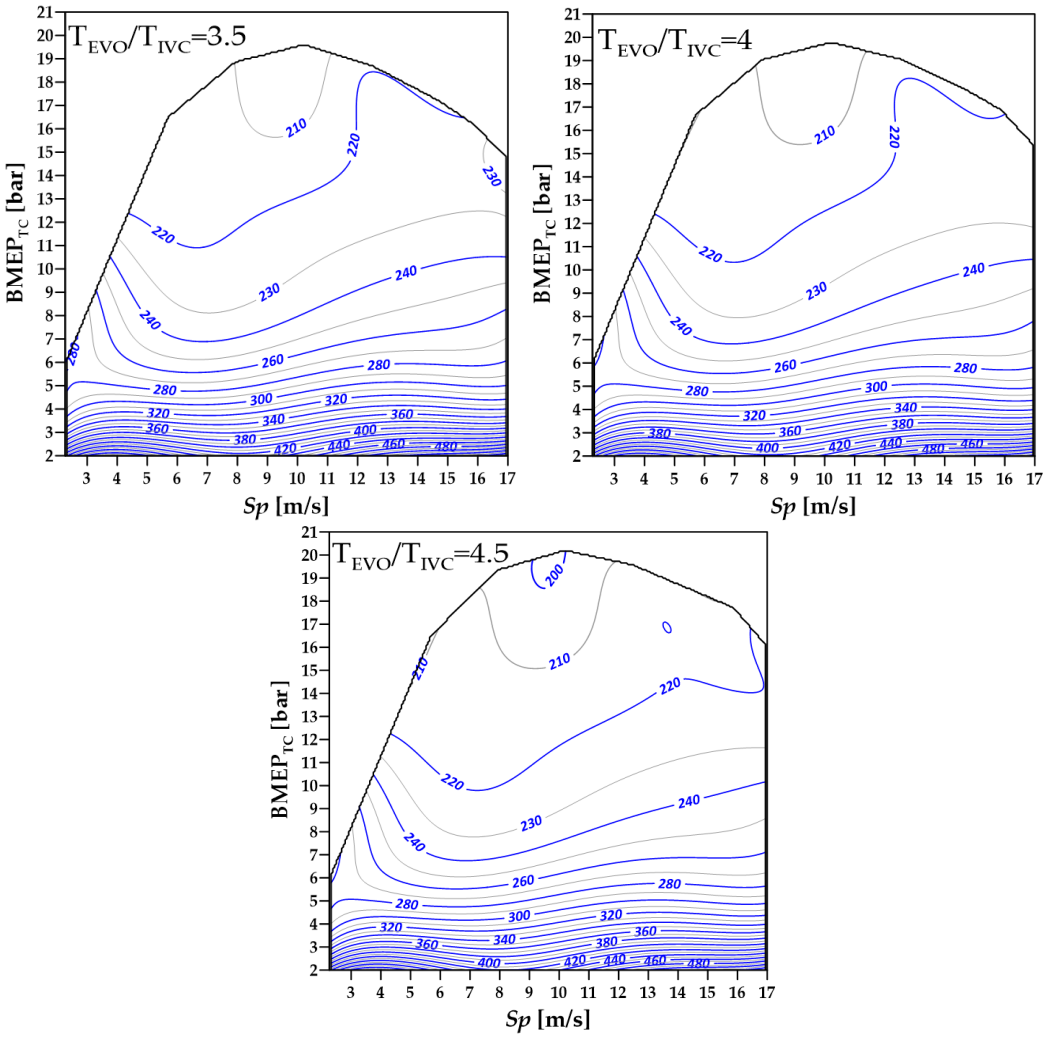

Figure 12: Brake specific fuel consumption map of the reference turbocharged engine with: T_{EVO}/T_{IVC} =3.5; T_{EVO}/T_{IVC} =4.0; T_{EVO}/T_{IVC} =4.5

The contour map of the brake specific fuel consumption obtained for the three cases considered are reported in **Figure 12**.

5. Preliminary separated electric turbo compound engine

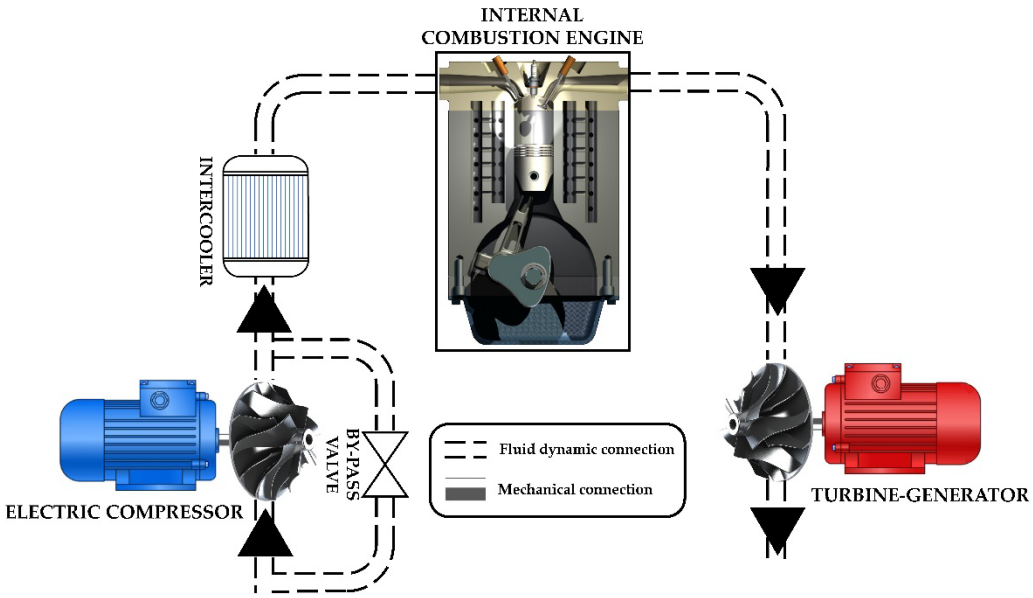

Figure 13: Schematic representation of the separated electric compound engine

This section describes the calculation algorithm developed to evaluate the performance of the proposed compound engine, which will be finally compared to the reference turbocharged engine developed in the previous section. **Figure 13** shows the schematic representation of the compound system proposed in this work, composed of a spark ignition engine supercharged by an electrical powered turbocompressor, and endowed of a turbine-generator group dedicated to recover the unexpanded gas energy of the exhaust gas; Figure 3 instead reports a possible hybrid architecture endowed of the electric compound engine: as already clarified, in the system conceived, the energy recovered by the turbine-generator is stored in the energy storage system of the vehicle and used for the vehicle propulsion. As can also be noted in **Figure 13**, a by-pass valve between the compressor inlet and outlet allows to power off the compressor in the part load operation, when MAP lower than 1 bar is required, thus reducing the power absorption of the supercharging system. As already pointed out, the turbine-generator group is instead considered to operate permanently, in

order to recover as much energy as possible from the exhaust gas. As regards the sizing of the turbocompressor, the author followed the same procedure and calculation algorithm already described in the previous paragraph for the reference turbocharged engine. It is worth noting that the author hypothesized the use of a turbocompressor being the most used in the automotive field; however, nothing prevents from the adoption of a different machine, as example a Roots type or a screw compressor. It must be also pointed out that the turbine considered for this application substantially differs from the turbines commonly employed for turbocharging purpose, which provide only the power necessary to drive the compressor and are designed to comply with wide variations of speed and mass flow, thus resulting not optimized for steady state operation. For this reason, the turbines developed for turbocharging application are low-inertia single radial stage machines, with conversion efficiencies far from the values reached by turbines used in stationary systems. This clarifies that the turbo-generator here considered, as well as the whole hybrid propulsion system, is not commercially available at the moment. The only commercially available products are composed of a radial turbine for turbocharging application connected to an electric generator [34-36] and are designed exclusively to supply the electric accessories of traditional vehicles, thus producing maximum output power within 6 kW. Given the lack of adequate references on the market, as therefore in the scientific literature, for a preliminary evaluation of the performances of the separated electric compound engine the author considered a constant turbine thermomechanical efficiency $\eta_{T,tm}$ (i.e. the product of the total to static isentropic efficiency $\eta_{t,s}$ and the mechanical efficiency η_m). Given this lack of previous studies, for a first evaluation of the performance of the compound

engine, it was not possible to predict exactly the effective efficiency of the exhaust gas turbine: on account of this, the author decided to consider two different efficiency levels, thus assessing the effect of this parameter on the overall energetic performance of the entire compound system. In detail, the two levels of thermomechanical efficiency considered for the compound engine turbine are $\eta_{T,tm}=0.70$ and $\eta_{T,tm}=0.75$. As already mentioned, the two efficiency values of the exhaust gas turbine are substantially higher than a common turbocharging turbine, due to the dedicated and optimized turbine design for steady state power production, the analysis of which is dealt with in the next section of this thesis.

As already done in the case of the reference turbocharged engine, the performances of the compound engine were evaluated for each *MAP* (from 0.78 bar to the maximum allowed 1.85 bar) and mean piston speed *Sp* (from 2.3 to 17.0 m/s). The gross indicated mean effective pressure of the compound engine was evaluated as:

$$IMEP_{g,COMP} = \frac{\delta_{COMP} \cdot \lambda_{V,COMP} \cdot LHV}{\alpha_F + 1/\delta'} \cdot \eta_{ig,COMP} \tag{51}$$

where the inlet air density δ_{COMP} of the compound engine was evaluated by means of equations (21), (22) and (23). For the evaluation of the both indicated gross efficiency $\eta_{ig,COMP}$ and volumetric efficiency $\lambda_{V,COMP}$ some observations are necessary, considering that the exhaust gas turbine will produce an increase in the exhaust gas back pressure p_S. Differently from a traditional turbocharged engine, the effect of the increased exhaust back pressure will certainly be stronger in the compound engine for two main reasons: firstly, because unlike the traditional system, in the proposed compound system, the exhaust gas turbine works with the whole exhaust mass flow relatively high-pressure ratio $\beta_I=p_S/p_{S0}$ (as will be shown further

on). Secondly, the turbo-generator group is considered to remain permanently active, i.e. also for the partial load operation, when engine *MAP* is lower than 1 bar.

As widely known, an increase of the engine exhaust back pressure affects both the indicated and the volumetric efficiency. As concerns the volumetric efficiency, a higher exhaust back pressure causes a higher residual gas mass inside the cylinder, thus limiting the amount of fresh mass that can be introduced during the intake phase. This phenomenon was taken into consideration by means of equation (27) which correlates the volumetric efficiency to the pressure difference between intake and exhaust. As instead regards the indicated engine efficiency, it is known that a higher in-cylinder residual gas fraction (*RGF*) will certainly slowdown the flame propagation speed and worsen the combustion efficiency; however no useful mathematical expressions were found in scientific literature to represent the indicated efficiency deterioration as function of the exhaust back pressure: on account of this lack, the author performed a dedicated series of experimental tests on a bench test (whose detailed description may be found in [37] and [38]) equipped with a 1.242 L port injected spark ignition engine fuelled with CNG and connected to a Schenck W130 eddy current dynamometer; a throttle valve installed in the exhaust pipe was used to modulate the exhaust back pressure, and an AVL GU13X piezoelectric pressure sensor flush mounted in the engine combustion chamber was employed for the in-cylinder pressure measurement, performed with a sample resolution of 1 CAD by the use of a 360 ppr optical encoder connected to the engine crankshaft. The exhaust pressure was evaluated as the average in-cylinder pressure during the exhaust stroke, excluding the blowdown period. The air mass flow was measured by means

of an FCI ST75 Mass Flow Meters, while natural gas mass flow measurement was performed using an Endress+Hauser Coriolis effect PROMASS 80A; an ECM AFRecorder 2400 module was employed to measure both manifold absolute pressure and engine speed. **Table 5** resumes the operating condition of the test: as shown, for each engine speed, the exhaust pressure was increased with steps of 0.1 bar until the occurrence of heavy combustion instability (identified by misfires occurrence), and without exceeding the maximum level of 2 bar. **Table 6** instead reports the measurement accuracy of the instrumentation employed in the experimental test.

Table 5. Operating conditions of the experimental test

Engine speed [rpm]	1500-2500-3500
MAP [bar]	1
Exhaust pressure *ps* [bar]	1.0 to 2.0 in steps of 0.1
Fuel	CNG
Spark advance	Optimal (LPP=15°ATDC)
Air-fuel ratio	Stoichiometric

Table 6. Measurement accuracy of the instrumentation employed in the test

Sensor	**Accuracy**
MAP	±1% FSO (2.38 bar)
Engine Speed	± 10 rpm
NG mass flow	±1% of reading
Air mass flow	±2% reading, ±0.5% full scale
Engine torque	±2% of reading
In-cylinder pressure	linearity error < ±0.3% FSO
In-cylinder pressure	thermal sensitivity shift ≤±0.5% at temperature between 200 and 300°C

The experimental measurements showed that there is a correlation between the increment of the residual gas fraction (defined as the ratio between the residual gas mass and the total in-cylinder mass of gas) and the decrement of the gross indicated efficiency, whose best fit was obtained by the equation:

$$\frac{\eta_{i,g}}{\eta_{i,g,0}} = \frac{1}{1 + b \cdot x^{\gamma}} \tag{52}$$

Where $\left(\frac{\eta_{i,g}}{\eta_{i,g,0}}\right)$ is the ratio between the indicated gross efficiencies measured with and without exhaust throttling, as well as $x=RGF/RGF_0$ is the ratio between the residual gas fractions detected with and without exhaust throttling; the parameters b and γ are correlated to the mean piston speed, which, as shown in **Figure 14.** , has a strong influence on the efficiency variation.

$$b = 0.1384 \cdot Sp^{-2.635} \tag{53}$$

$$\gamma = -0.2556 \cdot Sp + 6.0391 \tag{54}$$

Each residual gas fraction RGF was estimated through the procedure described reported in **Appendix A.**

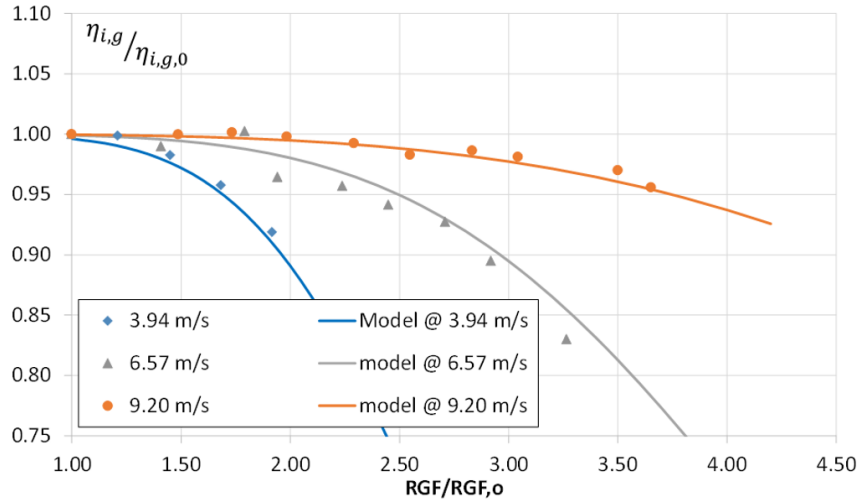

Figure 14. Variation of the engine gross indicated efficiency as function of the RGF ratio

With the same approach followed for the reference turbocharged engine, it was assumed that the gross indicated efficiency is the same for the same engine and the same conditions of normalized MAP ϕ and mean piston speed *Sp*. According to this assumption, the reference gross indicated efficiency of the compound engine $\eta_{i,g,COMP,0}$ (i.e. without exhaust throttling), was evaluated as:

$$\eta_{ig,COMP,0}\left(\phi, Sp\right) = \eta_{ig,CNG}\left(\phi, Sp\right) \tag{55}$$

The residual gas fraction *RGF* and the resulting gross indicated efficiency $\eta_{i,g,COMP}$ of the supercharged compound engine could be hence determined, for each *MAP* and mean piston speed, on the basis of the exhaust gas back pressure p_s through equations (52) to (54). The gross indicated mean effective pressure could be then calculated by the equation (51), which, in turn, allowed to evaluate the compound engine net indicated mean effective pressure $IMEP_{COMP}$:

$$IMEP_{COMP} = IMEP_{g,COMP} + PMEP_{COMP} \tag{56}$$

being the pumping mean effective pressure $PMEP_{COMP}$ estimated through equation (48), as in the case of the reference turbocharged engine. Equation (3) was then employed to evaluate the $FMEP_{COMP}$, and hence the engine $BMEP_{COMP}$ was obtained from equation (49).

Unlike the previous cases, however, in the compound system the exhaust gas turbine actively contributes to the energy production, so the total output power results from the sum of the engine and the turbine contributions. The overall brake mean effective pressure of the whole compound system $BMEP_{TOT,COMP}$ can be hence obtained as:

$$BMEP_{TOT,COMP} = BMEP_{COMP} + RMEP - CMEP \tag{57}$$

Being *RMEP* the recovery mean effective pressure of the exhaust gas turbine, and *CMEP* the compression mean effective pressure, derived from the power required by the motor-compressor. The recovery mean effective pressure *RMEP* was estimated as:

$$RMEP = \frac{60 \cdot \varepsilon \cdot POW_{tur}}{V_{COMP} \cdot n} \tag{58}$$

where POW_{tur} is the power produced by the exhaust gas turbine, V_{COMP} is the displacement of the compound engine and ε is the number of engine revolutions per cycle (2 in a 4-stroke engine). Analogously, the compression mean effective pressure was calculated as:

$$CMEP = \frac{60 \cdot \varepsilon \cdot POW_{comp}}{V_{COMP} \cdot n \cdot \eta_{EM}} \tag{59}$$

where POW_{comp} is the power required by the compressor and η_{EM} is the supply-electric motor chain efficiency. As can be noted, the electric supply chain efficiency of motor driving the compressor was considered, being the motor-compressor group an auxiliary device which affects the system energy balance; the efficiency of the turbine electric generator instead was not considered in the *RMEP* (equation (58)) coherently with the calculation performed for the output power from the internal combustion engine, which was not reduced by the efficiency of the connected electric generator (MG1 in Figure 3).

The power required by the compressor and the power produced by the turbine were evaluated as in the previous paragraph:

$$POW_{comp} = G_{COMP} \cdot cp_c \cdot \frac{T_0}{\eta_c} \cdot \left(\beta_c^{\frac{k_c - 1}{k_c}} - 1 \right) \tag{60}$$

$$POW_{tur} = G_{COMP} \cdot \frac{\alpha + 1}{\alpha_F} \cdot cp_S \cdot \eta_{T,tm} \cdot T_S \cdot \left(1 - \beta_T^{\frac{1-k_S}{k_S}} \right) \tag{61}$$

With the exception that the intake air mass flow of the compound engine is now G_{COMP}, the exhaust gas turbine efficiency has been indicated with $\eta_{T,tm}$, while all the other parameters (e.g. T_S, α_F, β_S, β_C, k_S, k_C, cp_C, cp_S, etc..) have the same meaning as in the previous paragraph (equations(29) and (30)). It is worth to note that, being in this case the expander supposed to permanently work with the entire exhaust gas mass flow, no by-pass exists and hence the term Ω is considered=1.

Being the engine intake air mass flow:

$$G_{COMP} = \frac{V_{COMP} \cdot n}{60 \cdot \varepsilon} \cdot \delta_{COMP} \cdot \lambda_{V,COMP} \frac{\alpha}{\alpha_F + 1/\delta'} \tag{62}$$

The specific performance parameters *RMEP* and *CMEP* hence become:

$$RMEP = \frac{60 \cdot \varepsilon}{V_{COMP} \cdot n} \cdot G_{COMP} \cdot \frac{\alpha_F + 1}{\alpha_F} \cdot c_{p,s} \cdot T_s \cdot \eta_{T,tm} \cdot \left(1 - \beta_T^{\frac{1-k_s}{k_s}} \right) \tag{63}$$

$$CMEP = \frac{60 \cdot \varepsilon}{V_{COMP} \cdot n \cdot \eta_{EM}} \cdot G_{COMP} \cdot cp_c \cdot \frac{T_0}{\eta_C} \cdot \left(\beta_c^{\frac{k_c - 1}{k_c}} - 1 \right) \tag{64}$$

Once determined the overall brake specific performance $BMEP_{TOT,COMP}$ for each operating condition of *MAP* and mean piston speed *Sp*, the overall brake thermal efficiency $\eta_{bTOT,COMP}$ of the compound system can be calculated as:

$$\eta_{b\,TOT,COMP} = \frac{BMEP_{TOT,COMP} \cdot \left(\alpha_F + 1/\delta' \right)}{\delta_{COMP} \cdot \lambda_{V,COMP} \cdot LHV} = \frac{\left(BMEP_{COMP} + RMEP - CMEP \right) \cdot \left(\alpha_F + 1/\delta' \right)}{\delta_{COMP} \cdot \lambda_{V,COMP} \cdot LHV} \tag{65}$$

And hence the related overall brake specific fuel consumption $BSFC_{TOT,COMP}$:

$$BSFC_{TOT,COMP} = \frac{\delta_{COMP} \cdot \lambda_{V,COMP}}{BMEP_{TOT,COMP} \cdot \left(\alpha_F + 1/\delta' \right)} \tag{66}$$

It must be pointed out now that, if on one hand a higher discharge pressure increases the recovery mean effective pressure *RMEP*, on the other hand it also increases the pumping mean effective pressure $PMEP_{COMP}$ (equation (48)) and worsens the gross indicated thermal efficiency, due to the increased amount of residual gas (equation (52)); it is therefore evident that, for each engine load (*MAP*) and mean piston speed (*Sp*), there will be a compromise solution between the advantages and disadvantages resulting from increasing the exhaust back pressure p_s: in other words, for each operating point of the engine, an optimum exhaust pressure exists which maximizes the overall brake thermal efficiency $\eta_{bTOT,COMP}$ of the compound system.

In his calculation, hence, the author carried out an optimization process, searching, for each operating point of the engine, the best exhaust back pressure p_s by maximizing the overall brake thermal efficiency $\eta_{bTOT,COMP}$; since the latter is not a linear or polynomial function of the exhaust pressure, a genetic algorithm was employed for the system efficiency optimization. A genetic algorithm is particularly suitable for the current application because it can generate high-quality solutions to optimization and search problems by relying on biologically inspired operators such as mutation, crossover and selection.

As already done in the case of the turbocharged engine, the entire calculation procedure was repeated for each value of the temperature ratio T_{EVO}/T_{IVC} (namely 3.5, 4.0 and 4.5) and, in addition, for each value of the exhaust gas turbine efficiency $\eta_{T,tm}$ considered (i.e. 0.70 and 0.75).

Figure 15 reports the contour maps of the optimal exhaust pressure levels determined for each overall load $BMEP_{TOT,COMP}$ and mean piston speed *Sp*, considering the case of T_{EVO}/T_{IVC}=4.5, $\eta_{T,tm}$=0.75.

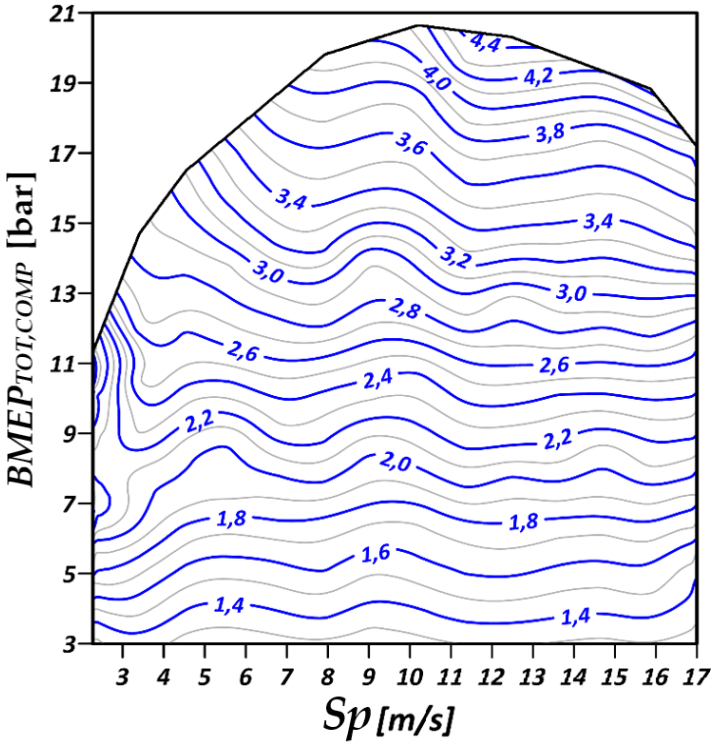

Figure 15. Optimal exhaust pressure levels as function of load and speed (T_{EVO}/T_{IVC}=4.5, $\eta_{T,tm}$=0.75)

As shown, higher exhaust back pressures were obtained for the medium-higher loads, where the higher in-cylinder pressures make easier the recovery of the unexpanded gas energy. As can also be observed, optimal exhaust pressures up to 4.4 bar were determined for the extreme case of T_{EVO}/T_{IVC}=4.5 and $\eta_{T,tm}$=0.75, while in the extreme opposite case (T_{EVO}/T_{IVC}=3.5, $\eta_{T,tm}$=0.70) optimal exhaust pressures up to 3.4 bar were reached; both scenarios, however, revealed exhaust pressure values significantly higher than in a traditional turbocharged engine: these conditions must be adequately considered for a future optimal design of the exhaust gas turbine dedicated to the unexpanded gas energy recovery. The optimization process led to the determination of the maximum $BMEP_{TOT,COMP}$ levels for each design case, and, as consequence, of the compound engine displacement V_{COMP} necessary to develop the maximum target power of 73.5 kW. The resulting main characteristics of the

compound engine for each of the three temperature ratios T_{EVO}/T_{IVC} considered are summarized in **Table 7** for case study $\eta_{T,tm}=0.7$ and in **Table 8** for the case study $\eta_{T,tm}=0.75$. The comparison of these results with the performance obtained by the traditional turbocharged engine (see **Table 4**) allow to observe that the minimum fuel consumption is always lower in the electric compound engine.

Table 7. Main characteristic of the compound engine obtained with $\eta_{T,tm}=0.7$

Engine	4-stroke, spark ignition		
Injection system	CNG multi-point injection		
Valvetrain	4 valves/cylinder, VVT		
Compression ratio	11		
Max boost pressure	1.85 bar		
Turbine efficiency	0.7		
Number of cylinders	3		
Stroke/bore ratio	1.11		
Displacement [cc]	731.1	708.9	695.6
T_{EVO}/T_{IVC}	3.5	4	4.5
Max BMEP$_{TOT,COMP}$	20.11 bar at 4220 rpm	20.34 bar at 4260 rpm	20.51 bar at 4290 rpm
Max output power	73.5 kW at 6560 rpm	73.5 kW at 6630 rpm	73.5 kW at 6670 rpm
Min BSFC$_{TOT,COMP}$	189.2 g/kWh	184.4 g/kWh	179.5 g/kWh
Variation of min BSFC	-6.33%	-8.09%	-10.25%
Max RMEP	4.18 bar at 5150 rpm	4.98 bar at 5210 rpm	5.86 bar at 5240 rpm
Max RMEP/BMEP$_{TOT,COMP}$	24.20%	29.70%	36.40%
Max turbine power	15.16 kW at 6560 rpm	17.82 kW at 6630 rpm	21.00 kW at 6670 rpm

More in detail, it can be noted a reduction of the minimum brake specific fuel consumption between 6.33% (in the worst case $T_{EVO}/T_{IVC}=3.5$ and $\eta_{T,tm}=0.7$) and 12.32% (in the best solution case $T_{EVO}/T_{IVC}=4.5$ and $\eta_{T,tm}=0.75$). The contour maps of the overall specific fuel consumption $BSFC_{TOT}$ obtained for the two intermediate cases with $T_{EVO}/T_{IVC}=4.0$, $\eta_{T,tm}=0.7$ and $T_{EVO}/T_{IVC}=4.0$, $\eta_{T,tm}=0.75$ are shown in **Figure 16** and **Figure 17** respectively. As obviously

expected, the two diagrams confirm that the overall fuel consumption of the compound system benefits from a higher turbine efficiency. A comparison between the maps of **Figure 16** and **Figure 17** with the fuel consumption map of the reference turbocharged engine (case b) of **Figure 12**) also allow to observe that both propulsion solutions show similar *BMEP* values, but the compound systems always exhibits a better fuel economy compared to the reference traditional turbocharged cases.

Table 8. Main characteristic of the compound engine obtained with $\eta_{T,tm}=0.75$

Engine	4-stroke, spark ignition		
Injection system	CNG multi-point injection		
Valvetrain	4 valves/cylinder, VVT		
Compression ratio	11		
Max boost pressure	1.85 bar		
Turbine efficiency	0.75		
Number of cylinders	3		
Stroke/bore ratio	1.11		
Displacement [cc]	728.3	697.9	689.3
T_{EVO}/T_{IVC}	3.5	4	4.5
Max BMEP$_{TOT,COMP}$	20.09 bar at 4220 rpm	20.47 bar at 4280 rpm	20.66 bar at 4300 rpm
Max output power	73.5 kW at 6570 rpm	73.5 kW at 6660 rpm	73.5 kW at 6690 rpm
Min BSFC$_{TOT,COMP}$	186.7 g/kWh	181.5 g/kWh	176.2 g/kWh
Variation of min BSFC	-7.76%	-9.85%	-12.32%
Max RMEP	4.74 bar at 5160 rpm	5.53 bar at 5230 rpm	6.59 bar at 5250 rpm
Max RMEP/BMEP$_{TOT,COMP}$	28.40%	33.90%	42.90%
Max turbine power	17.44 kW at 6570 rpm	19.64 kW at 6660 rpm	23.30 kW at 6690 rpm

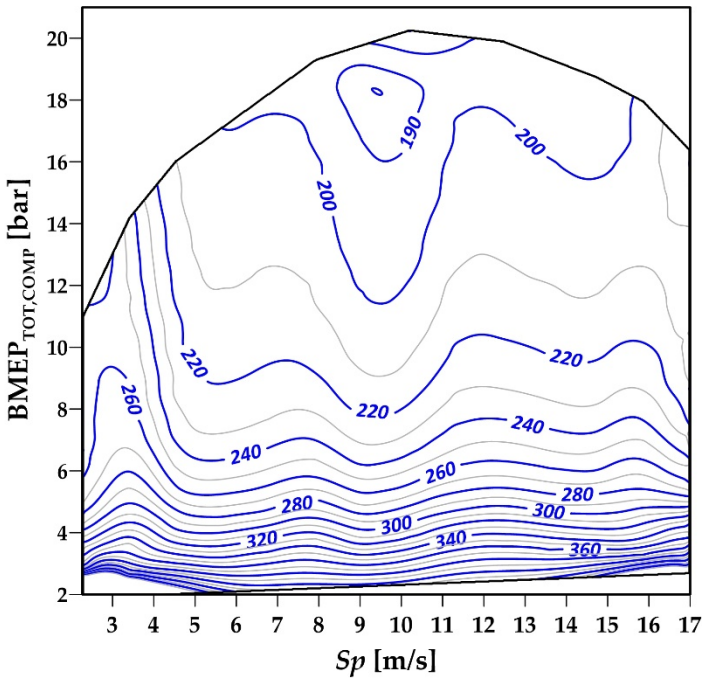

Figure 16. Brake specific fuel consumption [g/kWh] of the compound engine, as function of overall load and mean piston speed (T_{EVO}/T_{IVC} =*4.0*, $\eta_{T,tm}$=0.70)

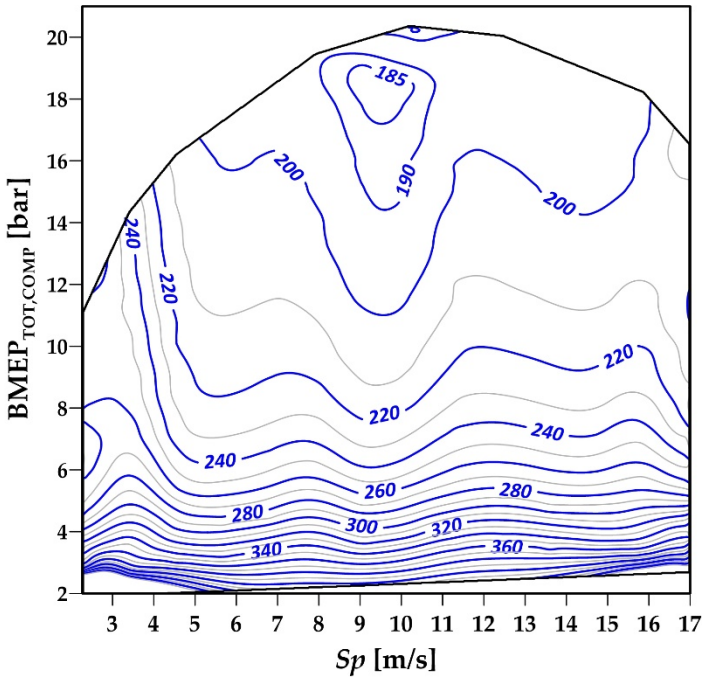

Figure 17. Brake specific fuel consumption [g/kWh] of the compound engine, as function of overall load and mean piston speed (T_{EVO}/T_{IVC}=4.0, $\eta_{T,tm}$ =0.75)

Table 7 and **Table 8** also show the percentage contribution of the exhaust gas turbine to the overall output power of the compound system, revealing maximum power share from 24.2% to 42.9%, the higher results obtained

with the better efficiency turbine ($\eta_{T,tm}=0.75$): according to the modelling approach followed, hence, the power contribution of the exhaust gas turbine to the vehicle propulsion would be relevant; as can also be observed in **Table 7** and **Table 8**, in the optimized system, maximum recovery mean effective pressures between 4.18 bar and 6.59 bar were determined, and maximum power delivered by the exhaust gas turbine between 15.16 and 23.30kW were calculated: once again, the higher values were obtained when the best efficiency turbine ($\eta_{T,tm}=0.75$) was considered. All these results confirm that, if adequately recovered, the unexpanded exhaust gas energy may constitute a relevant part of the whole propulsion energy thus helping to reduce both vehicle fuel consumption and related emissions.

The comparison based only on the minimum specific fuel consumption of the system is not exhaustive and gives a limited representation of the real beneficial effects of the separated electric compound propulsion system. Considering that in a hybrid propulsion system the thermal unit is dedicated to produce the power required for both the vehicle traction and battery charging, the two propulsive solutions should be compared on an equal output power basis. To this purpose, the author evaluated the overall efficiency improvement of the compound system with respect to the reference turbocharged engine, for the same power output and the same mean piston speed; **Figure 18** and **Figure 19** show the results obtained for the two extreme cases ($T_{EVO}/T_{IVC}=3.5$, $\eta_{T,tm}=0.70$) and ($T_{EVO}/T_{IVC}=4.5$, $\eta_{T,tm}=0.75$). As can be observed, the major energetic benefits of the electric compound system are obtained in the high load/speed regions; this can be easily explained considering that higher engine power implies higher in-cylinder pressures and exhaust mass flows: in these conditions the turbine can give a greater contribution to the overall output power of the system

without compromising the engine indicated efficiency, leading to greater exhaust gas energy recovery.

At part load, instead, the recovery of the exhaust gas energy may reveal energetically not convenient; in this condition, differently from a traditional turbocharged engine endowed of a waste-gate valve, the compound system can theoretically decrease the exhaust pressure down to the ambient through an appropriate control on the turbine-generator system. More in detail, the efficiency improvement revealed between 3 and 7% for the minimum power levels, reaching a maximum of about 12.5% in the case of **Figure 18** ($T_{EVO}/T_{IVC}=3.5$, $\eta_{T,tm}=0.70$) and 15.5% in **Figure 19** ($T_{EVO}/T_{IVC}=4.5$, $\eta_{T,tm}=0.75$) for the maximum output power levels. As could be expected, the best efficiency improvements were obtained with the better turbine efficiency ($\eta_{T,tm}=0.75$) and the higher temperatures ratio ($T_{EVO}/T_{IVC}=4.5$). For this reason, a correct study and optimization of the whole compound engine should be carried out with the aim to maximize the energetic advantages. The author considers the results obtained really encouraging, especially if it is noted that the effect of the increased exhaust back pressure was not accounted for in the evaluation of the gross indicated efficiency of the reference turbocharged engine.

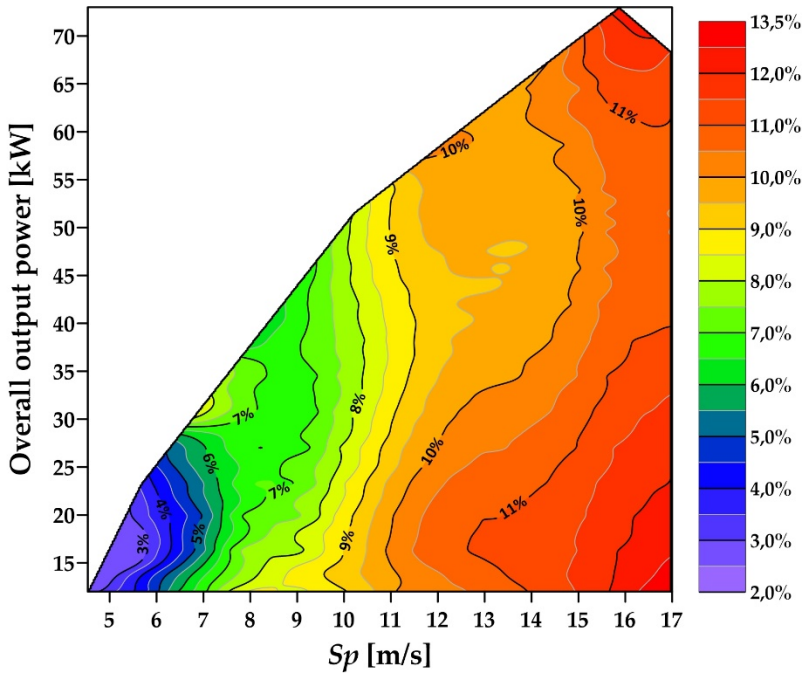

Figure 18. Efficiency improvement of the compound engine with respect to reference turbocharged engine as function of power output and mean piston speed for T_{EVO}/T_{IVC} =3.5 and η_I=0.70

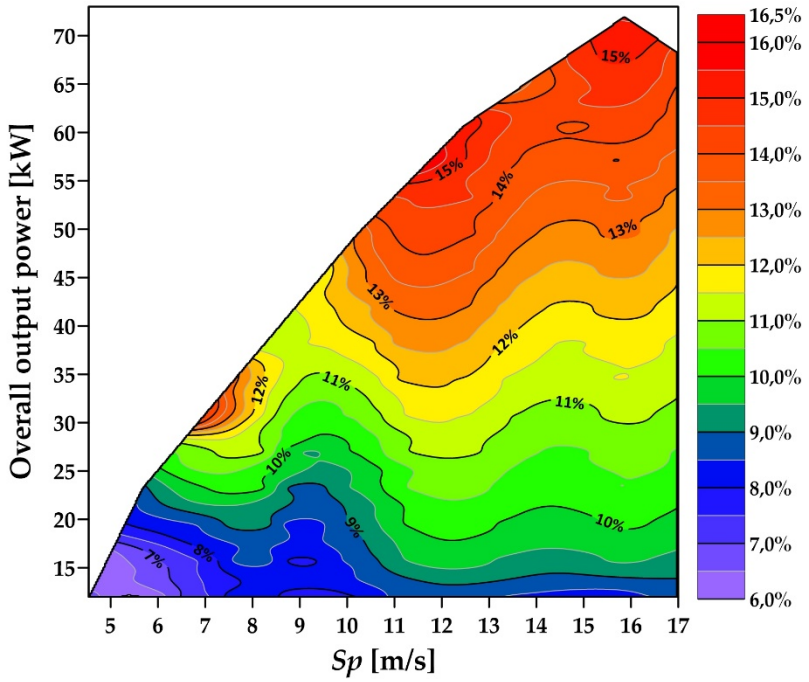

Figure 19. Efficiency improvement of the compound engine with respect to reference turbocharged engine as function of power output and mean piston speed for T_{EVO}/T_{IVC}=4.5 and η_I=0.75

In a hybrid propulsion system the operating point of the thermal unit is usually close to the best efficiency curve, i.e. the curve connecting the

operating conditions which ensure, for each power request, the maximum efficiency; on account of this consideration, the author carried out a further, and fairer, comparison, based on the best efficiency curves of both the compound engine and the reference turbocharged engine. To this purpose, for each output power, the author evaluated the best operating conditions (i.e. with best efficiency) of load and speed, for each of the propulsive systems.

The results of this further comparison for the case study $\eta_{T,tm}=0.75$ are reported in **Figure 20** respectively for all the temperature ratios T_{EVO}/T_{IVC} considered.

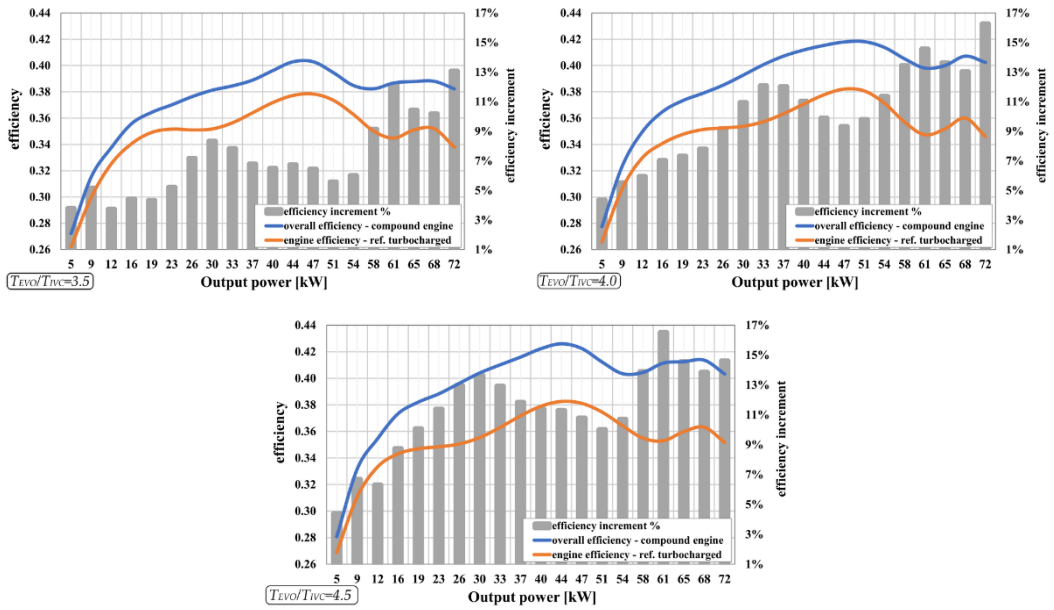

Figure 20. Comparison between the best efficiency curves of the compound engine with respect to reference turbocharged engine for the case of $\eta_{T,tm}=0.75$ and: $T_{EVO}/T_{IVC}=3.5$; $T_{EVO}/T_{IVC}=4.0$; $T_{EVO}/T_{IVC}=4.5$

As shown, the best efficiency curves of the compound system are always higher than the respective curves of the reference turbocharged engine, with efficiency improvement up to 13% for the case of the case of $T_{EVO}/T_{IVC}=3.5$ and $\eta_{T,tm}=0.75$ (case a) of **Figure 20**), and up to 16.5% for the extreme case of $T_{EVO}/T_{IVC}=4.5$ and $\eta_{T,tm}=0.75$ (case c)of **Figure 20**).

Aiming to obtain an average evaluation of the benefit connected with the adoption of the compound system in a hybrid architecture vehicle, from **Figure 20** it can be observed that the average efficiency increments, evaluated on the whole power range, result to be 7.2%, 10.3% and 11.4% for the case a),b) and c) respectively.

The preliminary evaluation performed established that the compound system revealed good potentials in fuel economy improvement and related emission savings in hybrid vehicles; this means that, if adequately recovered, the unexpanded gas energy may constitute a relevant part of the whole propulsion energy, and may contribute to lower both vehicle fuel consumption and related emissions.

6. Radial turbine for the exhaust energy recovery of the separated electric compound engine

As just shown in the preliminary analysis, showed in the previous chapters it was demonstrated that the separated electric compound engine is very promising, as it may achieve overall vehicle efficiency advantages up to 16.5% with respect to a reference hybrid propulsion system of the same nominal overall output power (73.5 kW) equipped with a traditional turbocharged engine.

Furthermore, it was showed that the contribution of the turbo-generator group may reach an impressive 33.9% share of the total power generated by the whole system, with maximum power delivered of 20 kW for the case of $\eta_{T,tm}=0.75$ and $T_{EVO}/T_{IVC}=4$.

In this regard, it must be pointed out that in the preliminary analysis the exhaust gas turbine considered was supposed to be optimized for steady state operation, since in a hybrid propulsion system the thermal engine undergoes small speed and load variations. Quite differently, the turbines usually employed for turbocharging purpose provide only the power required by the compressor and are designed for unsteady operation on account of the strong speed and mass flow variations due to the wide and rapid speed and load variation of the thermal engine. As mentioned above the turbo-generator here considered, as well as the whole hybrid propulsion system, is not commercially available at the moment. The only commercially available products are composed of a radial turbine for turbocharging application connected to an electric generator [22-24] and are designed exclusively to supply the electric accessories of traditional vehicles, thus producing maximum output power within 6 kW. Given the lack of adequate references on the market, as therefore in the scientific

literature, as already explained, in the preliminary analysis the author considered two constant turbine thermomechanical efficiency $\eta_{T,tm}$, i.e. independent of the turbine speed and pressure ratio.

The efficiency values assumed are substantially higher than the efficiency of a common turbocharging turbine on account of the more favourable working condition already mentioned, which allows a design strategy aimed at maximizing the efficiency in steady operation, and also permits the control module of the electric generator to operate the turbine at its best efficiency speed ratio, regardless of the power produced.

The aim of this section is to provide a more precise and reliable estimation of the performances of the separated electric compound system by evaluating the turbine efficiency in accordance with its operating condition and thus getting rid of the simplifying assumption used in the previous section, in which the turbine efficiency was assumed to be constant. To this end, the turbine was analysed and designed by means of a simple yet effective mean-line based approach. In this section the author focused on radial turbines instead of a multi-stage axial turbine with the aim to reach a good compromise between efficiency and overall machine size [39-41].

As further step, it was established the most suitable kind of turbine for the task proposed; to this purpose, the author evaluated the turbine Mass Flow Parameter (MFP) values resulting for the preliminary analysis of the separated electric compound.

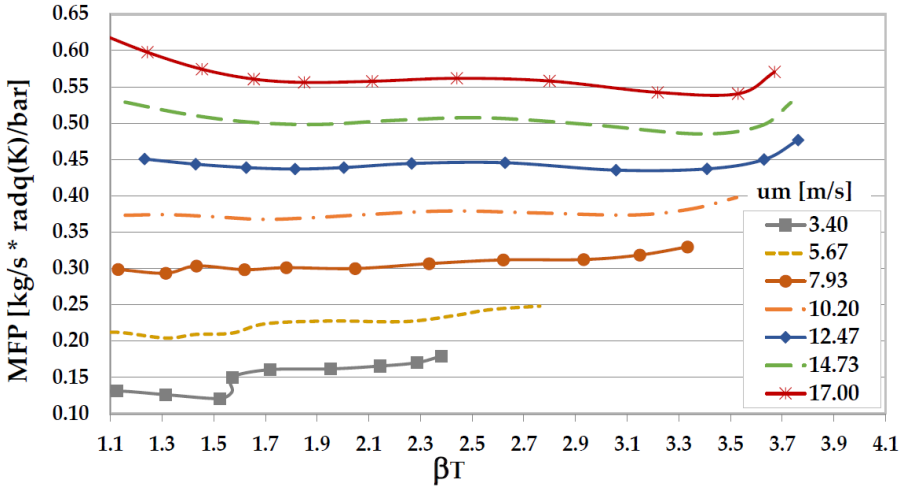

Figure 21. Operating points of the exhaust gas turbine of the separated electric compound engine studied in [4] (Mass Flow Parameter as function of turbine pressure ratio β_T)

As can be observed in **Figure 21**, where the turbine MFP values are shown as a function of the pressure ratio β_T, a single swallowing curve, typical of a fixed geometry turbine, cannot fit all the required operating points; as a consequence, a variable nozzle turbine was adopted, which allows multiple mass flow curves through the variation of the nozzle angle [42]. In the next part of this section the author first presents the mean-line prediction model algorithm used to evaluate the turbine performance for all the operating conditions of pressure ratio β_T, rotational speeds n (and consequent mass flow G_T). Successively, the design algorithm adopted to determine the main geometric dimensions of the turbine at the design operating condition is presented.

As a final step, the author presents the realistic performance of the separated electric compound engine evaluated by means of the 1-D turbine performance prediction model applied to the design geometry.

6.1.Radial turbine performance calculation model

As mentioned, the model adopted for the prediction of the turbine performance is based on mean-line analysis, according to which the flow is one-dimensional and is calculated at the mean radius of the turbomachinery stage, where the fluid properties are evaluated as reasonable average values across the full blade span. Mean-line analysis can provide good estimation of the geometry and flow parameters through a turbomachine. The author chose a one-dimensional approach because it represents the best solution in a preliminary design and performance analysis of a turbomachine. Successively, in a final design step, more detailed aerodynamic performance analysis can then be accomplished by CFD once appropriate turbine geometry and other parameters have been established through the mean-line analysis. **Figure 22** shows a schematic representation of the whole radial turbine, which includes the volute (from section 1 to section 2), the distributor nozzle (from section 2 to 3) and the rotor (from section 4 to 5).

As mentioned, the model adopted for the prediction of the turbine performance is based on mean-line analysis, according to which the flow is one-dimensional and is calculated at the mean radius of the turbomachinery stage, where the fluid properties are evaluated as reasonable average values across the full blade span.

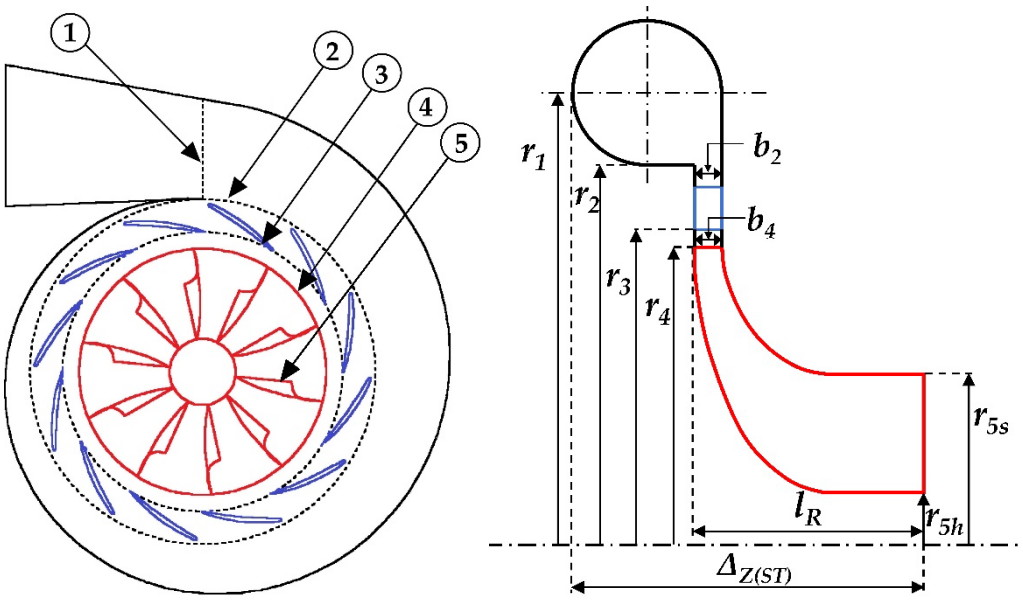

Figure 22. Schematic representation of turbine geometry, the numbers refer to the following main flow sections: 1) Volute inlet 2) Nozzle inlet; 3) Nozzle outlet; 4) Rotor inlet; 5) Rotor exit

In order to realistically assess the turbine efficiency, it was necessary to take into account the actual operating conditions; most of the time, in effect, the turbine does not operate at the design condition, since the pressure ratio and/or the rotational speed may be substantially different from the design values. For a given turbine geometry, the off-design operation will cause different mass flow rates and velocity triangles with respect to the design condition, and as a consequence, the turbine will exhibit a different overall performance, i.e. different output power and efficiency, with respect to the design point. With the aim to calculate the performances of the turbine for any possible operating condition, it was necessary to evaluate the energy losses connected to the flow inside the machine, by identifying the entropy generation mechanisms and quantifying their contribution in every phase of the fluid flow through the machine. The major contributions to the entropy generation are caused by incidence losses, passage losses (due to friction, secondary flow and flow separation), tip leakage flow and trailing edge losses, which occur in the internal blade passages in each of the

elements of the turbomachine (volute, nozzle and rotor). All these losses are conveniently quantified in terms of differences between the real static enthalpy at the exit of a stage, and that of the equivalent ideal isentropic process.

6.1.1. Analysis of the volute

The purpose of the volute is to distribute the flow around the periphery of the turbine providing uniform mass flow rate and uniform static pressure at the volute exit, thus ensuring the proper exploitation of each rotor blade passage and avoiding unsteady radial loading of the rotating system.

The static temperature at volute inlet T_1 can be calculated from the application of the first law of thermodynamics to a perfect gas:

$$T_1 = T_{T1} - \frac{c_1^{\,2}}{2 \cdot c_p\left(\overline{T_{T1-1}}\right)} \tag{67}$$

Being c_1 the absolute gas velocity at the volute inlet section 1, and $c_p(\overline{T_{T1-1}})$ the specific heat at constant pressure evaluated at the average temperature $\overline{T_{T1-1}} = (T_{T1}+T_1)/2$ through the use of the Shomate equation and the coefficients available on the NIST Chemistry WebBook [33]. It is worth noting that equation (67) implies an iterative calculation, since $c_p(\overline{T_{T1-1}})$ requires the value of T_1 which is the output of the equation. As starting value it was assumed $c_p(\overline{T_{T1-1}}) = c_p(\overline{T_{T1}})$. Analogous iterations have been carried out for similar evaluations performed in this thesis.

It is worth noting that equation (67) implies an iterative calculation, since $c_p(\overline{T_{T1-1}})$ requires the value of T_1 which is the output of the equation. As starting value it was assumed $c_p(\overline{T_{T1-1}}) = c_p(\overline{T_{T1}})$. Analogous iterations have been carried out for similar evaluations performed in this work.

Since for any given turbine pressure ratio $\beta_T = P_{T1}/P_5$ and rotor speed n_T, the pressure levels in the sections 1, 2, 3 and 4 (i.e. P_1, P_2, P_3, and P_4) are not known a priori, all the absolute velocities in the same sections are initially unknown; for this reason, each calculation procedure was started assuming an initial first attempt value of 100 m/s for each of the unknown absolute velocities (c_1, c_2, c_3 and c_4); the values of these velocities were then updated by successive iterations performed with the aim to obtain the mass-flow convergence on all the turbine sections. It is worth to point out that the turbine pressure ratio β_T was defined as:

$$\beta_T = \frac{p_S - \Delta p_1}{p_0 + \Delta p_2} = \frac{P_{T1}}{P_5} \tag{68}$$

Being p_s the in-cylinder gas pressure during exhaust stroke, Δp_1 the pressure drop up the turbine inlet, and Δp_2 the pressure drop between turbine outlet and ambient pressure p_0 (see chapter 5 for more details).

Assuming an isentropic expansion from the total condition upstream of the turbine (gas pressure P_{T1} and temperature T_{T1}), to the static condition, it was possible to calculate the static pressure at the volute inlet as:

$$P_1 = P_{T1} \cdot \left(\frac{T_1}{T_{T1}} \right)^{\frac{k\left(\overline{T_{T1-1}}\right)}{1-k\left(\overline{T_{T1-1}}\right)}} \tag{69}$$

being $k(\overline{T_{T1-1}})$ the mean isentropic coefficient evaluated at the average temperature $\overline{T_{T1-1}}$:

$$k\left(\overline{T_{T1-1}}\right) = \frac{c_p\left(\overline{T_{T1-1}}\right)}{c_v\left(\overline{T_{T1-1}}\right)} = \frac{c_p\left(\overline{T_{T1-1}}\right)}{c_p\left(\overline{T_{T1-1}}\right) - R'} \tag{70}$$

where, according to Meyer's relation, the specific gas constant R' is the difference between the constant pressure and the constant volume specific heats c_p and c_v. It is worth pointing out that, in the case of the isentropic

transformation, the average temperature $\overline{T_{T1-1,is}}$= (T_{T1}+$T_{1,is}$)/2 should be considered; however, being the difference between T_1 and $T_{1,is}$ not relevant, it results that the difference between $k(\overline{T_{T1-1,is}})$ and $k(\overline{T_{T1-1}})$ is negligible (less than 0.01%), as well as the difference between $c_p(\overline{T_{T1-1,is}})$ and $c_p(\overline{T_{T1-1}})$; the same conclusion is obtained considering the turbine nozzle and the rotor, where the enthalpy drops are higher; according to this observation the author adopted the approximation to use the average temperature of the real evolution in place of the average temperature of the isentropic evolution when calculating the thermochemical properties of the gas, i.e. the specific heat at constant pressure and the isentropic coefficient.

The static density of the gas at the volute inlet ρ_1 was then calculated by means of the perfect gas law as function of P_1 and T_1 as:

$$\rho_1 = \frac{P_1}{R' \cdot T_1} \tag{71}$$

And the mass-flow rate at the volute inlet G_1 resulted as:

$$G_1 = \rho_1 \cdot c_1 \cdot A_1 \tag{72}$$

Where A_1 is the inlet volute area. The absolute gas velocity c_1 was then corrected with the aim to reduce the difference between the mass-flow at the volute inlet G_1 and outlet G_2 (whose calculation is showed further on), which is considered a mass-flow error:

$$c_{1,new} = c_{1,old} - (G_1 - G_2) \cdot f_C \tag{73}$$

being f_C the factor adopted for the absolute velocities iterative corrections; the same approach was followed for the correction of all the other absolute velocities, each one correlated to a proper mass-flow error; once all the mass-flow errors reach a negligible value (i.e. less than 0.1% of the mass-

flow), the solution is considered the final and the calculation procedure is stopped. The convergence on the mass-flow was reached acting on the absolute velocities (c_1, c_2, c_3 and c_4) rather than on the static pressure levels (P_1, P_2, P_3 and P_4) since the iterative correction performed on the static pressure values revealed some calculation instabilities.

As regards the flow within the turbine volute, the most common assumption usually made is to consider a free vortex evolution; a variety of extensions to the free vortex model, however, have been proposed in the scientific literature to reproduce the real flow conditions, which are affected by friction, secondary flows, and mixing of the mainstream flow with outer fluid in the proximity of the outlet section. Loss correlations and coefficients may be used to account for deviations from the ideal evolution. Kastner and Bhinder in [43] represented the volute loss as a friction loss using conventional pipe-flow correlations. As proposed by Baines in [42], this loss item can be considered as the difference between the actual static enthalpy at exit from the volute and that of the equivalent isentropic process:

$$\Delta h_{vol} = h_2 - h_{2,is} = \frac{1}{2} C_f \cdot \left(L_{hyd,vol} \Big/ D_{hyd,vol} \right) \cdot \bar{c}^2 \tag{74}$$

where $\bar{c} = (c_1 + c_2)/2$ is the mean passage velocity (average value between inlet and outlet velocity), $L_{hyd,vol}$ and $D_{hyd,vol}$ are the hydraulic length and diameter of the volute respectively, while the coefficient of friction C_f is defined as:

$$C_f = 0.054 \cdot \left(\frac{\bar{c} \cdot D_{hyd,vol}}{\bar{\nu}} \right)^{-0.25} \tag{75}$$

being $\bar{\nu} = \left[\nu_{(T1)} + \nu_{(T2)} \right]/2$ the mean kinematic viscosity of the fluid between inlet and outlet of the volute. The free vortex evolution can be hence

modified to include the effects of shear stresses due to friction by means of the following relation:

$$\frac{c_1}{c_{2u}} = \frac{r_1}{r_2} + \frac{2 \cdot \pi \cdot C_f \cdot r_2 \cdot c_{2u}}{G} r_1 \cdot \left(r_1 - r_2 \right) \tag{76}$$

Which gives as result the tangential component of the absolute velocity at volute outlet c_{2u}. This correlation is based on an analysis performed by Stanitz [44] on the flow in the vaneless diffuser of a compressor, but being an analysis based on fundamental control volume, it could be adapted to the flows in the turbine volutes. It goes without saying that the volute loss produces a reduction in the real fluid velocity at volute outlet with respect to the ideal evolution, as shown by the simple application of the first law of thermodynamics between volute inlet and outlet sections:

$$c_2 = \sqrt{c_1^{\,2} + 2 \cdot \left(\Delta H_{is(vol)} - \Delta h_{vol} \right)} = \sqrt{c_1^{\,2} + 2 \cdot \Delta H_{re(vol)}} \tag{77}$$

being $\Delta H_{is(vol)}$ and $\Delta H_{re(vol)}$ the isentropic and the real enthalpy drop in the volute respectively. As already mentioned, however, being initially unknown the pressure level at the volute outlet P_2, the isentropic enthalpy drop is initially unknown as well as the absolute velocity c_2 which is required for the calculation of the volute loss. The calculation procedure is hence based on successive iterative approximation; the initial value of 100 m/s was assumed for the absolute velocity at nozzle inlet c_2, which, in turn, allowed to evaluate the gas temperature at the volute outlet T_2 by the application of the first law of thermodynamics:

$$T_2 = T_1 - \frac{c_2^{\,2} - c_1^{\,2}}{2 \cdot c_p \left(\overline{T_{1-2}} \right)} \tag{78}$$

and the consequent real enthalpy drop in the volute $\Delta H_{re(vol)}$:

$$\Delta H_{re(vol)} = h_1 - h_2 = c_p\left(\overline{T_{1-2}}\right)\cdot(T_1 - T_2) \tag{79}$$

Considering the isentropic transformation, the static pressure at nozzle outlet was evaluated as:

$$P_2 = P_1 \cdot \left(1 - \frac{\Delta H_{is(vol)}}{T_1 \cdot c_p\left(\overline{T_{1-2}}\right)}\right)^{\frac{k\left(\overline{T_{1-2}}\right)}{k\left(\overline{T_{1-2}}\right)-1}} \tag{80}$$

being the isentropic enthalpy drop obtained as the sum of the real enthalpy drop (equation (79)) and the volute loss (equation (74)):

$$\Delta H_{is(vol)} = \Delta H_{re(vol)} + \Delta h_{vol} \tag{81}$$

As already discussed, the mean constant pressure specific heat $c_p(\overline{T_{1-2}})$ and the mean isentropic coefficient $k(\overline{T_{1-2}})$ were both evaluated at the average temperature $\overline{T_{1-2}}=(T_1+T_2)/2$. As done for the volute inlet (see eq.(71)), the fluid density at the volute outlet section ρ_2 was evaluated though the application of the perfect gas law as function of the pressure P_2 and the temperature T_2. The mass flow through the volute outlet section G_2 could be hence calculated as:

$$G_2 = \rho_2 \cdot c_{2m} \cdot A_2 \tag{82}$$

where the meridional component of absolute velocity at volute outlet c_{2m} was evaluated as function of the tangential component of the absolute velocity c_{2u} obtained by eq. (76):

$$c_{2m} = \sqrt{{c_2}^2 - {c_{2u}}^2} \tag{83}$$

Again, the absolute velocity at volute outlet c_2 was corrected with the aim to reduce the mass-flow error between volute outlet and nozzle outlet, i.e. (G_2-G_3):

$$c_{2,new} = c_{2,old} - (G_2 - G_3) \cdot f_C \tag{84}$$

Once updated the value of the absolute velocity at volute outlet c_2, the entire calculation procedure from equation (74) to equation (84) is repeated until the mass-flow error (G_2-G_3) becomes negligible (i.e. less than 0.1% of G_2).

6.1.2. Analysis of the nozzle

The nozzle consists of an annular ring of vanes which set the angle of approach of the working fluid to the rotor and it works in conjunction with the volute to accelerate the fluid. As in the case of the volute, nozzle losses ultimately lead to a reduction of outlet velocity compared to the ideal evolution. It is possible to distinguish nozzle passage losses and nozzle incidence losses. The nozzle passage loss is mainly caused by the action of friction forces between the flow and the nozzle blade's solid surface [45], and it was determined by the following equation:

$$\Delta h_{p(nozzle)} = h_3 - h_{3,is} = 4 \cdot f \cdot \frac{L_{hyd,nozzle}}{D_{hyd,nozzle}} \cdot \left(\bar{c}\right)^2 \tag{85}$$

where $L_{hyd,nozzle}$ and $D_{hyd,nozzle}$ are the hydraulic length and diameter of the nozzle respectively, $\bar{c} = (c_2 + c_3)/2$ is the mean passage velocity (average value between nozzle inlet and outlet), while f is the friction factor evaluated as:

$$f = 8\left\{\left(\frac{8}{\overline{\mathrm{Re}}}\right)^{12} + \left\{\left[2.457 \ln\left(\frac{1}{\left(\frac{7}{\overline{\mathrm{Re}}}\right)^{0.9} + 0.27 \cdot RR}\right)\right]^{16} + \left(\frac{37530}{\overline{\mathrm{Re}}}\right)^{16}\right\}^{-1.5}\right\}^{\frac{1}{12}} \tag{86}$$

being $\overline{Re}$ the average Reynolds number between nozzle inlet and outlet, while RR represents the wall relative roughness, for which the value of 0.0002 [m] is suggested by Suhrmann et al [46].

The nozzle incidence loss, on the other hand, arises whenever there is a difference between the fluid-dynamic nozzle inlet angle $\alpha_{2,f}$ and the nozzle geometric inlet angle $\alpha_{2,g}$; a simple yet effective correlation for the calculation of the nozzle incidence loss is:

$$\Delta h_{i(nozzle)} = \frac{1}{2} c_2^{\,2} \cdot sin^2 \left(\alpha_{2,f} - \alpha_{2,g} \right) \tag{87}$$

As already observed in the case of the volute, the absolute velocity at nozzle outlet c_3 is related to the isentropic enthalpy drop in the nozzle $\Delta H_{is(nozzle)}$, to the real enthalpy drop $\Delta H_{re(nozzle)}$ and to the losses $\Delta h_{p(nozzle)}$ and $\Delta h_{i(nozzle)}$ by the first law of thermodynamics applied between inlet and outlet sections of the nozzle (i.e. sections 2 and 3 of **Figure 22**):

$$c_3 = \sqrt{c_2^{\,2} + 2 \cdot \left(\Delta H_{is(nozzle)} - \Delta h_{p(nozzle)} - \Delta h_{i(nozzle)} \right)} = \sqrt{c_2^{\,2} + 2 \cdot \Delta H_{re(nozzle)}} \tag{88}$$

Also in this case, being initially unknown the static pressure at the nozzle exit P_3, as well as the isentropic enthalpy drop, the absolute velocity at nozzle outlet c_3 could not be evaluated through equation (88); the calculation procedure was based on successive iterative approximation also in this case, adopting a first attempt value of 100 m/s also for the absolute velocity c_3. The static temperature at nozzle outlet T_3 was hence calculated as:

$$T_3 = T_2 - \frac{c_3^{\,2} - c_2^{\,2}}{2 \cdot c_p \left(\overline{T_{2-3}} \right)} \tag{89}$$

and the related real enthalpy drop in the nozzle:

$$\Delta H_{re(nozzle)} = c_p \left(\overline{T_{2-3}} \right) \cdot (T_3 - T_2) \tag{90}$$

The static pressure P_3 at nozzle outlet was obtained through the isentropic transformation:

$$P_3 = P_2 \cdot \left(1 - \frac{\Delta H_{is(nozzle)}}{T_2 \cdot c_p\left(\overline{T_{2-3}}\right)}\right)^{\frac{k\left(\overline{T_{2-3}}\right)}{k\left(\overline{T_{2-3}}\right)-1}} \tag{91}$$

where the isentropic enthalpy drop $\Delta H_{is(nozzle)}$ was obtained from the real enthalpy drop and the losses in the nozzle:

$$\Delta H_{is(nozzle)} = \Delta H_{re(nozzle)} + \Delta h_{nozzle} = \Delta H_{re(nozzle)} + \Delta h_{p(nozzle)} + \Delta h_{i(nozzle)} \tag{92}$$

The static density of the fluid at nozzle outlet ρ_3 was evaluated by the application of the perfect gas law (see eq.(71)) as function of the temperature T_3 and pressure P_3, thus allowing to evaluate the mass-flow at the nozzle exit G_3:

$$G_3 = \rho_3 \cdot c_{3m} \cdot A_3 \tag{93}$$

Being c_{3m} the meridional component of the gas velocity in the nozzle outlet section

$$c_{3m} = c_3 \cdot \sin(\alpha_{3,g}) \tag{94}$$

and A_3 the flow section normal to c_{3m}. As already done for the volute, the absolute velocity c_3 was corrected on the basis of the mass-flow error:

$$c_{3,new} = c_{3,old} - (G_3 - G_4) \cdot f_C \tag{95}$$

and hence the calculation procedure from equation (85) to equation (95) was repeated until the mass-flow convergence was reached.

6.1.3. Analysis of the nozzle-rotor interspace

In a variable geometry turbine, the swallowing capacity is controlled though the variation of the nozzle passage section which is obtained by the rotation of the nozzle blades; the lower mass flows can be obtained adopting small opening angles; increasing the opening angles allows the turbine to swallow higher mass flows. For this reason, a radial gap Δr

between the nozzle exit radius r_3 and the rotor inlet radius r_4 is necessary (see Figure 23), just to allow the nozzle blades rotation without causing any impact on the rotor.

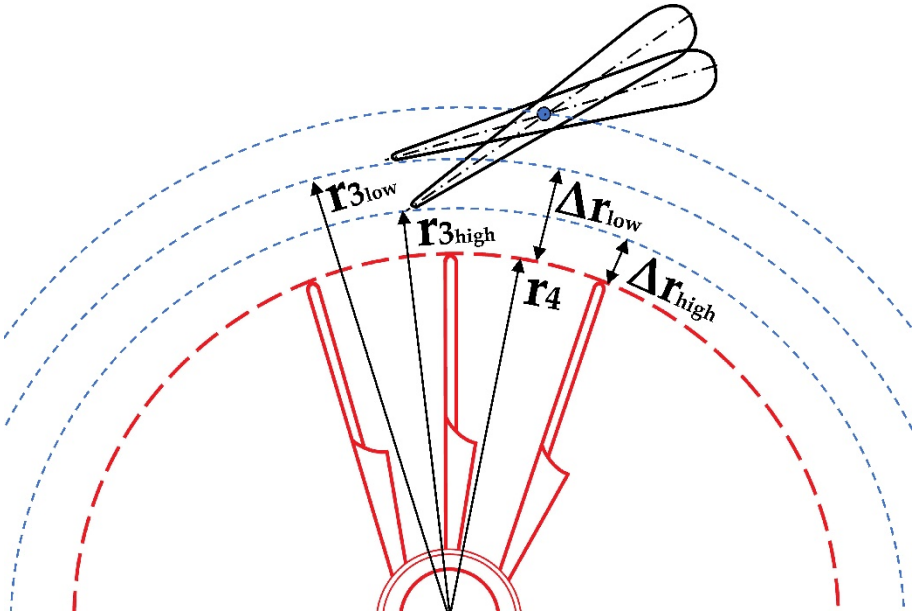

Figure 23: Radial gap between nozzle outlet section (radius r_3) and rotor inlet section (radius r_4)

As can also be observed in Figure 23, the radial gap increases when the nozzle blades reduce the opening angle, i.e. when the mass flow is reduced. This radial gap generates a limited interspace between nozzle outlet (section 3) and rotor inlet (section 4), where it is plausible to assume an ideal free vortex evolution, according to which:

$$c_{4u} = c_{3u} \frac{r_3}{r_4} \tag{96}$$

being the absolute velocity of the fluid at the rotor inlet c_4 related to the isentropic enthalpy drop in the radial gap $\Delta H_{is(gap)}$:

$$c_4 = \sqrt{c_3^2 + 2 \cdot \Delta H_{is(gap)}} \tag{97}$$

As in the previous cases, being initially unknown the static pressure at the rotor inlet P_4, and hence the isentropic enthalpy drop in the radial gap, the absolute velocity c_4 could not be evaluated through equation (97); an

iterative calculation procedure was employed also in this case, adopting a first attempt value of 100 m/s also for the absolute velocity c_4. The static temperature at the rotor inlet T_4 was then calculated as:

$$T_4 = T_3 - \frac{{c_4}^2 - {c_3}^2}{2 \cdot c_p\left(\overline{T_{3-4}}\right)} \tag{98}$$

The static pressure P_4 could be instead obtained through the isentropic evolution from the nozzle exit (condition 3) to rotor inlet (condition 4):

$$P_4 = P_3 \cdot \left(\frac{T_4}{T_3}\right)^{\frac{k\left(\overline{T_{3-4}}\right)}{k\left(\overline{T_{3-4}}\right)-1}} \tag{99}$$

The density of the fluid at the rotor inlet could be hence calculated by the application of the perfect gas law:

$$\rho_4 = \frac{P_4}{R' \cdot T_4} \tag{100}$$

Which, in turn, allowed to calculate the mass flow at the rotor inlet G_4:

$$G_4 = \rho_4 \cdot c_{4m} \cdot A_4 \tag{101}$$

Being A_4 the flow passage section at the rotor inlet, while the meridional component of the absolute velocity c_{4m} was obtained as:

$$c_{4m} = \sqrt{{c_4}^2 - {c_{4u}}^2} \tag{102}$$

The absolute velocity c_4 at rotor inlet was hence corrected on the basis of the mass-flow error (G_4-G_5):

$$c_{4,new} = c_{4,old} - (G_4 - G_5) \cdot f_C \tag{103}$$

being G_5 the mass flow through the outlet section from the rotor. The calculation procedure from equation (96) to equation (103) was repeated until the mass-flow convergence was obtained.

6.1.4. Analysis of the rotor

The rotor is composed of a set of rotating blades which constitute a rotating ring of vanes, conceived to transform part of the fluid enthalpy and kinetic energy into mechanical work, which, in turn, is transferred to the rotating shaft. In a moving stage, multiple entropy generation mechanisms contribute to losses; the loss models mainly adopted in the scientific literature when dealing with the rotor of radial turbine are: rotor incidence loss, passage loss, clearance loss, disc windage loss and trailing edge loss [39–42].

The rotor incidence loss is related to the incidence of the fluid flows approaching the rotor passage; according to the mostly employed model, described by NASA in [47], the enthalpy variation Δh_{in} associated to the rotor incidence loss depends on the difference between the actual fluid-dynamic angle $\beta_{4,f}$ and the optimum incidence angle $\beta_{4,opt}$:

$$\Delta h_{in} = \frac{1}{2} w_4^{\,2} \sin^2\left(\beta_{4,f} - \beta_{4,opt}\right) \tag{104}$$

where w_4 represents the relative velocity of the fluid at the rotor inlet; it is worth mentioning that the optimum angle $\beta_{4,opt}$ is different from the geometric angle $\beta_{4,g}$ due to the motion that the rotor induces in the flow approaching the blades. The optimum angle $\beta_{4,opt}$ can be evaluated on the basis of the optimal tangential component of relative velocity $w_{4u,opt}$:

$$\beta_{4,ott} = \arctan\left(\frac{w_{4u,opt}}{c_{4m}}\right) \tag{105}$$

being:

$$w_{4u,opt} = c_{4u,opt} - u_4 \tag{106}$$

The optimal tangential component of the absolute velocity $c_{4u,opt}$ in turn can be evaluated as function of the peripheral linear velocity at the rotor inlet u_4 by means of an empirical equation proposed by Stanitz [48]:

$$c_{4u,opt} = u_4 \cdot \left(1 - \frac{1.98}{N_R}\right) \tag{107}$$

It results hence that the optimum angle $\beta_{4,opt}$ can be evaluated as:

$$\beta_{4,ott} = \arctan\left(-\frac{1.98 \cdot u_4}{N_R \cdot c_{4m}}\right) \tag{108}$$

The rotor passage loss is a generic term aimed to quantify the losses due to friction and secondary flow processes which occur in the passage through the rotor vanes; the two contributions are usually incorporated into a single enthalpy variation Δh_p since there is currently no way to isolate and measure their effects separately. In [42] the rotor passage losses are quantified through:

$$\Delta h_p = \frac{1}{2} K_p \left\{\left(\frac{L_{hyd,R}}{D_{hyd,R}}\right) + 0.68\left[1 - \left(\frac{r_5}{r_4}\right)^2\right]\frac{\cos\beta_5}{b_5/ch}\right\} \cdot \left(w_4^{\,2} + w_5^{\,2}\right) \tag{109}$$

where $L_{hyd,R}$ and $D_{hyd,R}$ are the hydraulic length and diameter of the rotor respectively, β_5 and b_5 are the geometric angle and the blade height at rotor outlet respectively, ch_{rot} is the rotor blade chord, which, according to [42] can be approximated as:

$$ch_{rot} = \frac{l_R}{\cos\left(\overline{\beta}\right)} \qquad \text{being} \qquad \tan\left(\overline{\beta}\right) = \frac{\tan\left(\beta_4\right) + \tan\left(\beta_5\right)}{2} \tag{110}$$

while K_p is a coefficient which, as suggested in [42], should be set to 0.11on the basis of some experimental data.

The clearance loss is the loss related to the fluid leakage from the rotor blade through the clearance gap between the rotor and its shroud. This loss seems to be affected to a greater extent by the radial clearance ε_r than by the axial clearance ε_x, and there appears to be a cross-coupling effect between the two

parameters. The author evaluated the enthalpy variation Δh_{cl} due to the rotor clearance loss as reported in [42]:

$$\Delta h_{cl} = u_4^{\,3} \frac{N_R}{8\pi}\left(K_x \varepsilon_x C_x + K_r \varepsilon_r C_r + K_{xr}\sqrt{\varepsilon_x \varepsilon_r C_x C_r}\right) \tag{111}$$

where N_R is the number of blades in the rotor, C_x and C_r are geometrical parameters, while the three coefficients K_x, K_r and K_{xr} should be set to 0.4, 0.75, and -0.3 respectively, as indicated in [42], in agreement with the previously described influences of ε_r and ε_x on rotor clearance loss.

The rotor disc windage loss is an external loss which expresses the power loss due to friction between the back face of the turbine disc and the fluid entrapped in the interspace between the rotor and its housing. According to [49], the enthalpy variation connected to the rotor windage loss Δh_w can be modelled as:

$$\Delta h_w = 0.25 \cdot K_f \cdot \frac{\overline{\rho} \cdot r_4^{\,2} \cdot u_4^{\,3}}{G_5} \tag{112}$$

where $\bar{\rho}$ is the average fluid density between inlet and outlet section of the rotor, G_5 is the turbine mass flow, while the coefficient K_f, as described in [50], depends on the Reynolds number evaluated at the rotor inlet (section 4 in) and on the turbine geometry:

$$K_f = 3.7\left(\frac{\varepsilon_b}{b_4}\right)^{0.1} \cdot \mathrm{Re}_4^{-0.5} \qquad \text{if} \qquad \mathrm{Re} < 3 \cdot 10^5 \tag{113}$$

$$K_f = 0.102\left(\frac{\varepsilon_b}{b_4}\right)^{0.1} \cdot \mathrm{Re}_4^{-0.2} \qquad \text{if} \qquad \mathrm{Re} > 3 \cdot 10^5 \tag{114}$$

Being ε_b the clearance between the back face of the turbine disc and its housing, while b_4 represents the blade height at rotor inlet.

Lastly, the trailing edge loss [51] is related to the sudden expansion of the fluid when it passes the trailing edge of the rotor. The expansion is due to the rapid flow section increment caused by the end of the rotor blades. It is worth pointing out that this loss becomes numerically relevant if the fluid

velocity is high, i.e. if the relative Mach number $M_{5,rel}$ (evaluated on the basis of the relative velocity at the rotor exit w_5) approaches 1. The model here adopted by the author calculates the enthalpy variation Δh_t related to the trailing edge loss as:

$$\Delta h_t = \frac{2}{k_{(T_5)} \cdot M_{5,rel}{}^2} \cdot \frac{\Delta P_{rel}}{P_5 \cdot \left(1 + \frac{w_5{}^2}{2 \cdot T_5 \cdot c_{p(T_5)}}\right)^{\left(\frac{k_{(T_5)}}{k_{(T_5)}-1}\right)}} \tag{115}$$

where P_5 and T_5 are the static pressure and temperature at the rotor exit (section 5), $M_{5,rel}$ is the already mentioned relative Mach number in section 5, k and c_p are the isentropic coefficient and the specific heat respectively (both evaluated at the temperature T_5), and ΔP_{rel} is the pressure drop caused by the sudden expansion, which, according to the model adopted [51], is assumed to be proportional to the relative kinetic energy at the rotor exit:

$$\Delta P_{rel} = \frac{\rho_5 \cdot w_5{}^2}{2} \left[\frac{N_R \cdot t}{\pi \cdot (r_{5s} - r_{5h}) \cdot \cos \beta_5} \right] \tag{116}$$

being r_{5s} and r_{5h} the shroud and hub radius at rotor exit respectively (see Figure 24), N_R the number of blades in the rotor and t the blade thickness. In the calculation performed on the rotor, the outlet static pressure P5 is known, being part of the boundary condition adopted (as resumed in Table 9); the isentropic enthalpy drop in the rotor can be hence calculated as:

$$\Delta H_{is(rotor)} = c_p\left(\overline{T_{4-5}}\right) \cdot T_4 \cdot \left[1 - \left(\frac{P_5}{P_4}\right)^{\frac{k\left(\overline{T_{4-5}}\right)-1}{k\left(\overline{T_{4-5}}\right)}}\right] \tag{117}$$

And hence the real enthalpy drop in the rotor $\Delta H_{re(rot)}$ can be obtained:

$$\Delta H_{re(rot)} = \Delta H_{is(rot)} - \Delta h_{rot} \tag{118}$$

being Δh_{rot} the sum of all the losses in the rotor (=Δh_{in}+ Δh_p+ Δh_{cl}+ Δh_w+ Δh_t) discussed from equation (104) to equation (116). The static gas temperature T_5 at rotor outlet is hence:

$$T_5 = T_4 - \frac{\Delta H_{re(rot)}}{c_p\left(\overline{T_{4-5}}\right)} \tag{119}$$

And the consequent fluid density ρ_5 obtained from the perfect gas law:

$$\rho_5 = \frac{P_5}{R' \cdot T_5} \tag{120}$$

The real enthalpy drop in the rotor also allows to calculate the relative velocity at rotor outlet w_5 through the application of the first law of thermodynamics between section 4 and section 5, in the relative reference system of the rotor:

$$w_5 = \sqrt{w_4^{\,2} + u_5^{\,2} - u_4^{\,2} + 2\Delta H_{re(rot)}} \tag{121}$$

Being w_4 the relative velocity at rotor inlet, u_4 and u_5 the peripheral linear velocity at the rotor inlet and outlet respectively. Once calculated, the value of w_5 is updated in equations (115) and (116), thus allowing an iterative solution. The meridional component of the velocity w_5 is:

$$w_{5m} = c_{5m} = w_5 \cdot \cos\left(\beta_{5,g}\right) \tag{122}$$

Where $\beta_{5,g}$ is the geometric blade angle at rotor outlet (see Figure 24). The mass-flow rate can be hence calculated:

$$G_5 = \rho_5 \cdot c_{5m} \cdot A_5 \tag{123}$$

which, as already mentioned, is employed in equation (103) for the iterative correction of the absolute velocity at the rotor inlet c_4. Since all the losses were expressed in terms of enthalpy variations, it is possible to evaluate the total-to-static isentropic efficiency of the stage as follows:

$$\eta_{t,s} = \frac{\Delta H_r}{\Delta H_{id}} = \frac{\Delta H_{id} - \Delta h_{rot} - \Delta h_{nozzle} - \Delta h_{vol} - \frac{1}{2}c_5^{\,2}}{\Delta H_{id}} \tag{124}$$

Where the ideal enthalpy drop ΔH_{id} is calculated considering an isentropic expansion from the inlet conditions (P_{T1}, T_{T1}) to the rotor exit static pressure P_5:

$$\Delta H_{id} = c_p\left(\overline{T_{T1-5,is}}\right)\cdot\left(T_{T1} - T_{5,is}\right) \tag{125}$$

Being

$$\overline{T_{T1-5,is}} = \frac{T_{T1} + T_{5,is}}{2} \tag{126}$$

$$T_{5,is} = T_{T1}\left(\frac{P_5}{P_{T1}}\right)^{\frac{k\left(\overline{T_{T1-5,is}}\right)-1}{k\left(\overline{T_{T1-5,is}}\right)}} \tag{127}$$

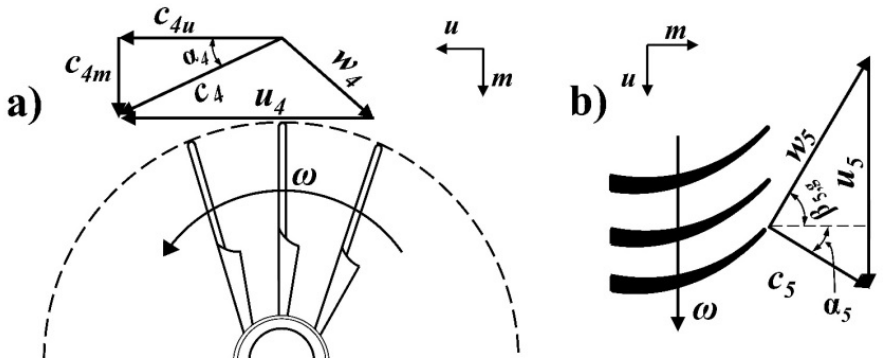

Figure 24: Velocity triangles a) rotor inlet; b) rotor outlet

6.1.5. Mechanical friction losses

A radial inflow turbine needs at least a journal bearing for shaft rotation and an axial thrust bearing that transfers the axial load of the turbine rotor to the machine frame [52]. The power dissipation in the journal bearing is primarily dependent on bearing geometry, oil viscosity, rotational speed and oil film thickness. Generally, the frictional power loss in journal bearings can be estimated through Petroff's equation [53] as:

$$POW_{J,B} = \frac{\pi}{4}\cdot\frac{\mu D^3 L\omega^2}{h} \tag{128}$$

where μ is the dynamic viscosity of the oil, ω is the rotational speed, L is the bearing length, D the bearing diameter and h the oil film thickness. The bearing diameter D was obtained by designing the shaft for infinite life according to the procedure described in [53], applying the Goodman criterion with a safety factor of 8. The material used for the shaft is a 40

NiCrMo 4430 steel, tempered at 540 C°, characterized by a yield strength of 1080 MPa and an ultimate tensile strength of 1170 MPa. The oil chosen for this application is Castrol 5W40 and its properties are evaluated at the working temperature of 90 C°. Finally, bearing length L was determined referring to available data for the L/D ratios applied in similar applications. According to Petroff's equation the bearing diameter is the largest influencing factor on power dissipation, followed by the rotational speed. However, decreasing the shaft diameter is not advisable because of the rotor dynamic issues.

The frictional power loss thrust bearings can be described by a modified Petroff's equation as follow:

$$POW_{T,B} = \frac{\pi\mu\omega^2}{2\varepsilon_{th}} \cdot \left(r_{ext,t}{}^4 - r_{in,t}{}^4 \right) \tag{129}$$

where $r_{in,t}$ denotes inner radius, determined by shaft diameter D, $r_{ext,t}$ is the outer radius calculated making reference to the $r_{ext,t}/\ r_{in,t}$ ratios used in similar cases, and ε_{th} is axial clearance, for which a value of 0.095 mm was assigned according to [52]. Petroff's equation reveals that the power dissipation is highly dependent on geometry, as for the journal bearing. Larger bearing contact surfaces result in higher power losses.

6.2. Design of the radial inflow turbine

In this chapter the author describes the procedure adopted to estimate the geometry and flow parameters of the turbomachine for the design condition. The design process is accomplished on the basis of predefined boundary conditions and operating parameters such as total inlet pressure P_{T1}, outlet static pressure P_5, total inlet temperature T_{T1}, mass flow rate G_T, and rotational speed of turbine rotor n_T.

6.2.1. Rotor design procedure

Once the turbine design parameters and its boundary conditions have been defined, the first calculation regards the discharge spouting velocity, i.e. the velocity associated to the isentropic enthalpy drop from total inlet pressure P_{T1} to the final exhaust pressure P_5:

$$C_{0s} = \sqrt{2 \cdot \Delta H_{id}} = \sqrt{2 \cdot c_p\left(\overline{T_{T1-5,is}}\right) \cdot T_{T1} \cdot \left(1 - \left(\frac{P_{5,is}}{P_{T1}}\right)^{\frac{k\left(\overline{T_{T1-5,is}}\right)-1}{k\left(\overline{T_{T1-5,is}}\right)}}\right)} \tag{130}$$

Where the average temperature is evaluated according to equations (126) and (127).

Another important parameter is the velocity ratio ν_s:

$$\nu_s = \frac{u_4}{C_{0s}} \qquad \Rightarrow \qquad u_4 = \nu_s \cdot C_{0s} \tag{131}$$

Since the value of ν_s is initially unknown, in the design procedure the first attempt value of 0.5 was assumed, which allows to determine u_4 and, in turn, the radius of the rotor inlet section.

$$r_4 = \frac{60 \cdot u_4}{2 \cdot \pi \cdot n_T} \tag{132}$$

In the nominal design condition, the outlet flow should be characterized by a zero swirl at the mean-line analysis, i.e. $c_{5u}=0$. As a result, the tangential component c_{4u} of the absolute velocity at rotor inlet could be computed by the application of the Euler equation, once the stage total-to-static efficiency $\eta_{t,s}$ is known:

$$c_{4u} = \frac{\Delta H_{id} \cdot \eta_{t,s}}{u_4} \tag{133}$$

It is obvious that, in the starting phase of the turbine design, the stage total-to-static efficiency $\eta_{t,s}$ is unknown (equation (124)); for this reason, in the design procedure a first attempt value was obtained by the empirical formula proposed by Aungier [40]:

$$\eta_{t,s} = 0.87 - 1.07 \cdot \left(n_s - 0.55\right)^2 - 0.5 \cdot \left(n_s - 0.55\right)^3 \tag{134}$$

where the specific speed n_s is:

$$n_s = \frac{2\pi \cdot n_T \cdot \sqrt{Q_5}}{60 \cdot \left(\Delta H_{id}\right)^{0.75}} \tag{135}$$

Being the volume flow at rotor exit Q_5 the ratio between the mass flow G_T and the rotor exit density ρ_5:

$$Q_5 = \frac{G_T}{\rho_5} \tag{136}$$

The fluid density at rotor outlet is calculated by means of the perfect gas law on the basis of the static pressure P_5 and of the rotor outlet temperature T_5, the latter being computed through the application of the first law of thermodynamics from section 1 to section 5 on the basis of the real enthalpy drop ΔH_r:

$$T_5 = T_{T1} - \frac{\Delta H_r}{c_p\left(\overline{T_{T1-5}}\right)} = T_{T1} - \frac{\Delta H_{id} \cdot \eta_{t,s}}{c_p\left(\overline{T_{T1-5}}\right)} \tag{137}$$

As is usually adopted for radial inward turbine, the inlet blade angle α_{4g} was considered to be 90° in this application. As instead regards the inlet absolute flow angle α_4, in the best efficiency condition, it is substantially a function of the specific speed n_s, as shown in [54]. The data reported in [54] have been employed to obtain a numerical correlation [40] used to obtain a first attempt value of the inlet absolute flow angle α_4, which is successively updated on the basis of the results:

$$\alpha_4 = 10.8 + 14.2 \cdot n_s^{\,2} \tag{138}$$

Equations (133) and (138) allow determining the meridional component of the fluid velocity at rotor inlet:

$$c_{4m} = \frac{c_{4u}}{\tan \alpha_4} = w_{4m} \tag{139}$$

The tangential component of relative velocity at rotor inlet is hence:

$$w_{4u} = c_{4u} - u_4 \tag{140}$$

Which allows the determination of the fluid-dynamic relative flow angle:

$$\beta_{4f} = \arctan\left(\frac{w_{4m}}{w_{4u}}\right) \tag{141}$$

Once the absolute velocity at rotor inlet is calculated ($c_4 = \sqrt{{c_{4u}}^2 + {c_{4m}}^2}$), it is possible to obtain an approximate evaluation of the thermodynamic state of the fluid at the rotor inlet; as proposed in [40], assuming the losses upstream of the rotor to account for about 25% of the total losses and considering a constant density flow, the total pressure at rotor inlet P_{T4} can be estimated as:

$$P_{T4} = P_{T1} - \rho_{T1} \cdot \Delta H_{id} \frac{\left(1 - \eta_{t,s}\right)}{4} \tag{142}$$

and the static pressure at rotor inlet P_4 is hence:

$$P_4 \approx P_{T4} - \frac{1}{2} \cdot \rho_1 \cdot {c_4}^2 \tag{143}$$

The static enthalpy H_4 and the temperature T_4 at the rotor inlet may be evaluated as:

$$H_4 = H_{T1} - \frac{1}{2} {c_4}^2 \tag{144}$$

$$T_4 = T_{T1} - \frac{{c_4}^2}{2 \cdot c_p\left(\overline{T_{T1-4}}\right)} \tag{145}$$

The rotor inlet density ρ_4 can be then calculated through the application perfect gas law employing the pressure and temperature evaluated in equations (143) and (145) respectively; the rotor inlet blade height can be hence obtained by the mass flow rate equation:

$$b_4 = \frac{G_T}{2\pi r_4 \rho_4 c_{4m}} \tag{146}$$

While the hub radius at rotor outlet can be obtained as:

$$r_{h5} = 0.3 \cdot r_4 \tag{147}$$

being the proportionality constant 0.3 based on results optimization process, as also confirmed in [55]. Following a correlation proposed in [40], the meridional component of the absolute velocity at rotor outlet can be estimated as:

$$c_{5m} = c_{4m} \cdot \left[1 + 5 \cdot \left(b_4 / r_4\right)^2\right] \tag{148}$$

As already mentioned, the zero-swirl flow is assumed at the turbine exit (i.e. c_{5u}=0) in the nominal design condition, thus minimizing the exit kinetic energy losses at the rotor outlet; as a consequence, the absolute velocity at rotor outlet is equal to the meridional component, i.e. c_5=c_{5m}. The section area at the rotor outlet is then evaluated:

$$A_5 = \frac{G}{\rho_5 \cdot c_{5m}} \tag{149}$$

Where the static density at rotor outlet, as made previously, is calculated by means the perfect gas law employing the static pressure P_5 (imposed as boundary condition) and the temperature calculated in equation (137). The exit shroud radius r_{s5} is therefore:

$$r_{s5} = \sqrt{\frac{A_5}{\pi} + r_{h5}^2} \tag{150}$$

Then the rotor outlet mean radius is:

$$r_5 = \frac{r_{s5} + r_{h5}}{2} \tag{151}$$

The blade speed at rotor outlet mean radius is:

$$u_5 = \frac{2 \cdot \pi \cdot n_T}{60} \cdot r_5 \tag{152}$$

According to the zero-swirl flow at the rotor outlet, the meridional component of relative velocity coincides with the absolute velocity:

$$w_{5m} = c_{5m} = c_5 \tag{153}$$

And the tangential component of the relative velocity results:

$$w_{5u} = -u_5 \tag{154}$$

As a last step, the relative blade angle β_{5g} at rotor outlet (which in the design condition is equal to the flow angle β_{5f}) is determined:

$$\beta_{5g} = \beta_{5f} = \arctan\left(\frac{w_{5u}}{w_{5m}}\right) = \arctan\left(\frac{-u_5}{c_5}\right) \tag{155}$$

To complete the geometry design, the rotor axial length was defined through a further empirical correlation provided by [40]:

$$l_R = 1.5 \cdot \left(r_{s5} - r_{h5}\right) \tag{156}$$

Glassman in [56] introduced an empirical equation for the optimum number of radial inflow turbine rotor blades N_R:

$$N_R = \frac{\pi}{30}\left(110 - \alpha_4\right) \cdot \tan\left(\alpha_4\right) \tag{157}$$

whose result must be obviously rounded to an integer value.

After the first iteration, equations from (130) to (157) have been updated employing the stage total-to-static efficiency η_{ts} obtained from the turbine performance calculation model described in eq.(124) of the previous chapter. As already mentioned above, the value of ν_s of the first iteration was imposed equal to 0.5, but successively optimized to obtain the maximum efficiency of the stage.

6.2.2. Nozzle design procedure

The nozzle row sizing strategy requires that the nozzle passage width is constant and is identical to the rotor inlet passage width determined from the rotor sizing procedure:

$$b_3 = b_4 \tag{158}$$

The tangential velocity at the nozzle exit can be calculated by means the conservation of angular momentum between section 3 and 4:

$$c_{3u} = c_{4u} \cdot \frac{r_4}{r_3} \tag{159}$$

Where the r_3 represents the radius at nozzle exit. As already mentioned and shown in **Figure 23**, this radius depends on the position of the distributor blades, i.e. on the angle α_3: when the distributor blades are closed (i.e. for the minimum mass flow rates) the nozzle outlet flow angle α_3 is at its minimum value and hence the radial gap Δr reaches the maximum amplitude. When the mass flow rates are high, instead, the distributor blades are in "fully open" position, i.e. with the maximum angle α_3, to which corresponds the minimum radial gap Δr. Since in this section the author are giving the guidelines to define the turbine geometry for a

particular design operating condition, the radius at nozzle exit r_3 is given by:

$$r_3 = r_4 + \Delta r_D \tag{160}$$

Where Δr_D denotes the radial gap value at the design operating condition, which can be roughly obtained as:

$$\Delta r_D = 4 \cdot b_3 \cdot \cos \alpha_3 \tag{161}$$

It is worth pointing out that once defined the turbine geometry, the maximum swallowing capacity of the turbine must be verified according to the maximum allowed distributor blades angle α_3 which corresponds to a null radial gap: if it results that in this condition the turbine is not be able to swallow the required maximum mass flow rates, the design must be corrected with a higher value of Δr_D.

For the turbine design procedure, the absolute velocity at nozzle outlet c_3 was evaluated assuming the absolute flow angle at nozzle outlet α_3 equal to the rotor inlet absolute flow angle α_4 (i.e. considering a null radial gap):

$$c_3 = \frac{c_{3u}}{\cos(90 - \alpha_3)} = \frac{c_{3u}}{\cos(90 - \alpha_4)} \tag{162}$$

Then the meridional component of absolute velocity is:

$$c_{3m} = c_3 \cdot \sin(90 - \alpha_3) \tag{163}$$

The static enthalpy H_3 and the temperature of the gas T_3 at nozzle outlet were computed as:

$$H_3 = H_{T1} - \frac{1}{2} {c_3}^2 \tag{164}$$

$$T_3 = T_4 + \frac{\left({c_4}^2 - {c_3}^2\right)}{2 \cdot c_p\left(\overline{T_{3-4}}\right)} \tag{165}$$

Since the flow conditions at nozzle inlet are initially unknown, and aiming to induce minimal incidence losses, at the design condition the inlet flow angle is assumed to be equal to the inlet blade angle (i.e. $\alpha_{2f} = \alpha_{2g}$); moreover, it is also assumed a constant density flow between section 2 and 3, which hence allows calculating the meridional component of the absolute velocity at distributor inlet:

$$c_{2m} \cong c_{3m} \cdot \frac{r_3}{r_2} \tag{166}$$

Aungier in [40] suggested that the ratio of nozzle inlet to outlet radius r_2/r_3 lies between 1.1 and 1.7. In this work the author adopted a value of 1.3 in order to obtain a good compromise between performance and overall size of the nozzle. Assuming a symmetrical nozzle blade profile, simple geometric considerations based on the triangle generated by the nozzle geometry (shown in Figure 25), allowed to calculate the nozzle inlet blade angle $\alpha_{2,g}$ as function of the exit blade angle $\alpha_{3,g}$:

$$\alpha_{2,g} = \frac{\pi}{2} - \arcsin\left[\frac{r_3}{r_2} \cdot \sin\left(\frac{\pi}{2} + \alpha_{3,g}\right)\right] \tag{167}$$

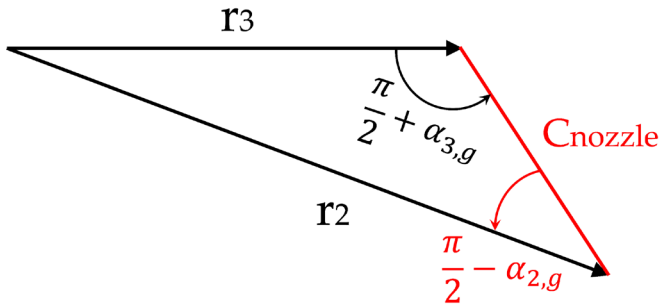

Figure 25: Geometric representation of the nozzle

The application of the Carnot's theorem at the triangle of **Figure 25** also allowed to evaluate the length of the nozzle blade chord C_{nozzle}:

$$r_2^2 = r_3^2 + C_{nozzle}^2 - 2 \cdot r_3 \cdot C_{nozzle} \cdot \cos\left(\frac{\pi}{2} + \alpha_{3,g}\right) \tag{168}$$

$$\Rightarrow C_{nozzle} = 2 \cdot r_3 \cdot \cos\left(\frac{\pi}{2} + \alpha_{3,g}\right) + \sqrt{\left(2 \cdot r_3 \cdot \cos\left(\frac{\pi}{2} + \alpha_{3,g}\right)\right)^2 - 4 \cdot \left(r_3^2 - r_2^2\right)} \tag{169}$$

Once determined the distributor inlet flow angle α_2, the tangential component of absolute velocity at nozzle inlet can be calculated as:

$$c_{2u} = \frac{c_{2m}}{\tan \alpha_2} \tag{170}$$

The absolute velocity at nozzle inlet is hence consequently calculated as:

$$c_2 = \sqrt{{c_{2u}}^2 + {c_{2m}}^2} \tag{171}$$

Since the velocity triangle at nozzle inlet just calculated is based on the approximate value of c_{2m} obtained from equation (166), an iterative correction process based on the conservation of mass flow-rate (G_2=G_3) is necessary to obtain a more accurate value of c_{2m}. For this purpose, the static temperature and pressure at nozzle inlet are evaluated as:

$$T_2 = T_3 + \frac{\left({c_3}^2 - {c_2}^2\right)}{2 \cdot c_p\left(\overline{T_{2-3}}\right)} \tag{172}$$

$$P_2 = P_3 \cdot \left(\frac{T_3}{T_2}\right)^{\frac{k\left(\overline{T_{2-3}}\right)}{1-k\left(\overline{T_{2-3}}\right)}} \tag{173}$$

Where, as made previously, both the isentropic coefficient and the specific heat are evaluated at the average temperature of the reference thermodynamic transformation (in this case $\overline{T_{2-3}}$). The static density ρ_2 of the working fluid at nozzle inlet can hence be obtained from the perfect gas law as a function of the temperature T_2 and pressure P_2. At this point the meridional component of the absolute velocity at distributor inlet is given by:

$$c_{2m} = \frac{G_2}{2\pi r_2 \rho_2 b_2} = \frac{G_3}{2\pi r_2 \rho_2 b_2} \tag{174}$$

Eq.(174) represents the updated value of the meridional component of absolute velocity at nozzle inlet, evaluated on the basis of the mass flow-rate swallowing capacity of the section. This value is replaced to the approximate value obtained by equation (166) thus iteratively recalculating the loop from equation (167) to equation (174) until final convergence is achieved.

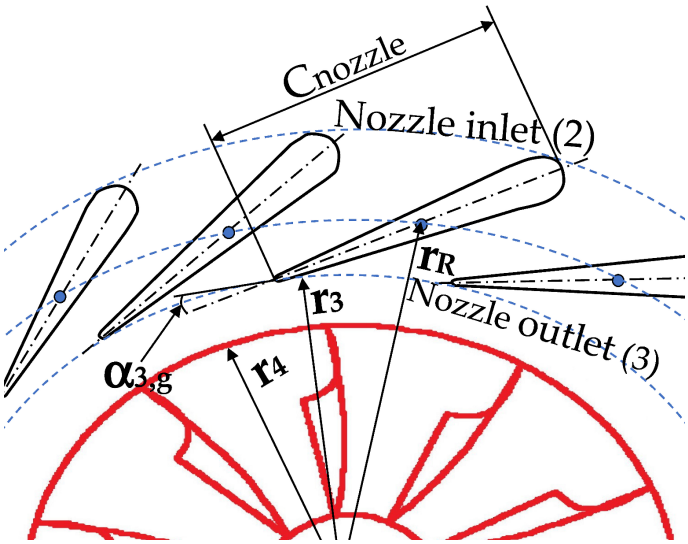

Figure 26: Schematic representation of nozzle geometry

6.2.3. Volute design procedure

The purpose of this section is to describe the analytical procedure adopted by the author for the design of the main geometric dimensions of the volute; as made in the previous sections, also in this case an iterative procedure was repeated until final value convergence was obtained. The volute inlet velocity (section 1 of **Figure 22**) is calculated by the conservation of the angular momentum:

$$c_1 = \frac{r_2}{r_1} \cdot c_{2u} \tag{175}$$

Since the value of the radial distance r_1 of the volute inlet section from the turbine axis is unknown in the initial phase of the design process, at first attempt it is assumed equal to r_2. This assumption allow to evaluate the static temperature at volute inlet:

$$T_1 = T_{T1} - \frac{c_1^{\,2}}{2 \cdot c_p\left(\overline{T_{1-2}}\right)} \tag{176}$$

Assuming an isentropic expansion from the total condition to the static condition, it is also possible to calculate the static pressure:

$$P_1 = P_{T1} \cdot \left(\frac{T_1}{T_{T1}}\right)^{\frac{k\left(\overline{T_{1-2}}\right)}{1-k\left(\overline{T_{1-2}}\right)}} \tag{177}$$

The density of the working fluid is then obtained through the application of the perfect gas law as function of P_1 and T_1. The area of the volute inlet section can hence be estimated:

$$A_1 = \frac{G}{\rho_1 \cdot c_1} \tag{178}$$

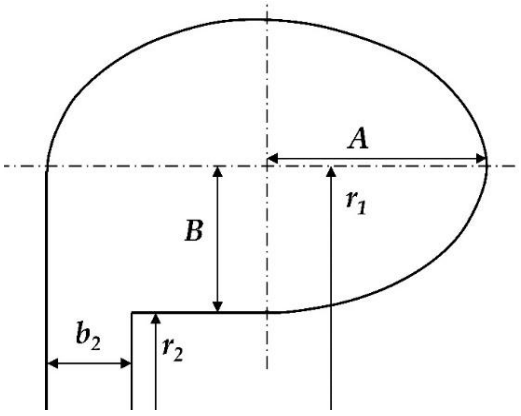

Figure 27: Inlet volute area geometry

As a general rule, the volute may have an elliptical section, as reported Figure 27; the axial semi-axis A is then:

$$A = \frac{A_1}{B \cdot \left(\frac{3}{4}\pi + 1 \right)} \tag{179}$$

while the radial distance r_1 is :

$$r_1 = r_2 + B \tag{180}$$

The radial semi-axis B is calculated on the basis of the volute aspect ratio A_R value:

$$A_R = \frac{A}{B} \qquad \Rightarrow \qquad B = \frac{A}{A_R} \tag{181}$$

In this work the author adopted an aspect ratio A_R=1, in accordance with the values of $0.75 \leq A_R \leq 1.5$ recommended in [40]. Once established the volute section aspect ratio, the calculation loop from equations (175) to (181) is iteratively repeated until the value of the radius r_1 reaches convergence. Therefore, after the volute design is completed, it is possible to estimate the total axial length of the stage as:

$$\Delta_{Z(ST)} = l_R + (2 \cdot A) - b_2 \tag{182}$$

6.3. Design calculation procedure

With the aim of explaining the whole calculation procedure adopted for the radial turbine design, Figure 28 shows a flowchart resuming the main steps followed by the author for the definition of the turbine geometry, here listed:

1) The input data (total pressure and temperature at turbine inlet, mass flow) are fed to the algorithm design block
2) The algorithm design block evaluates a first attempt value of the total-to-static efficiency of the turbine;

3) The total-to-static efficiency of the turbine is employed by the algorithm design block to define a turbine geometry;

4) The turbine geometry is fed to the performance prediction model for the realistic evaluation of all the energy losses, giving as final result the realistic total-to-static efficiency

5) The realistic total-to-static efficiency of the turbine is compared with the input efficiency employed in point 3):

   a. if their difference is higher than the convergence value the calculation re-starts from point 3) employing the new total-to-static efficiency for the new geometry evaluation.

   b. if their difference is lower or equal to the convergence value, the calculation is stopped and the last turbine geometry is adopted as the final result.

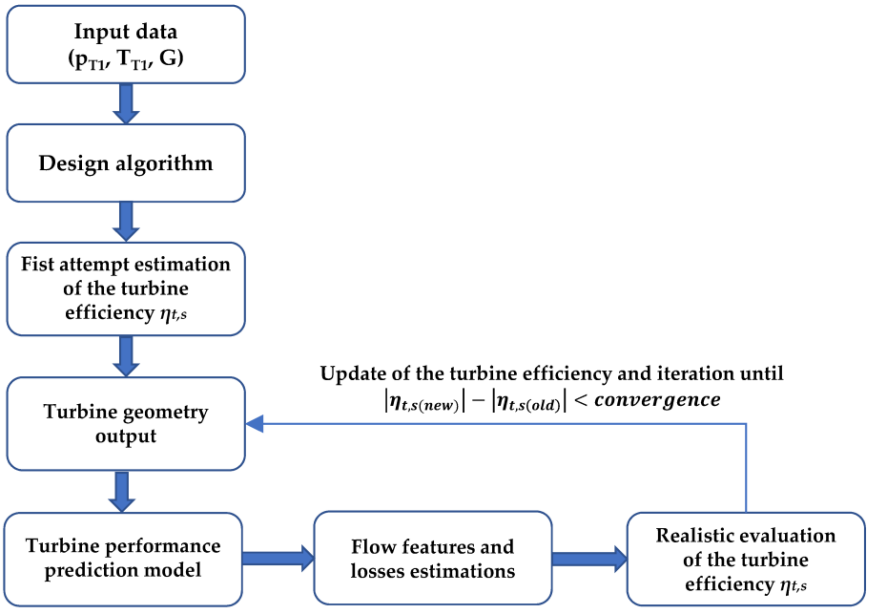

Figure 28: Flowchart of the design procedure adopted

6.4. Definition of the design operating condition and geometry output

The implementation of the design algorithm described in the chapter 6.2 of this work requires the definition of the turbine nominal operating condition. As already stated, the exhaust gas turbine of the turbo-generator group is designed to work on the CNG fuelled separated electric compound engine for hybrid vehicle the operating points of which are shown in **Figure 30**. As already explained in chapter 5 for each operating point of the compound engine, an optimum exhaust pressure exists which maximizes the overall brake thermal efficiency $\eta_{bTOT,COMP}$ of the system. The overall brake thermal efficiency $\eta_{bTOT,COMP}$ of the compound engine has been evaluated on the basis of the whole system output power as:

$$\eta_{bTOT,COMP} = \frac{POW_{TOT,COMP}}{G_b \cdot LHV} \tag{183}$$

Where $POW_{TOT,COMP}$ is the overall output power of the compound system. It is worth to point out that the overall output power of the separated electric compound system $POW_{TOT,COMP}$ is composed by the engine mechanical output power $POW_{ENG,COMP}$, with the addition of the mechanical output power of the exhaust gas turbine (here called recovery power POW_{REC}), and the reduction due to the power required by the motor-compressor POW_{COMPR}:

$$POW_{TOT,COMP} = POW_{ENG,COMP} + POW_{REC} - POW_{COMPR} \tag{184}$$

It is worth to point out that an efficiency 0.90 was considered for the supply-electric motor chain in the evaluation of the power drained by the compressor; as instead regards the turbine, the efficiencies of the electric generator and of the battery charging were not considered, coherently with

the approach followed for the main thermal engine, whose power split (part to the generator and part to the wheels) should depend on the particular mechanical transmission adopted, which is not defined in the evaluation here carried out. However, both the generator and the battery charging efficiency are almost the same also in the case of a hybrid propulsion system equipped with a traditional turbocharged engine: on account of this, the author fairly based their comparison on the mechanical output power produced. The aim of the present section is to provide a more precise and reliable estimation of the performances of the separated electric compound system by evaluating the turbine efficiency in accordance with its operating condition and thus getting rid of the simplifying assumption used in chapter 5, in which the turbine efficiency was assumed to be constant. The whole calculation procedure followed by the author to optimize the overall brake thermal efficiency of the compound engine is described in detail in chapter 5; the final result is shown in Figure 29, where the specific fuel consumption map of the GNC fuelled compound engine is reported as function of the mean piston speed Sp and overall brake mean effective pressure $BMEP_{TOT,COMP}$:

$$BMEP_{TOT,COMP} = \frac{60 \cdot \varepsilon_{ENG} \cdot POW_{TOT,COMP}}{V_{COMP} \cdot n_{COMP}} \tag{185}$$

where V_{COMP} and n_{COMP} denote the displacement and the speed of rotation of the thermal engine of the compound system, while ε_{ENG} is the number of engine rotation per cycle (2 in a four-stroke engine).

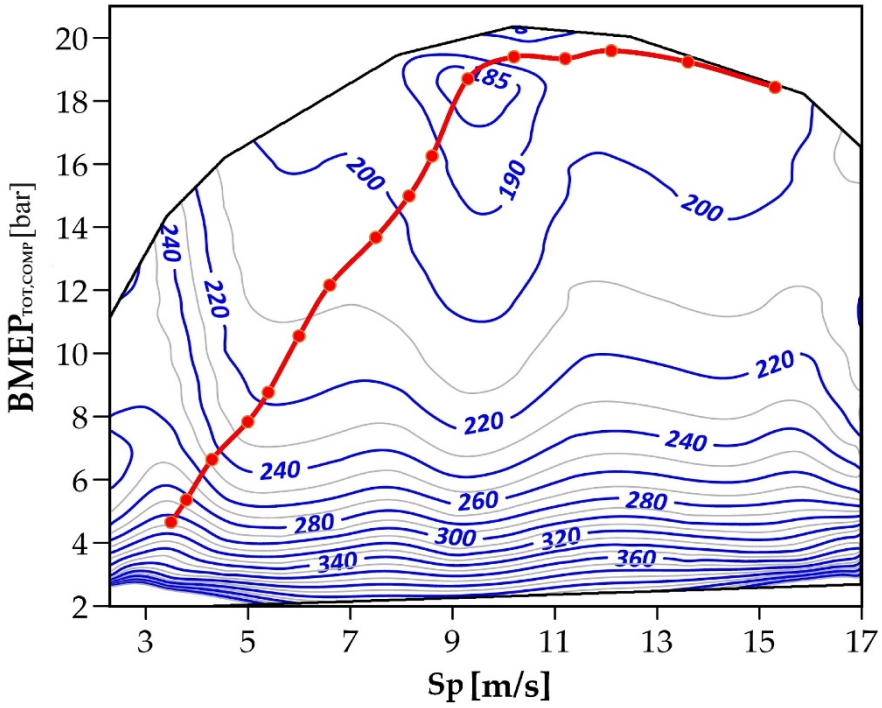

Figure 29: Brake specific fuel consumption (g/kWh) map of the preliminary separated electric compound engine $T_{EVO}/T_{IVC}=4$ and $\eta_{T,tm}=0.75$: the best efficiency curve is also reported

It is worth nothing, however, that in a hybrid propulsion system the thermal engine should work close to its best efficiency condition, so as to maximize the fuel economy of the vehicle; on account of this, the author also calculated the best efficiency curve of the compound system (red line in Figure 29), i.e. the curve connecting the operating conditions ($BMEP_{TOT,COMP}$ and Sp) which ensure, for each overall power request, the maximum overall efficiency.

Figure 30 shows the exhaust mass-flow rate G_T and turbine pressure ratio β_T evaluated for each point of the best efficiency curve of the compound system, as function of the overall output power.

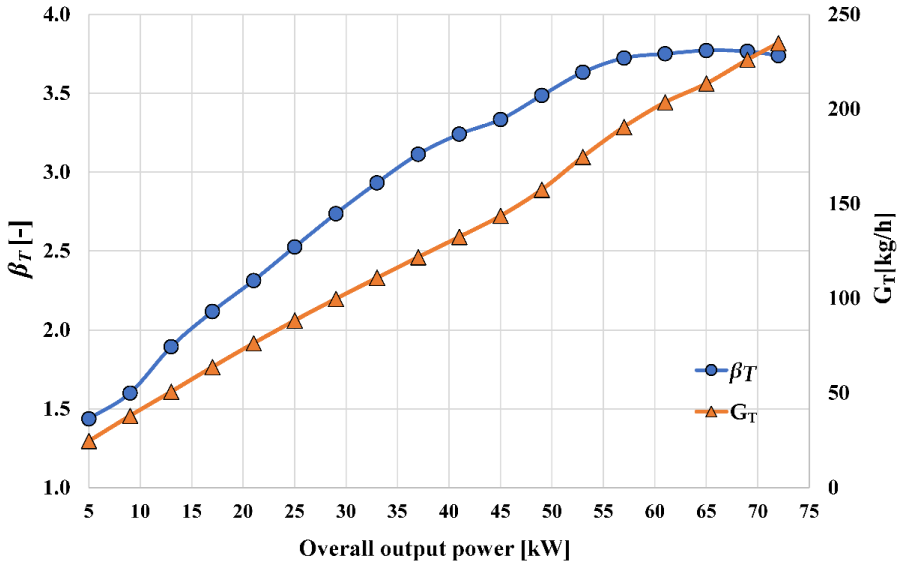

Figure 30: Operating points in terms of Mass Flow rate G_T and pressure ratio β_T of the exhaust gas turbine evaluated on the best efficiency curve of the separated electric compound engine studied

6.4.1. Turbine geometry and performance

The aim of the present work is to provide a more precise and reliable estimation of the performances of the separated electric compound system by evaluating the turbine efficiency in accordance with its operating condition and thus remove the simplifying assumption used in the preliminary studies, in which the turbine efficiency was assumed to be constant. After selecting the reference operating conditions of the turbine, the author proceeded with its design. With the aim to obtain the best performance for each operating point of the propulsion system, the geometry of the turbine was determined employing an optimized design procedure; this procedure consisted in the application of the design algorithm (described in paragraph 6.2 of this work) considering a particular set of design variable (i.e. the mass flow rate G_T, the total pressure upstream of the turbine P_{T1}, and the rotational speed of turbine rotor n_T), and in the successive evaluation of the turbine efficiency over the entire range of

operating conditions of Figure 29, carried out by means of the performance prediction model presented in paragraph 6.1.

Figure 31 shows some of the results obtained by implementation the optimized design procedure, which was repeated for many different sets of the three design variables; as shown in Figure 31, the best solution was obtained adopting the design values $\beta_T=2.19$, $n=130{,}000\ rpm$ and $G_T=150\ kg/h$: the resulting curve of the thermomechanical efficiency $\eta_{T,m}$ revealed the best over most part of the operating range, with an average value of 0.804.

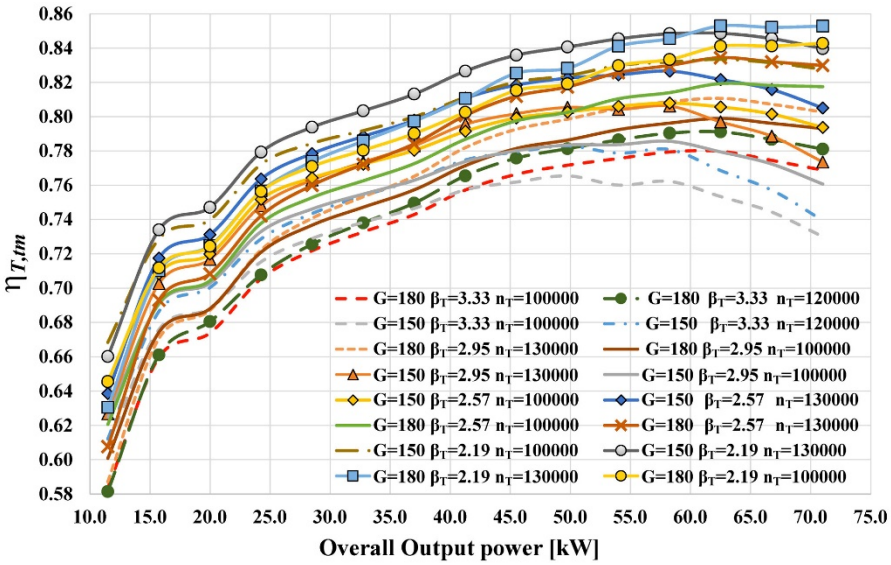

Figure 31: Turbine thermomechanical efficiency $\eta_{T,tm}$ as function of overall output of the separated electric compound system on its best efficiency curve for different turbine design operating conditions

Table 9 resumes all the design conditions adopted for the development of the radial turbine of this work, while Table 10 reports the resulting detailed turbine geometry obtained by the application of the design algorithm. Employing the turbine performance prediction model on the final geometry of the turbine (resumed in Table 10) allowed to trace the typical mass flow parameter (MFP) curves, reported in Figure 32, as function of the turbine pressure ratio (β_T) and for different values of the nozzle blade angle ($\alpha_{3,g}$): it

is clearly shown that, as desired, the variable nozzle turbine designed for the present work is fully able to swallow a wide range of mass-flow rates through the variation of the nozzle blade angle.

Table 9: Design parameters of the radial inflow exhaust gas turbine

Design condition of the radial inflow turbine	
Working fluid [-]	Air
Mass flow rate G_T [kg/h]	150
Inlet total pressure at turbine stage P_{T1} [bar]	2.3
Outlet static pressure at turbine stage P_5 [bar]	1.05
Inlet total temperature condition at turbine stage T_{T1} [K]	1070
Rotational speed of turbine stage n_T [rpm]	130000

Table 10 reports the geometry obtained by the application of the above-described design optimization procedure and the implementation of the design algorithm described in 6.2.

Table 10: Geometry design algorithm output

Radial inflow turbine geometry		
Inlet volute geometry		
Inlet radius of volute (r_1)	70.15	[mm]
Outlet radius of volute (r_2) (cost)	48.67	[mm]
Inlet radius of the volute area (**A=B**)	21.48	[mm]
Nozzle geometry		
Nozzle ring Radius (r_R)	40.33	[mm]
Nozzle inlet passage width (b_2)	4.08	[mm]
Nozzle chord length (C_{nozzle})	23.25	[mm]
Nozzle Outlet geometric angle ($\beta_{3,g}$)	10.88	[deg]
Nozzle Outlet radius (r_3)	35.07	[mm]
Number of Nozzle Blades (N_N)	21	[-]
Rotor geometry		
Rotor Inlet Radius (r_4)	31.99	[mm]
Rotor inlet geometric angle ($\beta_{4,g}$)	90	[deg]
Rotor inlet passage width (b_4)	4.08	[mm]

Rotor Outlet Mean Radius (r_5)	15.24	[mm]
Exit Hub Radius (r_{h5})	9.60	[mm]
Exit Tip Radius (r_{s5})	20.88	[mm]
Rotor outlet geometric angle ($\beta_{5,g}$)	-65.69	[deg]
axial length of the rotor (l_R)	16.92	[mm]
Number of Rotor Blades (Nr)	17	[-]
stage axial length ($\Delta z_{(ST)}$)	55.81	[mm]

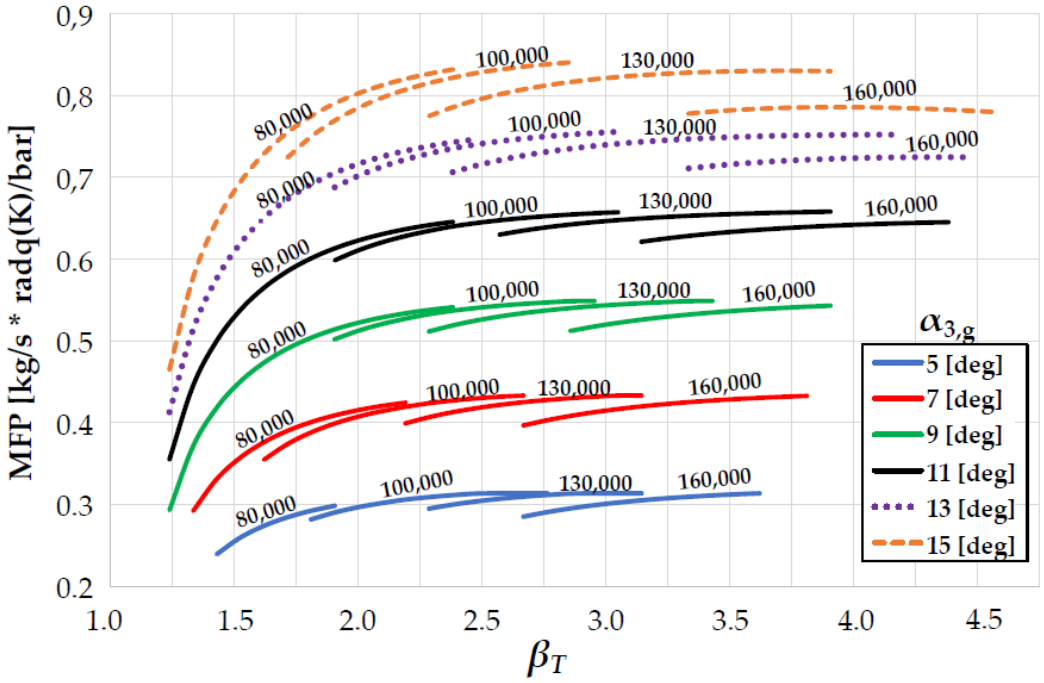

Figure 32: Turbine MFP curves as function of pressure ratio β_T for different position of nozzle blade metal angle

At this point, a fundamental difference between the separated electric compound system and a traditional turbocharged engine must be highlighted; in the common turbocharging application, the turbine is mechanically linked to the compressor and its speed of rotation is governed by the fluid dynamics of the complex system constituted by the compressor, the engine and the turbine; in the compound system here considered, instead, the turbine is not connected to the compressor and hence its speed of rotation is not constrained: this gives the compound system an additional degree of freedom; in effect, the variable nozzle turbine may adapt to each

engine exhaust mass flow and pressure ratio with infinite values of the rotor speed, each one corresponding to a single nozzle blade position; this implies that, in the separated electric compound engine, a double control action must be performed on the turbine, properly setting both the nozzle blade angle and the rotor speed, the latter being controlled by means of the electric generator.

According to this considerations, the author evaluated, for each exhaust mass flow and pressure ratio, the turbine thermomechanical efficiency with varying rotor speed, evaluating for each single case the nozzle blade angle required to comply with the mass flow: Figure 33 reports some of the results obtained and clearly shows that, for each engine exhaust mass flow and pressure ratio, a single value of the rotor speed of rotation (to which correspond a proper nozzle blade angle) allows to maximize the turbine efficiency. On account of this, and with the aim to let the turbine operate always at its best efficiency, the author evaluated, for each exhaust mass flow and pressure ratio, the rotor speed of rotation which maximizes the turbine efficiency, together with the related nozzle blade angle, which are both shown in the graphs of Figure 34: it is hence assumed that, whichever is the operating condition of the exhaust gas turbine, the rotor speed of rotation and the nozzle blade will be set to their best efficiency values. It can be clarified now that the turbine efficiency optimization calculation was followed also for each of the several turbine geometries evaluated during the design and validation procedure: this means that every value reported in Figure 31 represents the best efficiency of the turbine for one of the operating condition reported in **Figure 30**.

Figure 32 clearly shows that the variable nozzle geometry radial inflow turbine designed for the present work is fully able to swallow a wide range of mass-flow rates through the variation of the nozzle blade angle $\alpha_{3,g}$.

The turbine performances evaluated by the model presented in chapter 6.1 have been estimated supposing to employ a double control system, acting on both the nozzle blade angle $\alpha_{3,g}$ and on the rotational speed of the turbine. Specifically, for each operating condition, the author considered the required turbine mass-flow rate G_T and pressure ratio β_T (see Figure 30) and have been evaluated the couple of value, blade angle and turbine rotational speed, that ensured the best turbine thermomechanical efficiency.

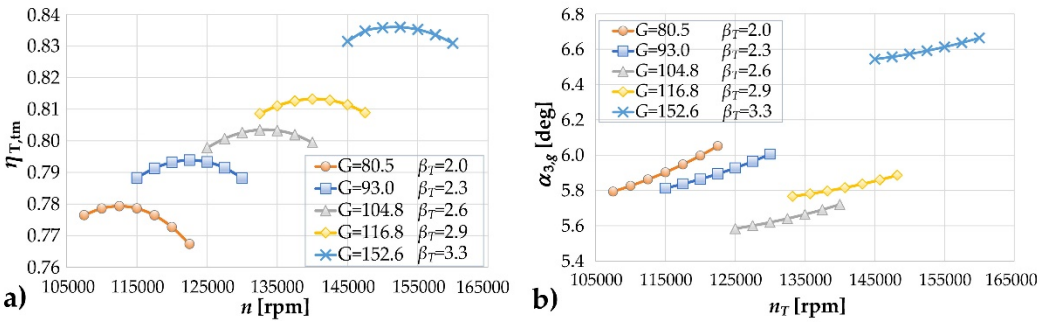

Figure 33: a) Turbine thermomechanical efficiency and b) nozzle outlet blade angle $\alpha_{3,g}$ as function of rotational speed for different operating conditions

As it could be expected, the implementation of the mean-line prediction model allowed to obtain realistic turbine efficiency values different from the constant values assumed in chapter 5 (i.e. 0.70 and 0.75). Figure 35 reports the turbine thermomechanical efficiency predicted by the model, as function of the exhaust mass flow G_T and pressure ratio β_T: as shown, the thermomechanical efficiency of the designed turbine ranges between a minimum value 65% up to a maximum value 84%, with the best efficiencies located in the high pressure/mass flow rate region.

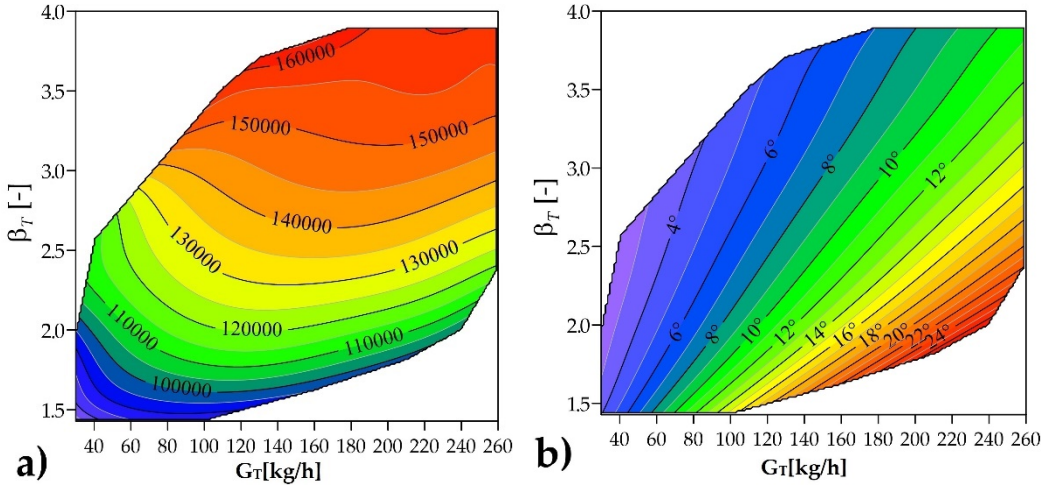

Figure 34: a) Optimum rotational speed and b) nozzle blade angle as function of mass flow-rate G_T and pressure ratio β_T

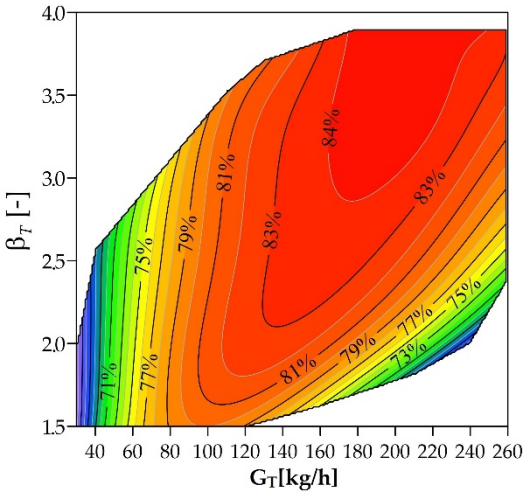

Figure 35: Optimized thermomechanical efficiency map of the turbine as function of mass flow-rate G_T and inlet pressure ratio β_T

7. Realistic performance of the turbo-compound system

As already clarified, the main task of the present thesis is to evaluate the realistic performance attainable by the hybrid propulsion system equipped with the separated electric compound engine. For this purpose, a CNG-fuelled SI compound engine was calculated following the modelling approach illustrated in chapter 5 and adopting the newly designed turbine geometry, whose thermomechanical efficiencies were evaluated, for each operating condition, through the mean-line model presented in chapter 6.

As already done in chapter 5, with the aim to perform a comparison with a traditional turbocharged engine based on an equal power basis, the compound engine was designed to deliver an overall output power of 73.5 kW: this means that, once evaluated the specific performances in terms of brake mean effective pressure, the displacement of each engine was sized so as to ensure the same output power of 73.5 kW (which corresponds to 100 HP). The realistic efficiency of the compound engine will then be compared to the efficiency of the reference turbocharged engine of the same nominal output power, described in chapter 0. It is worth mentioning that both the compound engine and the reference turbocharged engine have been supposed to be developed starting from the same baseline naturally aspirated engine of chapter 0. The only peculiarity of the calculations performed in the present section regards the evaluation of the exhaust gas temperature T_{EX} at the turbine inlet, which was evaluated on the basis of the ratio between the in-cylinder gas temperature T_{EVO} at the exhaust valve opening (EVO) and the inlet gas temperature T_{IVC} at intake valve closure (IVC) (eq. (36)); in modern spark ignition engines, the ratio T_{EVO}/T_{IVC} usually ranges between *3.5* and *4.5*, depending on the particular engine and on its operating condition; in this chapter the ratio T_{EVO}/T_{IVC} was assumed to remain constant and equal to 4, for both the compound engine and the reference turbocharged engine.

As could be easily expected, the realistic behavior of the turbine influenced substantially the performance of the compound engine, increasing the energy recovery at the higher power levels, where the realistic turbine revealed a better efficiency. The implementation of the realistic characteristic of the turbine required hence a new optimization of the whole compound engine, whose purpose is to maximize the overall brake thermal

efficiency $\eta_{bTOT,COMP}$ of the compound system for each operating condition. More specifically, the optimization process mainly regards the engine exhaust pressure level to be adopted for each operating condition of the compound engine; as obvious increasing the engine exhaust pressure produces an increment in the energy transformed by the turbine, but, at the same time, worsens the indicated efficiency of the engine, due to the increased residual gas fraction. As mentioned, a genetic algorithm was employed for the system efficiency optimization, since the latter is not a linear or polynomial function of the engine exhaust pressure. Figure 36 reports the contour map of the new optimal exhaust pressure levels obtained, for each overall brake mean effective pressure of the compound engine $BMEP_{TOT,COMP}$ and mean piston speed Sp, thanks to the implementation of the realistic turbine efficiency characteristic.

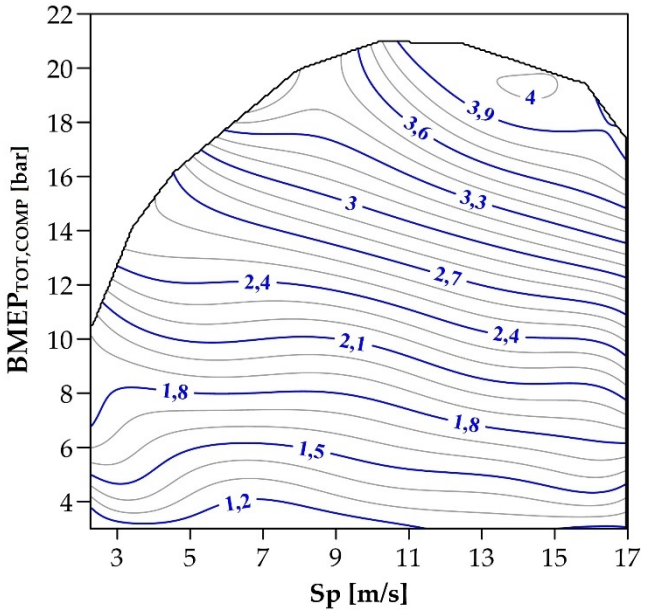

Figure 36: Optimal exhaust pressure levels of the compound engine, as function of load and mean piston speed

As can be observed in Figure 36, exhaust pressures up to 4.0 bar were determined in the high load/speed region, which can be easily explained considering that higher engine power implies higher in-cylinder pressures

and exhaust mass flows: in these conditions, the turbine can provide a greater contribution to the overall output power of the system without compromising the engine indicated efficiency, leading to greater exhaust gas energy recovery.

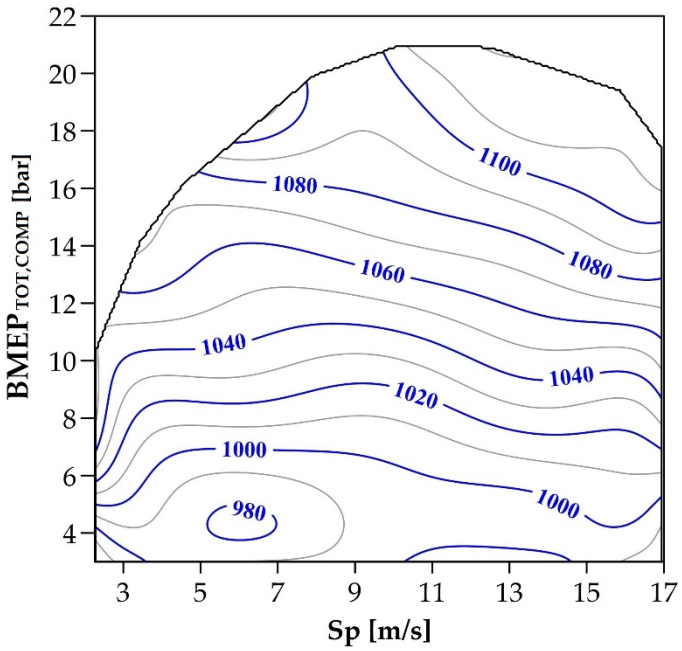

Figure 37: Exhaust gas temperature *[K]* related to the optimal exhaust pressure levels of the compound engine, as function of load and mean piston speed

The same Figure 36 also shows that the optimal exhaust pressure levels are significantly higher than in a traditional turbocharged engine; considering also the related exhaust gas temperature (between 980 and 1120 K, as reported in Figure 37), this further confirms the appropriateness of the gas turbine for the energy recovery, since its state of the art already complies with the boundary conditions imposed by the particular task. The high optimal exhaust pressure levels also point out the necessity of a proper turbine design algorithm, as well as of a reliable model for the turbine efficiency prediction, which certainly allow to obtain more realistic evaluations of the separated electric compound engine efficiency.

The new optimization process led to updated the maximum $BMEP_{TOT,COMP}$ levels for each mean piston speed of the compound engine, and, as a consequence, also the new compound engine displacement V_{COMP} necessary to develop the maximum target power of 73.5 kW. The resulting specifications of the updated compound engine are summarized in Table 11.

Table 11: Main characteristic of the realistic separated electric compound engine

Engine type	4-stroke, spark ignition
Injection system	CNG multi-point injection
Valvetrain	4 valves/cylinder, VVT
Compression ratio	11
Max boost pressure	1.85 bar
Number of cylinders	3
Stroke/bore ratio	1.11
Displacement [cc]	673.4
T_{EVO}/T_{IVC}	4
Max $BMEP_{TOT,COMP}$	21.01 bar at 4330 rpm
Max $POW_{TOT,COMP}$	73.5 kW at 6740 rpm
Min $BSFC_{TOT,COMP}$	176.4 g/kWh
Variation of min BSFC	−11.50%
Max POW_{REC}/POW_{COMP}	38.7%
Max POW_{REC}	21.97 kW at 6740 rpm

As shown, a reduction in the minimum brake specific fuel consumption of -11.50% with respect to the reference turbocharged engine was obtained by the new optimized compound engine. Table 11 also shows that the maximum percentage contribution of the exhaust gas turbine to the overall output power increased up to 38.7%, which denotes a remarkable increment

with respect to the values previously obtained assuming a constant efficiency turbine (29.7% and 33.9% with the constant turbine efficiency of 0.70 and 0.75 respectively): this is a further confirmation on how the appropriate evaluation of the real turbine capability may be fundamental for a reliable performance evaluation of the whole compound system. A higher efficiency turbine allows a better exploitation of the exhaust gas expansion, altering the proportion between the power delivered by the turbo-generator and by the engine: this is also confirmed by the new maximum power delivered by the exhaust gas turbine, which reached 21.97 kW and revealed higher than the values determined in the preliminary study (17.82 kW and 19.64 kW with the constant turbine efficiency of 0.70 and 0.75 respectively).

Figure 38 shows the contour maps of the new overall specific fuel consumption $BSFC_{TOT,COMP}$ obtained for the compound engine, while the map shown in Figure 39 refers to the reference turbocharged engine; it can be noted that the compound engine always exhibits a better fuel economy compared to the reference traditional turbocharged system. For a clearer evaluation of the advantages related to the implementation of the compound system, the map in Figure 40 reports the efficiency improvement of the realistic compound engine with respect to the reference turbocharged engine, as a function of the overall output power and mean piston speed; as can be observed, the efficiency improvements are limited (+4%) at the minimum power levels and increase with the power output, reaching a maximum value of 19%; this trend can be easily explained, since higher engine power implies higher in-cylinder pressures and exhaust mass flows, which, as shown in Figure 35, represent the conditions for which the turbine reveals its best efficiencies, and hence the conditions in which the turbine

can provide a greater contribution to the overall output power of the system without compromising the engine indicated efficiency.

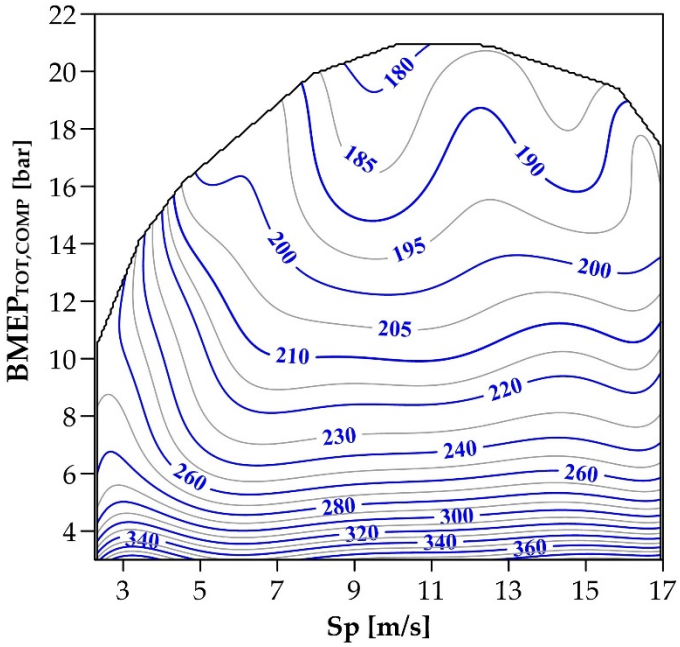

Figure 38: Brake specific fuel consumption map (g/kWh) of the realistic compound engine, as a function of the overall load and mean piston speed

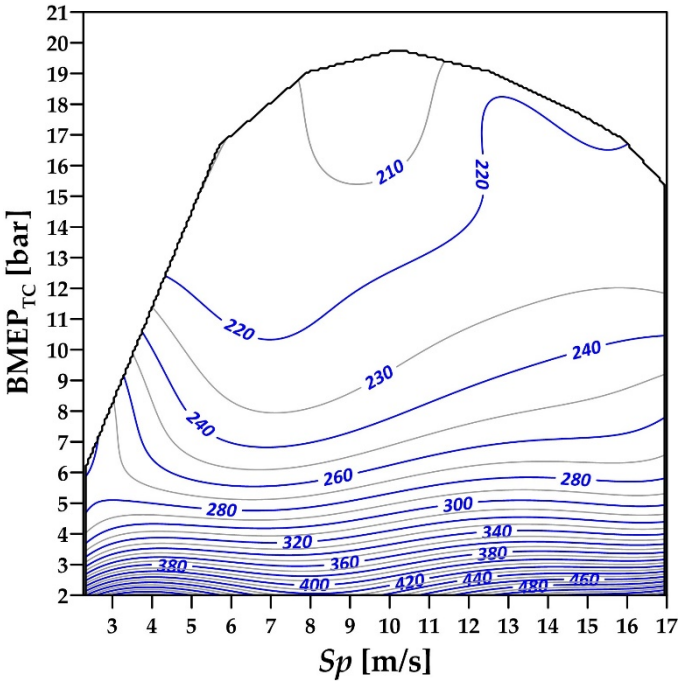

Figure 39: Brake specific fuel consumption (g/kWh) of the reference turbocharged engine, as a function of load and mean piston speed

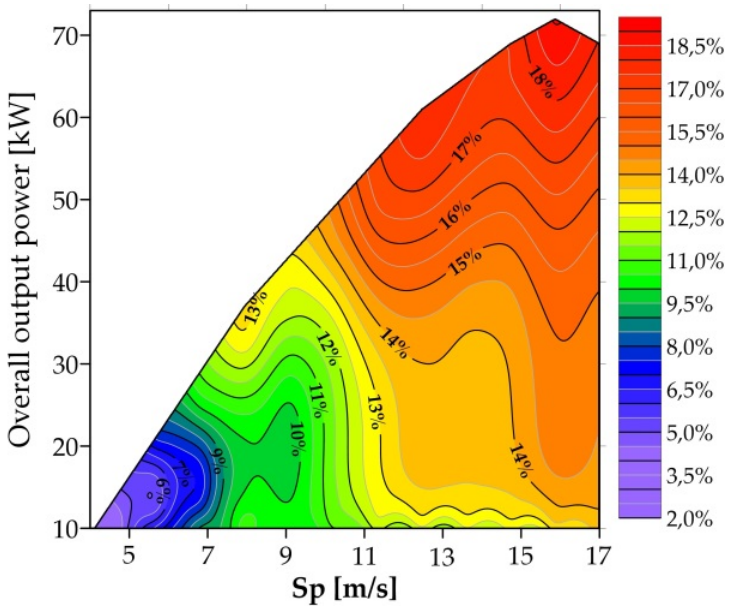

Figure 40: Efficiency improvement of the realistic compound engine with respect to the reference turbocharged engine as a function of power output and mean piston speed

As already said in chapter 5, considering the application on a hybrid propulsion system, a further and fairer comparison of the efficiencies of the two thermal units should be carried out on the basis of the best efficiency curves of both the realistic compound engine and the reference turbocharged engine. The result of this further comparison is shown in Figure 41, where, for each power level, the best efficiencies of both propulsive solutions are compared.

As can be noted, a maximum 17.9% efficiency improvement is obtained by the compound engine for the overall output power of 64 kW; a minimum 3% efficiency increment is instead obtained for the overall output power of 8 kW, while the average efficiency increment on the whole output power range is 10.9%. For a comparison purpose, it is worth mentioning that in the preliminary analysis of chapter 5, when the turbine efficiency was considered constant and equal to 0.75, it was estimated a maximum overall efficiency improvement of 15.6% with respect to the same reference

turbocharged engine, with an average increment of 10.2% on the whole power range.

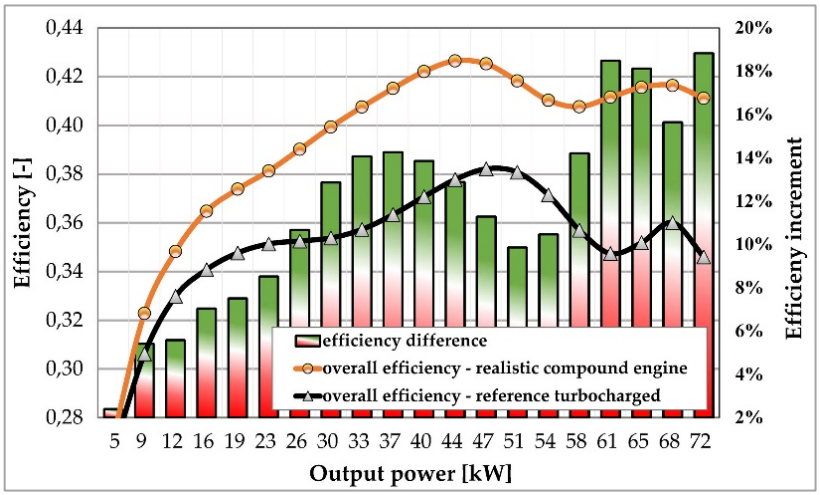

Figure 41: Comparison between the best efficiency curves of the realistic compound engine with respect to reference traditional turbocharged engine

8. Conclusion

This thesis deals with the energetic advantages related to the adoption of a separated electric turbo-compound propulsion unit for CNG-powered hybrid vehicles. The proposed compound system is composed of a supercharged CNG-fueled spark ignition engine equipped with an exhaust gas turbo-generator group dedicated to the unexpanded gas energy recovery. The supercharger is powered by an electric motor only when necessary (i.e., for manifold pressure higher than 1 bar), while the turbo-generator group is always active, continuously recovering energy from the whole exhaust gas mass flow. The system is particularly suitable for electric hybrid vehicle architectures in which the electric energy produced by the turbine generator can be stored on the vehicle storage system and hence profitably employed for vehicle propulsion. The benefits connected to the implementation of the compound unit were evaluated with respect to a

traditional CNG-fueled turbocharged reference engine, from the perspective of hybrid applications; for this purpose, the author implemented a simple model, mainly based on power and mass flow balances, sometimes integrated by experimental data. With the aim to perform a fair and reasonable comparison, both the compound engine and the turbocharged reference engine were calculated starting from the same baseline naturally aspirated CNG engine. As described in the first part of this thesis, the results obtained are influenced by a characteristic temperature ratio (T_{EVO}/T_{IVC})—that is the ratio between the in-cylinder gas temperature when the exhaust valve opens (T_{EVO}) and the in-cylinder gas temperature when the inlet valve closes (T_{IVC}); this temperature ratio plays an important role, since it directly influences the temperature of the gas entering the turbine of both the turbocharged engine and the compound engine: it mainly depends on the particular engine and on the operating condition, and may assume values between 3.5 and 4.5. In order to provide the results with a general validity, three different values of this temperature ratio were considered in the first part of this thesis, namely 3.5, 4.0 and 4.5. As also explained in this work, the turbine considered for the compound engine substantially differs from common turbines employed for turbocharging purposes, with regards to both the high-pressure ratios and the quasi-steady operating conditions that characterize its application: for these reasons, with the aim to ascertain the significance of the turbine efficiency in the compound engine performances, in the preliminary analysis of the compound system, two plausible values were considered, i.e., $\eta_{T,tm}$= 0.70 and $\eta_{T,tm}$= 0.75. The effect of the exhaust back pressure increment on both the compound engine volumetric efficiency and the indicated efficiency was also taken into account: for each operating

condition of the compound engine, the optimal exhaust pressure was hence determined by maximizing the compound system's overall efficiency.

Compared to the turbocharged reference engine, the preliminary analysis of the compound propulsion unit revealed a lower brake specific fuel consumption, with a reduction of between 6.33% and 12.32% for the two extreme cases of T_{EVO}/T_{IVC}= *3.5*, $\eta_{T,tm}$= 0.70 and T_{EVO}/T_{IVC}= *4.5*, $\eta_{T,tm}$= 0.75 respectively. The contribution of the turbine-generator to the overall power produced by the compound system revealed maximum shares between 24.2% and 42.9%, with a maximum power output of between 15.2 and 23.3 kW.

Considering that in hybrid propulsion vehicles, the internal combustion engine is usually employed in operating conditions close to the best efficiency curve, the authors also carried out a further comparison based on the best efficiency curves of both the compound engine and the turbocharged engine. This last comparison revealed that the compound propulsion unit could allow average efficiency improvement (i.e., on the whole output power range) of between 6.1% and 11.2%, depending on the temperature ratio and the turbine efficiency, with maximum benefits of 15.6% in the best case (T_{EVO}/T_{IVC} = 4.5; $\eta_{T,tm}$ = 0.75).

The preliminary analysis of the turbo-compound system here proposed, shown very encouraging results. Some simplifying assumption, mainly related to the turbine efficiency which was supposed to be constant, however detracted from the reliability of the results obtained in the preliminary analysis. In the second part of this thesis the author aims to obtain a more realistic evaluation of the performance attainable by the separated electric compound engine taking into account a realistic thermomechanical efficiency of the turbine, which should depend on the

operating condition. First of all the author focused on the selection the proper kind of machine; some thermodynamic and fluid dynamic evaluations based on the preliminary obtained results allowed to select radial variable nozzle turbines as the best compromise between compactness and performances. Successively, a simple but reliable model based on mean-line approach was developed for the estimation of the turbine realistic efficiency on all the operating conditions. An effective but simple design algorithm was also presented, which, by means of some simplifying assumption, allows a fast determination of the main geometric dimension of the turbine.

After the presentation of both the design algorithm and the performance prediction model of the turbine the author dedicated to the definition of the best turbine design operating condition. The design algorithm presented in paper was employed, also implementing an optimization process which allowed maximizing the efficiency of the turbine on the whole range of utilization of the compound engine. Once determined the best turbine geometry, its realistic performances have been evaluated by means of the mean-line performance prediction model, also determining the characteristic map of the turbine. The realistic prediction model allowed to estimate an average thermomechanical turbine efficiency of 0.804 in the operating range related to the best efficiency curve of the compound-engine. The performance prediction model also pointed out that the efficiency of the turbine strongly depends on the working conditions, ranging from a minimum value of 65% for the smallest pressure ratio and mass flow rates, to a maximum value of 84% in the higher-pressure ratio and mass flow rates region. The realistic energetic advantages of the separated electric compound engine were hence evaluated on the basis of

the realistic turbine efficiencies predicted by the model, and compared to the reference turbocharged engine of the same nominal output power analyzed in the first part of the thesis. It was found that the realistic turbine behaviour influenced substantially the performance of the compound engine, leading to a better exhaust gas energy recovery at the higher output power levels.

As a final result, compared to a traditional turbocharged engine, the efficiency advantages of the newly proposed electric turbo-compound engine are comprised between 3.1% and 17.9%, depending on the output power level. The average efficiency increment, evaluated on the whole best efficiency curve, revealed equal to 10.9%.

1. Eurostat, Energy, transport and environment statistics - 2020 edition, DOI: 10.2785/522192, https://ec.europa.eu/eurostat/web/products-statistical-books/-/ks-dk-20-001
2. European Environment Agency; Monitoring CO2 emissions from passenger cars and vans in 2018, doi:10.2800/19757
3. European Commission, Climate Action, EU Action, Transport emissions, Road transport: Reducing CO2 emissions from vehicles, CO2 emission performance standards for cars and vans, https://ec.europa.eu/clima/eu-action/transport-emissions/road-transport-reducing-co2-emissions-vehicles/co2-emission-performance-standards-cars-and-vans_en
4. Zhao, Y., Chen, J., (2006), Performance analysis and parametric optimum criteria of an irreversible Atkinson heat-engine, Applied Energy, 83 (8), pp. 789-800, DOI: 10.1016/j.apenergy.2005.09.007
5. Hou, S.-S., (2007), Comparison of performances of air standard Atkinson and Otto cycles with heat transfer considerations, Energy Conversion and Management, 48 (5), pp. 1683-1690, DOI: 10.1016/j.enconman.2006.11.001
6. Zhao, J., Xu, F., (2018), Finite-time thermodynamic modeling and a comparative performance analysis for irreversible Otto, Miller and Atkinson cycles, Entropy, 20 (1), art. no. 75, DOI: 10.3390/e20010075
7. R. H. Miller, Supercharging and Internal Cooling Cycle for High Output, Transactions of ASME 69, pp.453-457, 1947.
8. Zhuge, W., Huang, L., Wei, W., Zhang, Y. et al., "Optimization of an Electric Turbo Compounding System for Gasoline Engine Exhaust Energy Recovery," SAE Technical Paper 2011-01-0377, 2011, https://doi.org/10.4271/2011-01-0377
9. Kawamoto, N., Naiki, K., Kawai, T., Shikida, T. et al., 2009, "Development of New 1.8-Liter Engine for Hybrid Vehicles," SAE Technical Paper 2009-01-1061, doi.org/10.4271/2009-01-1061
10. Wang, Y., Lin, L., Zeng, S., Huang, J., Roskilly, A.P., He, Y., Huang, X., Li, S., (2008), Application of the Miller cycle to reduce NOx emissions from petrol engines, Applied Energy, 85 (6), pp. 463-474, DOI: 10.1016/j.apenergy.2007.10.009
11. Aghaali, H., Ångström, H.-E., (2015), A review of turbocompounding as a waste heat recovery system for internal combustion engines, Renewable and Sustainable Energy Reviews, 49, pp. 813-824, DOI: 10.1016/j.rser.2015.04.144
12. Alshammari, M., Alshammari, F., Pesyridis, A., Electric boosting and energy recovery systems for engine downsizing, (2019) Energies, 12 (24), art. no. 4636, DOI:10.3390/en12244636
13. Pasini, G., Lutzemberger, G., Frigo, S., Marelli, S., Ceraolo, M., Gentili, R., Capobianco, M., Evaluation of an electric turbo compound system for SI engines: A numerical approach, (2016) Applied Energy, 162, pp. 527-540, DOI:10.1016/j.apenergy.2015.10.143
14. Arsie, I., Cricchio, A., Pianese, C., Ricciardi, V., De Cesare, M., Evaluation of CO2 reduction in SI engines with Electric Turbo-Compound by dynamic powertrain modelling,(2015) IFAC-PapersOnLine, 28 (15), pp. 93-100, DOI:10.1016/j.ifacol.2015.10.014
15. Millo, F., Mallamo, F., Pautasso, E., Ganio Mego, G., The potential of electric Exhaust Gas Turbocharging for HD diesel engines,(2006) SAE Technical Papers, DOI:10.4271/2006-01-0437

16. Hopmann, U. and Algrain, M., "Diesel Engine Electric Turbo Compound Technology," SAE Technical Paper 2003-01-2294, 2003, https://doi.org/10.4271/2003-01-2294.
17. Mohd Noor, A., Che Puteh, R., Rajoo, S., Basheer, U. M., Md Sah, M. H., & Shaikh Salleh, S. H. (2015). Simulation Study on Electric Turbo-Compound (ETC) for Thermal Energy Recovery in Turbocharged Internal Combustion Engine. Applied Mechanics and Materials, 799–800, 895–901. doi.org/10.4028/www.scientific.net/amm.799-800.895
18. Kant, M., Romagnoli, A., Mamat, A.M., Martinez-Botas, R.F., Heavy-duty engine electric turbocompounding, (2015) Proceedings of the Institution of Mechanical Engineers, Part D: Journal of Automobile Engineering, 229 (4), pp. 457-472, DOI: 10.1177/0954407014547237
19. R. Cipollone, D. Di Battista, A. Gualtieri, Turbo compound systems to recover energy in ICE, International Journal of Engineering and Innovative Technology (IJEIT), Volume 3, Issue 6, December 2013, http://www.ijeit.com
20. Zhuge, W., Huang, L., Wei, W., Zhang, Y. et al., "Optimization of an Electric Turbo Compounding System for Gasoline Engine Exhaust Energy Recovery," SAE Technical Paper 2011-01-0377, 2011, https://doi.org/10.4271/2011-01-0377
21. Chris, M.; Abul Masrur, M. Hybrid Electric Vehicles: Principles and Applications with Practical Perspectives, 2nd ed.; San Diego State University: San Diego, CA, USA, 2017; ISBN 978-111-897-053-9.
22. Michon, M.; Calverley, S.; Clark, R.; Howe, D.; Chambers, J.; Sykes, P.; Dickinson, P.; Clelland, M.; Johnstone, G.; Quinn, R.; et al. Modelling and Testing of a Turbo-generator System for Exhaust Gas Energy Recovery. In Proceedings of the 2007 IEEE Vehicle Power and Propulsion Conference, Arlington, TX, USA, 9-12 September 2007; pp. 544–550. https://doi.org/10.1109/VPPC.2007.4544184.
23. Nonthakarn, P.; Ekpanyapong, M.; Nontakaew, U.; Bohez, E. Design and Optimization of an Integrated Turbo-Generator and Thermoelectric Generator for Vehicle Exhaust Electrical Energy Recovery. Energies 2019, 12, 3134. https://doi.org/10.3390/en12163134
24. Haughton, A. and Dickinson, A., "Development of an Exhaust Driven Turbine-Generator Integrated Gas Energy Recovery System (TIGERS®)," SAE Technical Paper 2014-01-1873, 2014, https://doi.org/10.4271/2014-01-1873.
25. Eriksson Lars, Lindell Tobias, Leufvén Oskar, Thomasson Andreas, 2012, "Scalable Component-Based Modeling for Optimizing Engines with Supercharging, E-Boost and Turbocompound Concepts," SAE International Journal of Engines, 5, 2, pp. 579 - 595, doi:10.4271/2012-01-0713
26. Millo, F.; Mallamo, F.; Digiovanni, R.; Dominici, A.; Morel, T.; Okarmus, M. Improving misfire diagnostic through coupled engine/vehicle numerical simulation. SAE Trans. 2004, 113, 466–475. Available online: https://www.jstor.org/stable/44723523 (accessed on September 2022).
27. Chen S. K., and Flynn, P. F., "Development of Single Cylinder Compression Ignition Research Engine", SAE Paper 650733
28. Heywood, John B., Internal combustion engine fundamentals, McGraw-Hill, Inc. Cambridge, Massachusetts, 2018; ISBN 126-011-610-7.
29. Xu, R.; Saggese C.; Lawson, R.; Movaghar, A.; Parise, T.; Shao, J.; Choudhary, R.; Park, J.W.; Lu, T.; Hanson, R.; et al. A physics-based approach to modeling real-fuel combustion chemistry – VI. Predictive kinetic models of gasoline fuels. Combustion and flame 2020, 220, 475-487, doi.org/10.1016/j.combustflame.2020.07.020.

30. AMG GAS, Local Natural Gas Supplier, http://www.amg.pa.it/
31. D'Ambrosio, S.; Spessa, E.; Vassallo, A.; Ferrera, M. et al. Experimental Investigation of Fuel Consumption, Exhaust Emissions and Heat Release of a Small-Displacement Turbocharged CNG Engine. SAE Technical Paper 2006, doi:10.4271/2006-01-0049.
32. Genchi, G.; Pipitone, E. Octane Rating of Natural Gas-Gasoline Mixtures on CFR Engine. SAE Int. J. Fuels Lubr 2014, 7(3), doi:10.4271/2014-01-9081.
33. NIST Chemistry WebBook, https://webbook.nist.gov/chemistry/ (accessed on 16 July 2022)
34. Michon, M.; Calverley, S.; Clark, R.; Howe, D.; Chambers, J.; Sykes, P.; Dickinson, P.; Clelland, M.; Johnstone, G.; Quinn, R.; et al. Modelling and Testing of a Turbo-generator System for Exhaust Gas Energy Recovery. In Proceedings of the 2007 IEEE Vehicle Power and Propulsion Conference, Arlington, TX, USA, 9-12 September 2007; pp. 544–550. https://doi.org/10.1109/VPPC.2007.4544184.
35. Nonthakarn, P.; Ekpanyapong, M.; Nontakaew, U.; Bohez, E. Design and Optimization of an Integrated Turbo-Generator and Thermoelectric Generator for Vehicle Exhaust Electrical Energy Recovery. Energies 2019, 12, 3134. https://doi.org/10.3390/en12163134
36. Haughton, A. and Dickinson, A., "Development of an Exhaust Driven Turbine-Generator Integrated Gas Energy Recovery System (TIGERS®)," SAE Technical Paper 2014-01-1873, 2014, https://doi.org/10.4271/2014-01-1873.
37. Pipitone, E.; Beccari, S. Performances and emissions improvement of an S.I. engine fuelled by LPG/gasoline mixtures. SAE Technical Papers 2010, doi:10.4271/2010-01-0615.
38. Pipitone, E.; Beccari, A. A Study on the Use of Combustion Phase Indicators for MBT Spark Timing on a Bi-Fuel Engine. SAE Technical Paper 2007, doi:10.4271/2007-24-0051.
39. Development and optimization of small-scale radial inflow turbine for waste heat recovery with organic Rankine cycle, Kiyarash Rahbar, Ph.D. Thesis in School of Mechanical Engineering
40. Aungier RH. Turbine Aerodynamics: Axial-flow and radial-inflow turbine design and analysis. New York (USA): ASME Press; 2005. ISBN-10: 0791802418
41. Meanline analysis of radial inflow turbines at design and off-design conditions, Zicheng Wei, Master of Applied Science in Aerospace Engineering
42. Moustapha, H.; Zelesky, M.F.; Baines, N.C.; Japikse, D. Chapter 8. In Axial and Radial Turbines; Concepts ETI, Inc.: Plano, TX, USA, 2003, ISBN-10: 0933283121
43. L. J. Kastner, F. S. Bhinder, A Method for Predicting the Performance of a Centripetal Gas Turbine Fitted with a Nozzle-Less Volute Casing, ASME, 1975
44. John D. Stanitz, One-dimensional compressible flow in vaneless diffusers of radial- and mixed-flow centrifugal compressors. including effects of friction, heat transfer and area change, National advisory committee for aeronautics, Lewis Flight Propulsion Laboratory Cleveland, Ohio, 1952
45. Whitfield, A. and N. C. Baines (1990). Design of radial turbomachines. Harlow, Essex, England; New York, NY, Longman Scientific & Technical ; Wiley. ISBN-10: 0582495016
46. Suhrmann, J., D. Peitsch, M. Gugau, T. Heuer and U. Tomm (2010). Validation and development of loss models for small size radial turbines. Proceedings of ASME Turbo

Expo: Power for land, sea and Air GT2010, Glasgow, UK. https://doi.org/10.1115/GT2010-22666

47. C. A. Wasserbauer and A. J. Glassman, Fortran program for predicting off-design performance of radial-inflow turbines, Lewis Research Center, National Aeronautics and Space Administration, Cleveland, Ohio 44135
48. D. Stanitz, Some theoretical aerodynamic investigations of impellers in radial and mixed-flow centrifugal compressors, ASME Paper, 74(1952), 473–497
49. Andrea Meroni, Miles Robertson, Ricardo Martinez-Botas, Fredrik Haglind, A methodology for the preliminary design and performance prediction of high-pressure ratio radial-inflow turbines, Energy, https://doi.org/10.1016/j.energy.2018.09.045
50. Daily, J. W., and Nece, R. E. (March 1, 1960). "Chamber Dimension Effects on Induced Flow and Frictional Resistance of Enclosed Rotating Disks." ASME. J. Basic Eng. March 1960; 82(1): 217–230. https://doi.org/10.1115/1.3662532
51. Ghosh, S. K., Sahoo, R. K., and Sarangi, S. K., Mathematical Analysis for Off-Design Performance of Cryogenic Turboexpander, ASME. J. Fluids Eng. March 2011; 133(3): 031001. https://doi.org/10.1115/1.4003661
52. Friction Characterization of Turbocharger Bearings, Erik Sjöberg, Master of Science Thesis MMK 2013:06 MFM 149
53. Shigley's Mechanical Engineering Design, Tenth Edition in SI Units, McGraw-Hill, ISBN: 9780073398204
54. Rohlik, H. E., 1968, Analytical Determination of Radial Inflow Turbine Design Geometry for Maximum Efficiency, Technical Note TN D-4384, NASA, Washington, DC.
55. C. Ventura, J. Peter, A. Rowlands, P. Petrie-Repar, E. Sauret, Preliminary Design and Performance Estimation of Radial Inflow Turbines: An Automated Approach, Journal of Fluids Engineering, Transactions of ASME, 2012, DOI: 10.1115/1.4006174
56. A. J. Glassman, Computer program for design analysis of radial-inflow turbines, Lewis Research Center, Clevehnd, Ohio 44135, 1976
57. Bohac, S.V.; Assanis, D.N. Effect of Exhaust Valve Timing on Gasoline Engine Performance and Hydrocarbon Emissions. SAE Technical Paper. 2004. Available online: https://www.jstor.org/stable/44740919 (accessed on December 2022)

Abbreviations and symbols

A	Area	[m²]
AR	Aspect ratio	[-]
b	Blade width	[m]
$BMEP$	Brake mean effective pressure	[bar]
$BMEP_{max}$	Maximum BMEP [bar]	[bar]
$BMEP_{TC}$	Brake mean effective pressure of the reference turbocharged engine	[bar]
$BMEP_{TOT,COMP}$	Overall BMEP of the compound engine	[bar]
$BSFC$	Brake specific fuel consumption	[g/kWh]
$BSFC_{COMP}$	Overall BSFC of the compound engine	[g/kWh]
c	Absolute velocity	[m/s]
c_{0s}	Spouting velocity	[m/s]
ch	Chord	[m]
$CMEP$	Compressor mean equivalent pressure	[bar]
c_p	Constant pressure specific heat	$\frac{J}{kg \cdot K}$
$c_{p,c}$	Specific heat at constant pressure of the air	$\frac{J}{kg \cdot K}$
$c_{p,s}$	Specific heat at constant pressure of burned gas	$\frac{J}{kg \cdot K}$
c_v	Constant volume specific heats	$\frac{J}{kg \cdot K}$
D_{hyd}	Hydraulic diameter	[m]
EVO	Exhaust valve open	[-]
$FMEP$	Friction mean effective pressure	[bar]
G	Mass flow rate	[kg/s]
G_{COMP}	Air mass flow of the compound engine	[kg/s]
GCR	Geometrical compression ratio	[-]
G_T	Turbine gas mass flow (turbocharged engine)	[kg/s]
G_{TC}	Engine air mass flow (turbocharged engine)	[kg/s]
H	Specific enthalpy	[J/kg]
$ICEV$	Internal combustion engine vehicle	[-]
$IMEP$	Indicated mean effective pressure	[bar]
$IMEP_g$	Gross indicated mean effective pressure	[bar]
IVC	Inlet valve closure	[-]
k	Specific heat ratio	[-]
k_S	Isentropic coefficient of the exhaust gas	[-]
LHV	Lower heating value of the fuel	[MJ/kg]
L_{hyd}	Hydraulic length	[m]
l_r	Rotor axial length	[m]
M	Mach number	[-]
m_{air}	Fresh air charge mass	[kg]

MAP	Manifold absolute pressure	[bar]
MAP_{max}	Maximum MAP	[bar]
MFP	Mass flow parameter	[-]
n	Rotational speed	[rpm]
N_R	Number of rotor blades	[-]
p	Pressure	[Pa]
p_c	Boosting pressure	[bar]
$PMEP$	Pumping mean effective pressure	[bar]
POW_{comp}	Power required by the compressor	[W]
POW_{tur}	Power produced by the turbine	[W]
p_S	Engine exhaust pressure	[bar]
p_{S0}	Exhaust pipe pressure	[bar]
r	Radius	[m]
R_{CNG}'	Specific gas constant of natural gas	$\frac{J}{kg \cdot K}$
Re	Reynolds number	[-]
RGF	Residual gas fraction	[-]
R_{INT}	Intercooler efficiency	[-]
$RMEP$	Recovery mean equivalent pressure	[bar]
RR	Wall relative roughness	[m]
R_S'	Specific gas constant of exhaust gas or burned gas	$\frac{J}{kg \cdot K}$
S	Normalized mean piston speed = $Sp/Spmax$	[-]
Sp	mean piston speed	[m/s]
Sp_{max}	maximum mean piston speed	[m/s]
t	Trailing edge blade thickness	[m]
T	Temperature	[K]
$T_{(EVO)}$	In-cylinder gas temperature at EVO	[K]
$T_{(IVC)}$	In-cylinder gas temperature at IVC	[K]
T'_{TC}	Air temperature at the compressor outlet	[K]
T_0	Air temperature in the intake manifold	[K]
T_S	Exhaust gas temperature	[K]
T_{TC}	Air temperature at the intercooler outlet	[K]
u	Peripheral velocity	[m/s]
V_A	Naturally aspirated engine displacement	[m^3]
V_{COMP}	Engine displacement in the compound unit	[m^3]
V_{TC}	Turbocharged engine displacement	[m^3]
w	Relative velocity	[m/s]

Greek letters

α	Absolute flow angle	[deg]
αF	Air-fuel ratio	[-]
$\alpha F,_{ST}$	Stoichiometric air-fuel ratio	[-]
β	Relative flow angle	[deg]
β_C	Compressor pressure ratio	[-]
β_T	Exhaust gas turbine pressure ratio	[-]
δ_A	Air density in the intake manifold	[kg/m^3]
δ_{COMP}	Density of the compressed air in the intake manifold for the compound engine	[kg/m^3]
Δh	Enthalpy drop	[J/kg]
δ_T	Density of the compressed air in the intake manifold for the turbocharged engine	[kg/m^3]
ε	Number of revolutions per cycle	[-]
εc	Clearance gap	[m]
η	efficiency	[-]
η_{br}	Brake thermal efficiency of the engine	[-]
$\eta_{br,max}$	Maximum brake thermal efficiency of the engine	[-]
$\eta_{bTOT,COMP}$	Overall brake thermal efficiency of the compound engine	[-]
η_c	Compressor efficiency	[-]
η_{EM}	Electric motor efficiency	[-]
η_i	Indicated thermal efficiency of the engine	[-]
$\eta_{i,g}$	Gross indicated thermal efficiency of the engine	[-]
η_T	Turbine efficiency of the compound engine	[-]
$\eta_{T,TC}$	Turbine efficiency of the reference turbocharged engine	[-]
λ	Relative air-fuel ratio	[-]
λ_V	Volumetric efficiency of the engine	[-]
$\lambda_{V,COMP}$	Volumetric efficiency of the compound engine	[-]
$\lambda_{V,TC}$	Volumetric efficiency of the reference turbocharged engine	[-]
ν	kinematic viscosity	[m^2/s]
ν_s	velocity ratio	[-]
ρ	Density	[kg/m^3]
φ	relative MAP = MAP/MAP_{max}	[-]
ω	rotational speed	[rad/s]

Subscripts

0	Reference condition
1	Total
2	Nozzle inlet
3	Nozzle exit
4	Rotor inlet
5	Rotor exit
a	Axial
b	Blade
br	brake
cl	Clearance
COMP	Compound engine
f	Fluid-dynamic
g	Gross
h	Hub
id	Ideal
in	Incidence
is	Isentropic
J,B	Journal bearing
m	Meridional
nozzle	Nozzle
p	Passage
r	Radial
re	Real
rel	Relative
rot	Rotor
s	Exhaust gas
sh	Shroud
t	Trailing edge
T	Total
T,B	Thrust bearings
t,s	Total-to-static
t,t	Total-to-total
TC	Turbochargerd
tm	thermomechanical
u	Peripheral
vol	Volute
w	Windage

Appendix A

Residual Gas Fraction (RGF) evaluation

When engine inlet valves close (IVC), the mass entrapped in the cylinder results the sum of the residual gas from previous cycle (m_s) and of the fresh charge (m_o); the residual gas fraction (RGF), which represents the ratio between the residual gas mass and the total in-cylinder mass, is hence:

$$RGF = \frac{m_S}{m_{TOT}} = \frac{m_S}{m_0 + m_S} \tag{186}$$

The fresh charge mass entrapped in the cylinder depends on the engine volumetric efficiency λ_V :

$$m_0 = \lambda_V \cdot \frac{MAP}{R'_0 \cdot T_0} \cdot V \tag{187}$$

being T_0 and MAP the temperature and pressure in the intake manifold, and V the engine displacement. Assuming the residual gas mass as the amount of in-cylinder exhaust gas at the ideal end of the exhaust stroke (i.e. at top dead centre):

$$m_S = \frac{p_S}{R'_S \cdot T_R} \cdot \left(\frac{V}{\rho - 1} \right) \tag{188}$$

where T_R and p_s represent the temperature and pressure of the in-cylinder residual gas, ρ is the engine compression ratio and hence $V/(\rho-1)$ the in-cylinder volume at top dead centre. The residual gas temperature T_R, in line with the simple approach followed in this paper, can be evaluated neglecting the heat transfer with in-cylinder wall during the exhaust stroke, thus assuming an isentropic transformation:

$$T_R = T_{EVO} \cdot \left(\frac{p_{EVO}}{p_S} \right)^{\frac{1-k_s}{k_s}} \tag{189}$$

being p_{EVO} and T_{EVO} the in-cylinder gas pressure and temperature when the exhaust valves open (EVO). As mentioned, experimental findings confirmed by data reported in the scientific literature [28] [57] show that for a spark ignition engine the ratio T_{EVO}/ T_{IVC} ranges from 3.5 to 4.5. The isentropic coefficient k_S should be evaluated as function of the exhaust gas composition and temperature, as described above (from equation (37) to equation (40)).